Performance Characteristics of the Spiky Central Receiver Air Pre-heater (SCRAP)

by

Matti Lubkoll

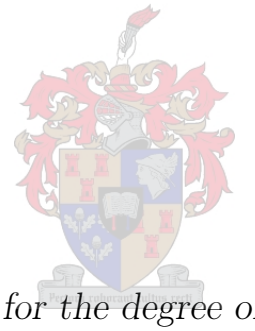

Dissertation presented for the degree of Doctor of Philosophy in the Faculty of Engineering at Stellenbosch University

Supervisor: Prof T.W. von Backström
Co-supervisor: Prof T.M. Harms

March 2017

Stellenbosch University https://scholar.sun.ac.za

Declaration

By submitting this dissertation electronically, I declare that the entirety of the work contained therein is my own, original work, that I am the sole author thereof (save to the extent explicitly otherwise stated), that reproduction and publication thereof by Stellenbosch University will not infringe any third party rights and that I have not previously in its entirety or in part submitted it for obtaining any qualification.

This dissertation includes four original papers published in peer-reviewed journals, peer-reviewed conference proceedings or books and one unpublished publication. The development and writing of the papers (published and unpublished) were the principle responsibility of myself and, for each of the cases where this is not the case, a declaration is included in the dissertation indicating the nature and extent of the contribution of co-authors.

Date: March 2017

Copyright © 2017 Stellenbosch University
All rights reserved.

Stellenbosch University https://scholar.sun.ac.za

Stellenbosch University https://scholar.sun.ac.za

Abstract

Performance Characteristics of the Spiky Central Receiver Air Pre-heater (SCRAP)

M. Lubkoll

Department of Mechanical and Mechatronic Engineering,
Stellenbosch University,
Private Bag X1, Matieland 7602, South Africa.

Dissertation: PhD (Eng)

March 2017

A combined cycle concentrating solar power (CSP) plant provides significant potential to achieve an efficiency increase and an electricity cost reduction compared to current single-cycle plants. A combined cycle CSP system requires a receiver technology capable of effectively transferring heat from concentrated solar irradiation to a pressurized air stream in a gas turbine. The novel spiky central receiver air pre-heater (SCRAP) technology is proposed to provide such a receiver and overcome barriers experienced by developments to date.

The SCRAP receiver is a novel metallic receiver technology aimed at pre-heating an air stream to about 800 °C, either prior to a combustion chamber or alternatively a cascaded secondary non-metallic receiver system, capable of achieving elevated temperatures. The SCRAP receiver is distinguished in shape and functioning from receiver concepts presented to date for the application in Brayton or combined cycles.

The receiver is predicted to perform at solar-thermal efficiencies exceeding 80 %. The geometric design of the receiver achieves a relatively low radiative heat loss, predicted at about 4 % – 5 %, whereas the relatively large surface results in vulnerability to convective heat losses. The pressure drop was found to be dependent on the geometries selected but relatively low, compared to existing alternative receiver designs, with system pressure drops below 40 mbar achievable.

A ray-tracing analysis showed that the flux impinging on the absorber assemblies is in its spatial distribution dependent on the solar field, more specific, the heliostat size and design. A thermodynamic model was developed to investigate the performance characteristics of the SCRAP receiver. The

Stellenbosch University https://scholar.sun.ac.za

developed thermodynamic computer model was verified against an experimental test setup designed and built at the heat transfer laboratory at Stellenbosch University. Tests with steam heating at nominally 100 °C show good agreement between the experimental results and the modeled predictions, at various air flow rates.

Further work on the SCRAP receiver technology is recommended. On the modeling side work is proposed on developing solutions for jet impingement heat transfer on the spike tip to improve heat transfer while reducing pressure drop. Further work on helically swirled fins is suggested to contribute to increased heat transfer characteristics. The receiver showed vulnerability towards convective heat losses; further work to better predict and mitigate these is required. Experiments under solar flux or simulated solar flux should further improve understanding of the technology. Cost effective manufacturing processes need to be developed to satisfy economic suitability of the receiver technology.

Stellenbosch University https://scholar.sun.ac.za

Uittreksel

Gedragskenmerke van die Puntige Sentrale Ontvanger Lug-Voorverwarmer (PSOLV)

(Performance Characteristics of the Spiky Central Receiver Air Pre-heater (SCRAP))

M. Lubkoll

Departement Meganiese en Megatroniese Ingenieurswese,
Universiteit van Stellenbosch,
Privaatsak X1, Matieland 7602, Suid-Afrika.

Proefskrif: PhD (Ing)

Maart 2017

'n Saamgestelde siklus gekonsentreerde sonkrag (GS) aanleg bied aansienlike potensiaal vir 'n toename in doeltreffendheid en 'n vermindering in elektrisiteitskoste in vergelyking met huidige enkel-siklus aanlegte. 'n Saamgestelde siklus GS aanleg vereis 'n ontvangertegnologie wat in staat is om warmte doeltreffend oor te dra vanaf sonstraling na 'n saamgedrukte lugstroom binne 'n gasturbine. Die nuwe Puntige Sentrale Ontvanger Lug-Voorverwarmer (PSOLV) tegnologie word voorgestel as so 'n ontvanger om hindernisse te oorkom wat tot dusver deur ontwikkelaars ervaar is.

Die PSOLV ontvanger is 'n nuwe, metaal-ontvanger tegnologie wat daarop gemik is om 'n lugstroom tot sowat 800 °C voor 'n verbrandingskamer te verhit, of alternatiewelik in 'n kaskade met 'n sekondêre nie-metaal ontvangerstelsel, wat in staat is om verhoogde temperature te bereik. Die PSOLV ontvanger word onderskei in vorm en funksionering van ontvanger konsepte tot op datum voorgestel vir toepassing in Brayton- of saamgestelde kringlope.

Die voorspelling is dat die ontvanger son-termiese doeltreffendhede van 80 % sal oorskry. Die geometriese ontwerp van die ontvanger bereik 'n relatief lae voorspelde stralingswarmteverlies van sowat 4 % – 5 %. Die relatief groot oppervlakte toon daarteenoor 'n kwesbaarheid vir konveksie warmteverliese. Daar is bevind dat die PSOLV drukval afhanklik is van die geselekteerde geometrieë, maar relatief laag is in vergelyking met bestaande alternatiewe ontvangers, met stelsel drukvalle onder 40 mbar bereikbaar.

'n Straalspoor analise het getoon dat die ruimtelike verdeling van die vloed wat inval op die ontvangersamestelling afhang van die sonversamelveld, en meer

Stellenbosch University https://scholar.sun.ac.za

spesifiek van die heliostaat grootte en ontwerp. 'n Termodinamiese model is ontwikkel om die gedragskenmerke van die PSOLV ontvanger te ondersoek. Die ontwikkelde rekenaar model is geverifieer teen 'n eksperimentele toetsopstelling, ontwerp en gebou in die warmteoordrag laboratorium by Stellenbosch Universiteit. Toetse met stoomverwarming by nominaal 100 °C toon goeie ooreenkoms tussen eksperimentele resultate en model voorspellings, by verskeie lugvloeitempo's.

Verdere werk op die PSOLV ontvanger tegnologie word aanbeveel. Op die modelleringskant word werk voorgestel op die ontwikkeling van oplossings vir straalbotsing-warmteoordrag binne die die stekelpunt om warmteoordrag te verbeter, terwyl drukval verminder word. Verdere werk op heliese vinne word anbeveel om by te dra tot verhoogde warmte-oordrag eienskappe. Die ontvanger het kwesbaarheid teenoor konvektiewe warmteverliese getoon; verdere werk word vereis om dit beter te voorspel en te beperk. Eksperimente onder direkte of gesimuleerde sonvloede behoort begrip van die tegnologie verder te verbeter. Koste-effektiewe produksieprosesse behoort ontwikkel te word om ekonomiese toepaslikheid van die ontvanger tegnologie te bevredig.

Stellenbosch University https://scholar.sun.ac.za

Acknowledgements

I would like to express my sincere gratitude to the following people:

- Prof TM Harms and Prof TW von Backström for their guidance throughout this project and the late Prof DG Kröger for his invaluable contribution in the origins of this work.
- Mr Cobus Zietsman without whom the experimental test setup would not exist today in the quality and usability as it is. His contribution was irreplaceable.
- Mr Calvin Hammerse, Mr Anton van den Berg, PJ, Mr Graham Hammerse, Mr Braveboy Sotondosha and especially Mr Nathi Hlempu, Ms Maurisha Galant and Mr Juliun Stanfliet, who all contributed along the way of creating the experimental test setup and making it work.
- My colleagues at the Solar Thermal Energy Research Group (STERG) who created an exceptional working environment, especially Dr Lukas Heller, Dr Kenneth Allen, Dr Stefan Hess as well as Dr Paul Gauché for the discussions and feedback they have provided.

Stellenbosch University https://scholar.sun.ac.za

Stellenbosch University https://scholar.sun.ac.za

Dedications

Für meine Eltern
Judith und Christoph

Stellenbosch University https://scholar.sun.ac.za

Contents

Stellenbosch University https://scholar.sun.ac.za

Stellenbosch University https://scholar.sun.ac.za

Stellenbosch University https://scholar.sun.ac.za

Stellenbosch University https://scholar.sun.ac.za

Stellenbosch University https://scholar.sun.ac.za

List of Figures

Stellenbosch University https://scholar.sun.ac.za

Stellenbosch University https://scholar.sun.ac.za

Stellenbosch University https://scholar.sun.ac.za

Stellenbosch University https://scholar.sun.ac.za

Stellenbosch University https://scholar.sun.ac.za

List of Tables

Stellenbosch University https://scholar.sun.ac.za

Nomenclature

Constants

R_{air}	$= 287.058\,J/(kg\,K)$
σ	$= 5.670 \times 10^{-8}\,W/(m^2\,K^4)$

Variables

Bi	Biot number	$[-]$
C	geometry function	$[-]$
c_p	specific heat	$[J/(kg\,K)]$
d	diameter	$[m]$
d_h	hydraulic diameter	$[m]$
f_D	Darcy friction factor	$[-]$
e	error	$[\%]$
h	height (duct)	$[m]$
h	heat transfer coefficient	$[W/(m^2\,K)]$
h	epecific enthalpy	$[J/kg]$
h_{fg}	enthalpy of condensation	$[J/kg]$
H	distance (from nozzle to plate/surface)	$[m]$
i	node number	$[-]$
I	irradiation (solar flux)	$[W/m^2]$
k	thermal conductivity	$[W/(m\,K)]$
K	stress concentration factor	$[\,]$
l	length	$[m]$
m	node number (fin)	$[kg/s]$
$\dot{m}$	mass flow rate	$[kg/s]$
n	node number	$[kg/s]$
N_{ducts}	number of ducts	$[-]$
Nu	Nusselt number	$[-]$
p	static pressure	$[Pa]$
Δp	differential pressure	$[Pa]$

Stellenbosch University https://scholar.sun.ac.za

$\dot{q}''$	heat flux	$[\mathrm{W/m^2}]$
$\dot{Q}$	heat rate	$[\mathrm{W}]$
r	radius	$[\mathrm{m}]$
Ra	Rayleigh number	$[-]$
Re	Reynolds number	$[-]$
S	surface (area)	$[\mathrm{m^2}]$
T	temperature	$[^\circ\mathrm{C}]$
t	(wall) thickness	$[\mathrm{m}]$
ΔT	differential temperature	$[\mathrm{K}]$
U	mean velocity	$[\mathrm{m/s}]$
U'	residual mean velocity	$[\mathrm{m/s}]$
u	velocity	$[\mathrm{m/s}]$
u	uncertainty	$[\%]$
V	volume	$[\mathrm{m^3}]$
w	width (duct)	$[\mathrm{m}]$
α	relaxation factor	$[-]$
α	thermal absorptivity	$[-]$
δ_x	control volume length	$[\mathrm{m}]$
ε	error	$[-]$
ε	thermal emissivity	$[-]$
η	efficiency	$[-]$
μ	dynamic viscosity	$[\mathrm{kg/(s\,m)}]$
ξ	friction coefficient	$[-]$
ρ	density	$[\mathrm{kg/m^3}]$
σ	stress (van Mises)	$[\mathrm{MPa}]$
τ_s	surface shear stress	$[\mathrm{Pa}]$

Abbreviations

BC	Brayton cycle
CC	combined cycle
CR	central receiver
CSP	concentrating solar power
DNI	direct normal irradiation
HTF	heat transfer fluid
LCOE	levelized cost of electricity
PTC	parabolic trough collector

Stellenbosch University https://scholar.sun.ac.za

PV photovoltaics
R South African Rand (ZAR)
RC Rankine cycle
SCRAP spiky central receiver air pre-heater
SUNSPOT Stellenbosch University solar power thermodynamic cycle

Subscripts

A area/cross-section(al)
adv advection
ax axial
bal energy balance
con condensate
cond conduction
conv convection
D Darcy
exp experiment(al)
f fin
h hydraulic (diameter)
i node number
i inner
m mean
o outer
opt optical
p pressure
r radial
rad radiation
s surface
sim simulation model
T temperature
t thermal

Stellenbosch University https://scholar.sun.ac.za

Stellenbosch University https://scholar.sun.ac.za

Chapter 1

Introduction[1]

1.1 Background

Concentrating solar power (CSP) plants have long been considered as a key contributor to renewable energy power generation in a sustainable world with a high renewable market penetration. In a rapidly developing and changing environment of renewable energy technologies, CSP maintains a unique value proposition, the built in ability for cost effective energy storage in the form of thermal storage. In fact, the levelized cost of electricity (LCOE) can be reduced by adding thermal storage to a plant, thereby providing dispatchability.

Nonetheless, bids for CSP plants around the world indicate current technologies not being cost competitive with other renewable energy technologies, as well as conventional base load (in the South African context: coal). CSP plants are currently considered to provide LCOEs at about 0.12 USD/kWh, whereas new built coal in South Africa is estimated at about 0.07 USD/kWh (DoE, 2016) and solar PV has recently reduced to 0.04 USD/kWh (Bischof-Niemz and Fourie, 2016).

CSP technologies are currently undergoing a revolution in technology from the conventional parabolic trough collector (PTC) to central receiver (CR) technologies. Accompanying such change of technology is the ability to reach significantly higher heat transfer fluid temperatures by employing molten salt as heat transfer fluid (HTF). As with the PTC, also with CR, the HTF limitations dictated the operating temperature of the receiver outlet temperature. Figure 1.1a illustrates on the left hand side the growing global deployment and on the right hand side the switch in technologies, away from the PTC (the currently dominant technology) to predominantly CR based systems. This trend is explained by the higher plant performance and thereby reduced LCOE is expected from these plants.

[1]Parts of this chapter have been published in Lubkoll *et al.* (2014)

Stellenbosch University https://scholar.sun.ac.za

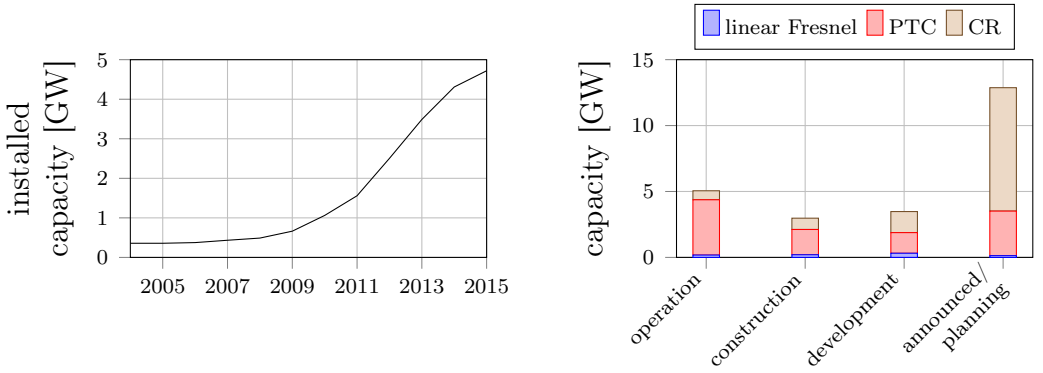

(a) Global installed CSP capacity (b) CSP technology trends

Figure 1.1: The installed global CSP capacity until 2015 (a) as well as the CSP technology trends (b), where plants under operation, construction, development and announced/planned CSP plants are listed[2].

This current generation of CSP CR plants operates with molten salt as HTF, as well as sensible thermal storage medium (using a two tank system). A molten salt to steam heat exchanger is used to drive a Rankine cycle (RC). Material limitations restrict such plants to typical operating temperatures of 565 °C.

This high innovation rate in CSP technologies partially explains a slow reduction in LCOE for CSP in general, as new, innovative plants tend to be first-of-a-kind systems. Furthermore, cost reduction can be achieved by an increased large scale roll out of CSP, as well as further innovation into increasing plant performance.

The latter can be further improved with increasing the thermodynamic conversion efficiency of the power block through increased hot end temperature. The SUNSPOT cycle is a manifestation of a possible next generation CSP CR plant utilizing pressurized air as HTF and an asynchronous combined cycle (CC) for efficient and dispatchable power generation. The SUNSPOT cycle is illustrated in Figure 1.2.

CC CSP plants typically feature an open cycle gas turbine, sucking in ambient air. After the compressor stage, the pressurized air stream is directed to the CR system where it is heated up before returning — should need be, via a combustion chamber — to the turbine stage. The turbine outlet air, as in conventional CC plants is used to drive a steam generator for the bottoming Rankine cycle. With the SUNSPOT cycle, a packed rock bed is intended to serve as a thermal energy storage facility, providing asynchronous operation ability, as well as dispatchability (Kröger, 2012).

[2]Figure 1.1a is based on data provided in Sawin *et al.* (2016). Figure 1.1b is based on current data (November 2016) provided in the CSPtoday project tracker available under http://social.csptoday.com/tracker/projects. Not shown are dish projects due to marginal capacities as well as solar park projects.

Stellenbosch University https://scholar.sun.ac.za

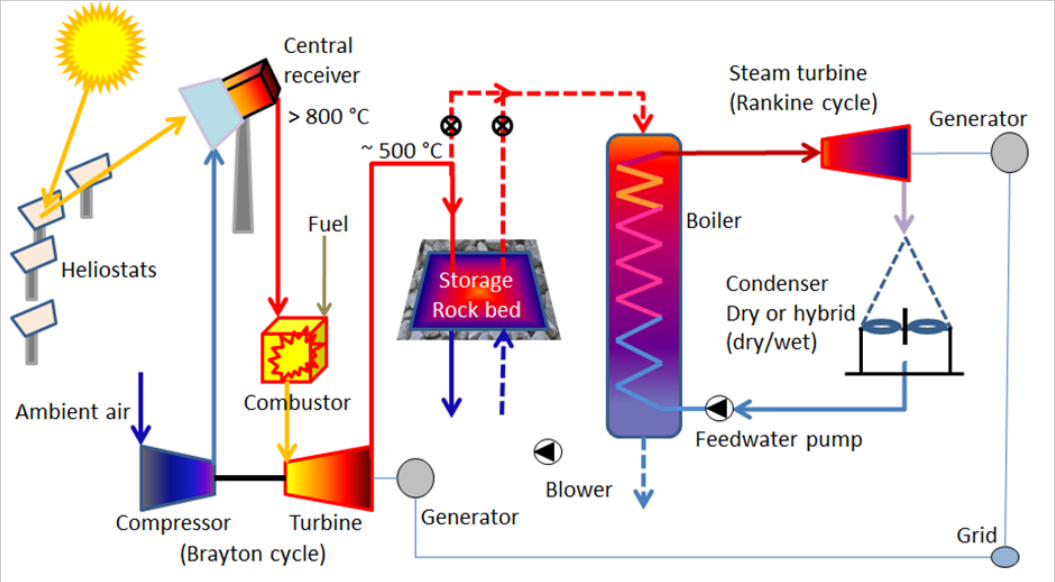

Figure 1.2: The SUNSPOT cycle (Kröger, 2012)

A central receiver technology, heating a pressurized air stream inbetween the compressor and the turbine stage, should be able to heat the air to outlet temperatures of above 1000 °C, while at the same time, operating at a low pressure drop to minimize the performance drop in the Brayton cycle. Such receiver technologies developed to date leave room for improvement as discussed in the technology review. The proposed SCRAP receiver is an attempt to overcome weaknesses of the current technologies.

1.2 Review of pressurized air receiver technology

A common goal for developing a central receiver is maximized central receiver system solar-thermal efficiency. This review describes initially the relevant optical and thermal losses influencing that efficiency. Following this review is an overview of central receiver design classifications and absorber systems.

Numerous criteria influence the design of a central receiver system. Among the most important are the choice of the heat transfer fluid, its required temperature, the receiver capacity and the heliostat field layout. As a result, a variety of concepts for different central receiver applications have been proposed in the past. Consequently, the review on existing concepts is kept to recently developed pressurized air receivers. However, the challenge using air as a heat transfer fluid requires pressurized air receivers to be of a different design when compared to conventional concepts for direct steam generation or molten salt systems. This chapter concludes with the positioning of the SCRAP receiver in comparison to previously developed systems.

Stellenbosch University https://scholar.sun.ac.za

1.2.1 Receiver efficiency

The total losses affecting receiver system efficiency are the optical losses, thermal losses and pumping losses (Stine and Geyer, 2001). The optical and thermal losses are described in more detail below:

- Optical: Reflection, spillage and secondary concentrator optical losses
- Thermal: Radiation, conduction and convection

However, the thermal efficiency (η_{thermal}) is the most widely used value in literature to compare different receivers, regardless of the concentrator configuration (e.g. heliostat type, heliostat field layout, secondary concentrator). The thermal efficiency of a receiver system is described as the ratio of usable thermal energy generated $\dot{Q}_{\text{out}}$ to the impinging concentrated radiation $\dot{I}_{\text{in}}$ onto the receiver aperture:

$$\eta_{\text{thermal}} = \frac{\dot{Q}_{\text{out}}}{\dot{I}_{\text{in}}} \tag{1.1}$$

It is apparent that the thermal efficiency does not include optical characteristics of the heliostat field or a secondary concentrator. These are incorporated in total system efficiency.

The optical loss of solar re-reflection from the receiver is typically represented as part of the thermal efficiency, while the remaining optical losses only appear in a total efficiency analysis. When investigating an entire plant, the heliostat field efficiency needs to be considered. Heat transfer fluid pumping power can be classified as a parasitic loss of the system, or in case of a pressurized air receiver as the pressure drop that directly impacts the thermodynamic cycle's efficiency.

Optical losses of a receiver are determined by reflection, spillage and the optical efficiency of a secondary concentrator.

Low reflective losses (equaling high absorptance in the spectrum of the incoming radiation) are achieved in two ways. One attempt is the application of a selective coating to the absorber surface, improving the absorptive capabilities of the absorber directly, while providing low emittance values at the temperature range of the material. Another way frequently employed is the trapping of radiation by the application of coatings that form microscopic voids, thus increasing the absorptivity (Duffie and Beckman, 2006).

Spillage losses represent the fraction of sun beams reflected by the heliostat field that misses the absorber target. Typically, spillage losses are not accounted for in the receiver efficiency, η_{thermal}, but are represented in a total systems analysis. Heliostats at different distances to the tower cast images of different sizes and shapes onto the absorber. Advanced algorithms are used to target different heliostats onto specific points on the receiver in an attempt to generate

Stellenbosch University https://scholar.sun.ac.za

a homogeneous flux distribution over the absorber surface. This leads to spillage of radiation to areas not covered by the absorber.

A secondary concentrator, also referred to as compound parabolic concentrator (CPC), can be utilized to increase the flux on receiver systems of limited size. A CPC's optical losses, which can be in the range of 15 % (Ávila-Marín, 2011) are not included in the receiver efficiencies, as the flux on the CPC outlet is used to compute the thermal efficiency.

The optical losses of the CPC as well as spillage are not included because their magnitude relies on the heliostat field layout and the aiming strategy of the heliostats. While spillage losses are usually small (Stine and Geyer, 2001) and apply to a certain degree to any receiver design, CPC losses can be significant (Ávila-Marín, 2011; Hischier *et al.*, 2012).

Thermal energy losses of a receiver system are compounded of thermal radiation, conduction and convection losses. Conductive losses result from the absorber mounting to the tower structure. These are losses of minor nature and are often neglected (Solgate Report, 2005). Convective heat losses are losses to ambient air from heated exposed receiver surfaces. Radiative heat losses occur from hot receiver surfaces towards the environment.

The magnitude of the different thermal energy losses depends on the absorber properties, the receiver surface area and geometry, as well as the receiver temperature. Convective and conductive heat losses are directly proportional to the surface temperature. On the other hand, radiative heat losses are proportional to the difference of the fourth power of surface temperature to the fourth power of ambient temperature (or corresponding surface). As a result, different system target temperatures may result in diverse ideal receiver designs, depending on the dominance of the particular losses in each situation.

Heat transfer fluid pumping losses can be of relevance in terms of parasitic losses or, as in the case of a Brayton cycle, directly reducing the pressure ratio on the turbine side. The Brayton cycle efficiency is sensitive to pressure drop, therefore a low pressure drop forms a primary design goal when developing receiver systems.

Stellenbosch University https://scholar.sun.ac.za

1.2.2 Overview of generic receiver concepts

The central receiver concepts of interest for a pressurized air system are reviewed. The overarching concepts of external and cavity receivers are first discussed, before elaborating on proposed concepts.

External receiver

The conventional external receiver is the simplest and cheapest receiver design, where the absorber system, usually numerous vertical tubes, is externally mounted to the receiver tower. This can be done in variations such as the so called "billboard" receiver, where a flat panel of parallel aligned tubes is exposed in the direction of a polar heliostat field. For a surrounding heliostat field multiple similar panels can be mounted to cover larger areas, e.g. reproducing a rectangular or cylindrical shape (as shown in Figure 1.3 for a direct steam generation (DSG) system).

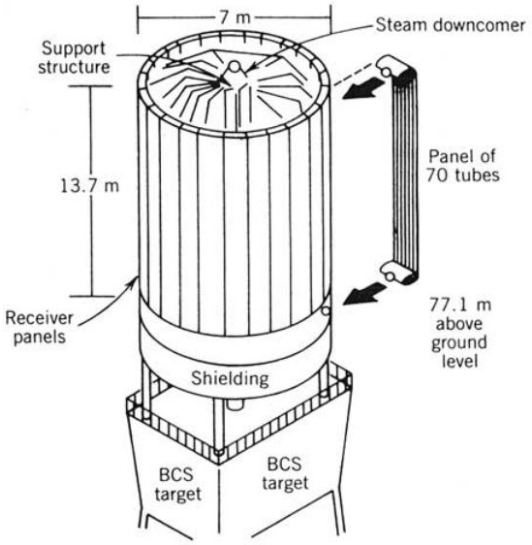

Figure 1.3: Cylindrical external receiver, here for the application of a direct steam generation plant. Heliostat calibration target (BCS target) below the receiver is shown (Stine and Geyer, 2001).

The external receiver concept shows high exposure of the absorber tubes to ambient. This results in high heat losses by means of convection and radiation. Since these are functions of the exposed surface area and temperature, external receiver systems require heat transfer fluids capable of removing heat effectively in order to reduce both, the absorber surface temperature and the total absorber surface. Presently, external receivers are widely used for molten salt and DSG systems (both operating below 600 °C). Thermal efficiencies in the region of above 80 % can be achieved with existing designs (Lata *et al.*, 2008).

Stellenbosch University https://scholar.sun.ac.za

The external receiver, as shown in Figure 1.3, can utilize a surrounding heliostat field. An advantage that a surrounding heliostat field shows over a polar[3] field is a stable solar field optical efficiency over the course of the day, while a polar heliostat field has a higher noon performance (Vant-Hull, 2012). Hence, employing a surrounding receiver system can allow for an increased optical efficiency of the heliostat field. For large scale plants, the surrounding field becomes inevitable, as the distance of the farthest heliostats grows too large for efficient operation.

A conventional external receiver is not suited for low heat transfer coefficient fluids, such as air, as the required large exposed absorber surfaces would lead to significant heat losses.

Cavity receiver

A cavity receiver is a receiver system where the absorber system is encased inside a space with an opening towards the heliostat field. A simple cavity receiver is an encased flat absorber panel on one wall and an opening (aperture) on the opposing side, as shown in Figure 1.4. Having the absorber system encased, can improve the thermal efficiency by means of reducing the convective heat loss (which can further be enhanced by a window in the opening), as well as by trapping reflected light and radiated heat.

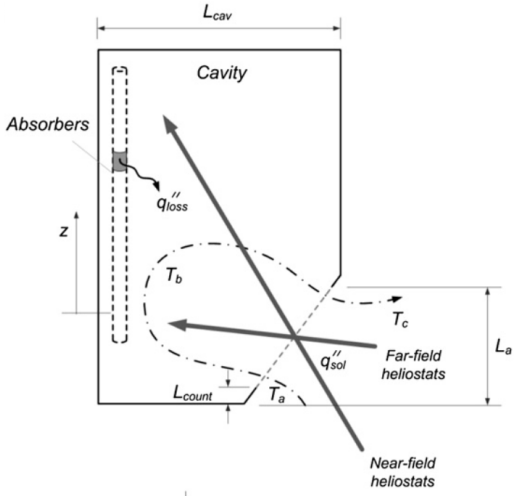

Figure 1.4: Cavity receiver (Soo Too and Benito, 2013)

At a more sophisticated level, high temperature systems such as pressurized air receivers have been conceived as cavity receivers (see chapter 1.2.4).

[3]A heliostat field that only covers an area to one side of a tower is referred to as a polar heliostat field. A billboard receiver or a receiver employing a CPC require polar field layouts.

Stellenbosch University https://scholar.sun.ac.za

1.2.3 Overview of generic absorber concepts

An essential sub-system of the receiver of a CSP plant is the absorber. It is employed to effectively transfer the energy of the concentrated sunlight into the heat transfer fluid. The two absorber types commonly employed are then introduced. These are the tubular and the volumetric absorber principles.

Tubular absorber

Current central receiver technologies for molten salt and direct steam generating systems use a number of tubes to form the absorber surface. A multitude of parallel tubes are used to form a billboard receiver or cylindrical receiver (as shown in Figure 1.3). The heat transfer fluid is pumped through the tubes and is heated up in the process. In order to minimize absorber surface area and temperature, fluids with high thermal conductivity are preferred, as they maintain an efficient system.

As shown in chapter 1.2.4, innovations in pipe manufacturing, heat transfer enhancements and intelligent receiver design can make tubular receivers a viable technology for pressurized air systems.

Volumetric absorber

Increasing attention has recently been given to volumetric receiver/absorber systems.

A volumetric receiver utilizes the geometric configuration of a porous absorber material to improve receiver efficiency. A porous surface, allowing the radiation to penetrate into the depth of the absorber, reduces reflection losses. The heat transfer fluid, which is forced through the porous absorber from the irradiated side, provides the highest cooling effect at the exposed surface. The volumetric effect can be described by the peak surface temperature occurring deep in the structure. This results in a lower irradiated (front) surface temperature than the maximum heat transfer fluid temperature (Romero-Alvarez and Zarza, 2007). The described volumetric effect is illustrated in Figure 1.5 in comparison to a tubular absorber.

The volumetric absorber forms a radiation trap for reflected light beams and radiated heat. It furthermore does not expose the highest temperature parts of the system, reducing the exposed surface temperature and with that heat losses.

A volumetric receiver can suck in ambient air in an open configuration if atmospheric pressure is desired. If higher pressures are required, as with the implementation in a Brayton cycle, the absorber needs to be sealed from the ambient by a window to maintain system pressure.

Stellenbosch University https://scholar.sun.ac.za

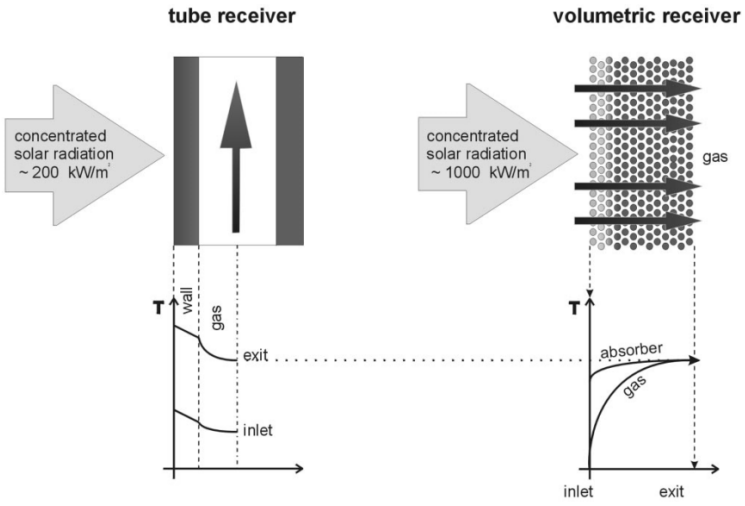

Figure 1.5: Temperature distribution for tubular and volumetric absorber (Romero *et al.*, 2002, based on Hoffschmidt, 1997)

1.2.4 Review of existing pressurized air receiver concepts

The research area of air receiver systems for elevated temperatures, capable of supplying a Brayton cycle, is relatively young. To date, mainly the German Aerospace Center (DLR) and the Weizmann Institute of Science (WIS) have driven development, leading to demonstration scale systems with published findings. Both research institutions have developed cavity receiver systems with volumetric absorber technology, capable of reaching mean outlet temperatures of above 1000 °C. This review covers the progress to date and highlights important problems encountered.

Possible target outlet temperatures of receiver systems can be gas turbine operating temperatures in a range of 1000 °C to 1350 °C (Kribus *et al.*, 1998). The gap between the lower air temperature after a solar receiver and the turbine requirement is usually overcome by introducing a fuel combustor.

Before describing the progress of the research on pressurized air receiver systems in more detail, a summary of the reviewed projects is provided in Table 1.1.

Stellenbosch University https://scholar.sun.ac.za

Table 1.1: Important pressurized air receiver projects

Project	Receiver	Receiver type	Temperature achieved	Project start
DIAPR	DIAPR	Volumetric cavity	1200 °C	1992
REFOS	REFOS	Volumetric cavity	800 °C	1996
SOLGATE	two REFOS and pre-heater	Volumetric cavity and tubular cavity	1030 °C	2001
SOLHYCO	SOLHYCO	Tubular cavity	800 °C	2006
SOLUGAS	SOLUGAS	Tubular cavity	800 °C	2008
SOLTREC	SOLUGAS and REFOS	Volumetric cavity and tubular cavity	unknown	2010

Attempts by DLR

The DLR began tests on volumetric pressurized air receiver systems in 1989 with the PLVCR5 receiver, which employed a dome-shaped quartz glass window (Pritzkow, 1991). The receiver concept has since been continuously improved, and the current version is known as the REFOS receiver, shown in Figure 1.6. The volumetric absorber material used in the receiver can be either a silicon-carbide (Si-C) ceramic mesh for high temperatures or a metal wire mesh for pre-heating purposes.

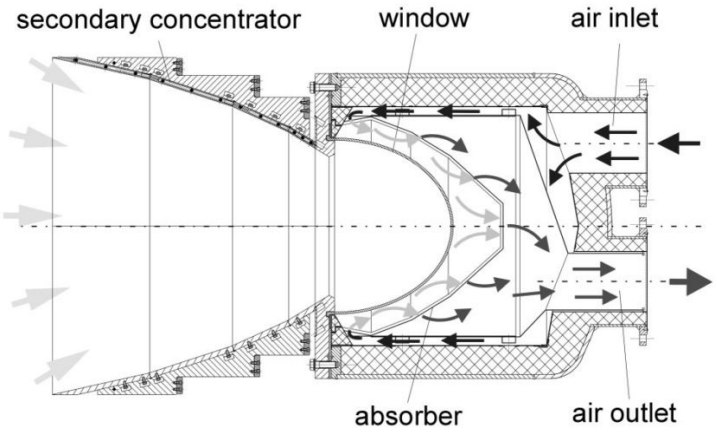

Figure 1.6: The REFOS receiver (Buck *et al.*, 2002)

The REFOS receiver has been successfully operated at up to 1030 °C (Heller, 2010). In the SOLGATE project, a hexagonal compound parabolic concentrator

Stellenbosch University https://scholar.sun.ac.za

(CPC) and two pre-heating sections (with identical CPCs) were included into the setup. The receiver cluster consisted of a multi-tube coil pre-heater (Figure 1.7), a medium temperature REFOS pre-heater and a high temperature REFOS receiver. The goal of employing two pre-heating sections of different technologies was to achieve cost reduction over the high temperature REFOS receiver technology.

The aforementioned tubular pre-heating section was not satisfactory. One problem encountered was its high pressure drop of 70 % of the total cluster pressure drop (120 mbar) (Solgate Report, 2005). Furthermore, the tube surface temperature peaked at 400 K above the air outlet temperature (Solgate Report, 2005). More importantly, the cross-sectional temperature gradient between the radiated and unradiated pipe surface was calculated at up to 220 K, resulting in high thermal stresses, thereby reducing the receiver lifetime (Heller, 2010).

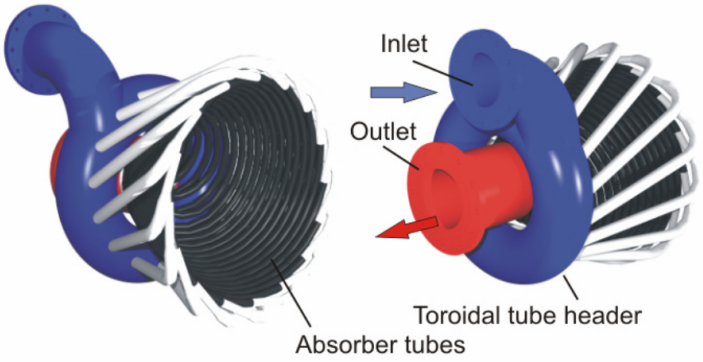

Figure 1.7: The SOLGATE multi-tube coil receiver (Solgate Report, 2005)

In the following projects, SOLHYCO (Heller, 2010) and SOLUGAS (Korzynietz *et al.*, 2012) (Figure 1.8), a new tubular cavity type receiver was developed by the DLR in cooperation with, among others, the Spanish company Abengoa Solar.

The new SOLUGAS receiver was meant to replace the tubular cavity receiver pre-heater and the REFOS receiver pre-heating stage of the SOLGATE project. It was intended to bring the pre-heated temperature in one step to about 800 °C (Korzynietz *et al.*, 2012). The SOLHYCO receiver design was similar to the SOLUGAS receiver with the same target temperature, but with a designation as a sole heating stage for micro-turbines. One innovation in the SOLHYCO receiver was a three-layered pipe (PML-pipe) of Inconel-Copper-Inconel, where the copper's high conductivity was employed to reduce the circumferential temperature gradient on the absorber pipe. However, thermal cycling caused cracking of the PML tube between metal layers (Heller, 2010). The following SOLUGAS project employs conventional pipes and has ended in April 2013, with a final report yet to be published. The follow-up-project was SOLTREC, where the SOLUGAS receiver and the REFOS receiver were installed in series

Stellenbosch University https://scholar.sun.ac.za

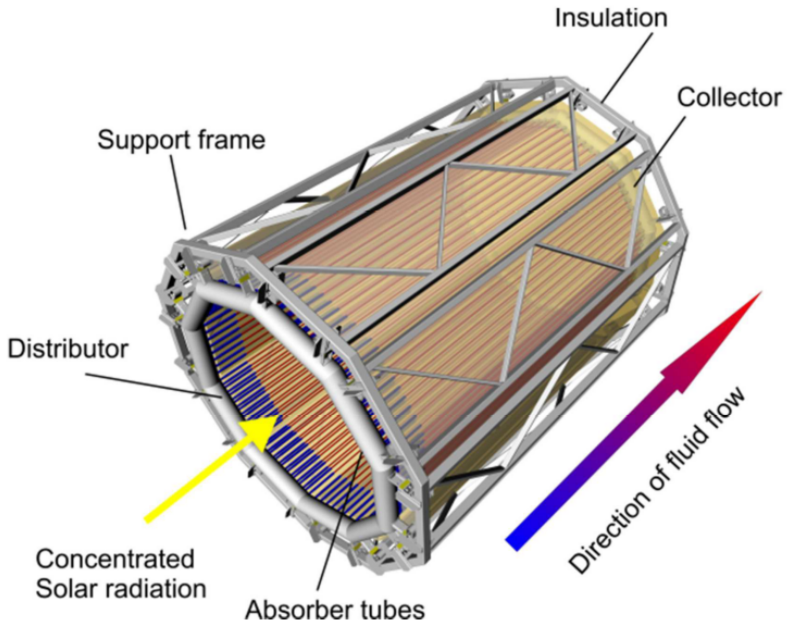

Figure 1.8: The SOLUGAS receiver (Korzynietz *et al.*, 2012)

at the Plataforma Solar de Sanlúcar la Mayor (PSSM). The target of the SOLTREC project was to achieve a mean air temperature of 1000 °C. The SOLUGAS receiver was successfully operated at air outlet temperatures of 800 °C (Korzynietz *et al.*, 2016).

The solar-thermal efficiency of the SOLUGAS receiver reached just below 80 % during testing which uses the flux on aperture as reference. During the same test series the receiver system pressure drop was measured at around 200 mbar (Korzynietz *et al.*, 2016). The similar, but smaller, receiver of the SOLHYCO project had an expected thermal efficiency of 67 % to 80.8 % (without and with a quartz window enclosing the aperture). These values were grossly missed with measured efficiencies of 37 % to 45 % respectively (Heller, 2010). Continued research on the SOLUGAS receiver in the current SOLTREC project suggests that some parts of that efficiency discrepancy and low target temperature performance are hoped to be eradicated.

The thermal efficiency of the SOLGATE cluster with the now abandoned tubular pre-heater was 78 % at 800 °C outlet air temperature and 72 % at 900 °C outlet air temperature (Heller *et al.*, 2006). Buck *et al.* (2002) stated an efficiency goal for the REFOS receiver (without a pre-heater system) of 80 % at 800 °C, including the optical losses of the CPC but did not report test results. Deducting the CPC's optical losses, the mentioned value of 80 % suggests a high thermal efficiency of the REFOS receiver in the range of 90 %. A typical flux density for the REFOS receiver was below 1000 kW/m^2 after the secondary concentrator (Solgate Report, 2005).

Stellenbosch University https://scholar.sun.ac.za

The quartz glass of the dome-shaped window (see Figure 1.6) needs to withstand high temperatures and pressures in order to separate the hot pressurized air flow (up to 20 bar) from ambient. The quartz glass is barely addressed in publications regarding the REFOS receiver. It has, however, shown to be a limiting factor to receiver dimension. Quartz glass (fused Silica SiO_2) is the only glass of sufficiently high allowable temperature, high transmittance and low thermal expansion (Hofmann *et al.*, 2009). Observation of the REFOS receiver over a total operating time of 500 h at air outlet temperatures of 600 °C to 800 °C resulted in the following findings:

- Burning-in of surface contamination that cannot be cleaned out (resulting in an increase in absorption);
- Microscopic fabrication defects that grow during thermal cycling;
- Active cooling requirement of the glass;
- Sensitivity to thermal shock;
- Size limitation of the glass due to manufacturing constraints.

With the mentioned 500 h of test time, representing about 60 days of normal operation, deterioration was already visible within a fraction of a plant's lifetime (Hofmann *et al.*, 2009). Concerns are that besides deterioration of the optical quality, cracking of the window occurs under pressure and high solar flux density (Grange *et al.*, 2011).

The diameter of the REFOS quartz glass window was 620 mm in the first generation (Ávila-Marín, 2011) and has recently been increased to 816 mm (Río *et al.*, 2015). For unpressurized systems higher diameters are possible. For example the SOLUGAS receiver design was considered with a quartz glass window covering its 5 m diameter opening.

The DIAPR receiver

In parallel to the DLR, the WIS (Weizmann Institute of Science) developed a pressurized air volumetric cavity receiver, the Directly Irradiated Annular Pressurized Receiver (DIAPR). The DIAPR is based on the porcupine model, where concentrated solar radiation impinges on high temperature resistant alumina-silica pins (Karni *et al.*, 1998). The pressurized air stream is guided past the pins and is heated up in the process. The cross-section of a DIAPR is shown in Figure 1.9.

The DIAPR was the first receiver to exceed test temperatures of 1200 °C (Kribus *et al.*, 2001) and can handle extraordinarily high flux densities of up to 10 MW/m^2 (Karni *et al.*, 1997). In an attempt to increase the system efficiency, a multistage DIAPR was developed that employed, similarly to the DLR approach, a coiled tubular cavity pre-heater (Kribus *et al.*, 1999).

Stellenbosch University https://scholar.sun.ac.za

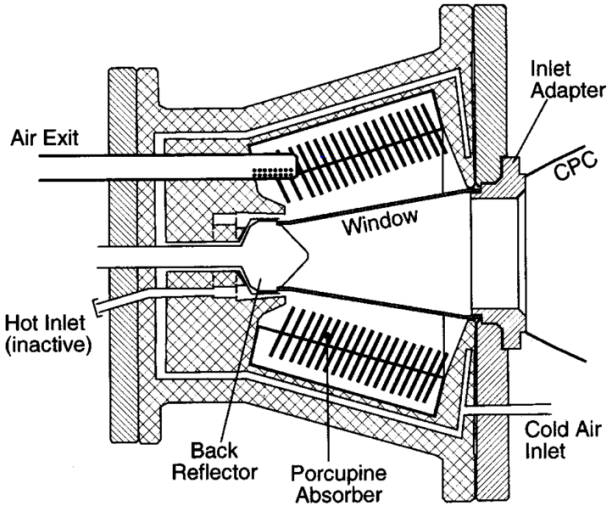

Figure 1.9: The DIAPR receiver in cross-section (Kribus *et al.*, 2001)

Efficiency information on the cluster or the pre-heater is not available. The DIAPR receiver without a pre-heater has a stated thermal efficiency of 70 % to 90 % between 850 °C and 1200 °C respectively, while Kribus *et al.* (2001) expected values of 85 % to 90 % with improved CPC optics. These values were provided for a flux density of 5 MW/m^2 on the receiver aperture. The downside of high flux densities is that the required concentration ratios lead to increased shading and blocking in a denser heliostat field, as well as increased spillage losses at the CPC aperture (Pitz-Paal *et al.*, 2011). In the case of the DIAPR prototype testing, 60 % of the concentrated beams were lost to spillage (Kribus *et al.*, 2001).

Even though the DIAPR also utilizes a pressurized fused quartz glass, no concerns with regards to its durability were mentioned, and even up-scaling of the receiver was discussed. The capability of the window to withstand pressures of up to 50 bar was stated and high temperature tests were conducted at 17 bar to 20 bar (Kribus *et al.*, 2001). During the tests, the DIAPR receiver was operated for a significantly shorter time than the REFOS receiver. It is therefore unknown whether the DIAPR's quartz glass window can sustain long-term operation.

While further work has been proposed, no new information on development progress with regards to the DIAPR system has been published in recent years. The DIAPR technology was recently implemented in the 100 kW_e AORA Solar micro-turbine central receiver system (Ávila-Marín, 2011). AORA, to date, built two pilot plants in Israel and at Plataforma Solar de Almería (PSA) in Spain (Aora-Solar, 2011). AORA has not released information on their system to the public.

Stellenbosch University https://scholar.sun.ac.za

Other recent receiver concepts

With increasing attention to the development of pressurized air receivers, new concepts were recently proposed. These concepts are, due to lack of supportive test results, only briefly explained.

In 2012, the DLR has presented the concept of a pressurized ceramic receiver that can be implemented within the cavity of the SOLUGAS cavity receiver. Pre-heated air is ducted from the SOLUGAS receiver at 800 °C through channels inside the ceramic absorber bodies to be heated up to 1200 °C (Jensch *et al.*, 2012). Further results, limitations and capabilities of the system are not provided.

The Australian Commonwealth Scientific and Industrial Research Organisation (CSIRO) is developing a solar Brayton cycle system in cooperation with the Japanese Mitsubishi Heavy Industries (MHI). MHI is supplying a pressurized air receiver based on a tubular absorber in a cavity (as shown in Figure 1.4). The targeted and achieved outlet temperature is 850 °C (Stein *et al.*, 2010; Nakatani *et al.*, 2012). Further information on performance is not provided.

In the PEGASE project, the development of a pressurized air receiver, based on compact heat exchanger technology, is pursued by the French CNRS/PROMES. Similar to the earlier described multi-layered PML-tube (SOLHYCO and SOLUGAS receiver), the PEGASE receiver consists of panels with an irradiated nickel-based super-alloy absorber surface and a copper core through which super-alloy tubes are ducted, carrying the pressurized air (see Figure 1.10). The tubes are small with an inner diameter of 6 mm (Bellard *et al.*, 2012). The proposed system is claimed to provide an output temperature of 750 °C at a pressure drop of 300 mbar (Bellard *et al.*, 2012). CFD simulations by Grange *et al.* (2011) resulted in a predicted thermal efficiency of 81.3 %. The thermal efficiency and durability of the material bonds are yet to be confirmed by tests. The experiments reported on in Bellard *et al.* (2012) highlight problems with unexpected high pressure drop, but no information on thermal efficiency of the system has been provided.

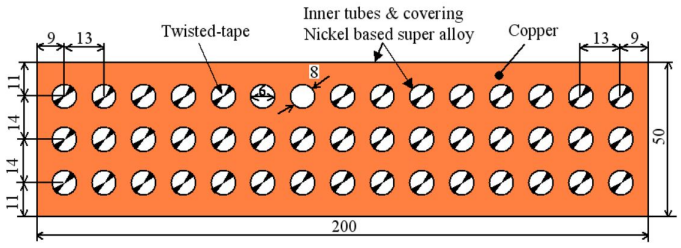

Figure 1.10: Structure of the multi-layer PEGASE absorber with shown dimensions in mm (Bellard *et al.*, 2012)

Stellenbosch University https://scholar.sun.ac.za

Hischier *et al.* (2012) proposed a cavity receiver design with a similar absorber system approach to the PEGASE receiver. The absorbed radiation in a cylindrical cavity receiver is conducted into an annular reticulate porous ceramic (RPC) foam material (SiC), through which the pressurized air is sucked and in the process heated up (see Figure 1.11). The ceramic foam is shielded from the cavity by the absorber surface. Small scale laboratory testing has been conducted with a $3\,\mathrm{kW_t}$ receiver prototype. Hischier *et al.* (2012) predicted thermal efficiencies in the range of 74 % to 90 % for air outlet temperatures between 967 °C and 1437 °C for a $100\,\mathrm{kW_t}$ receiver.

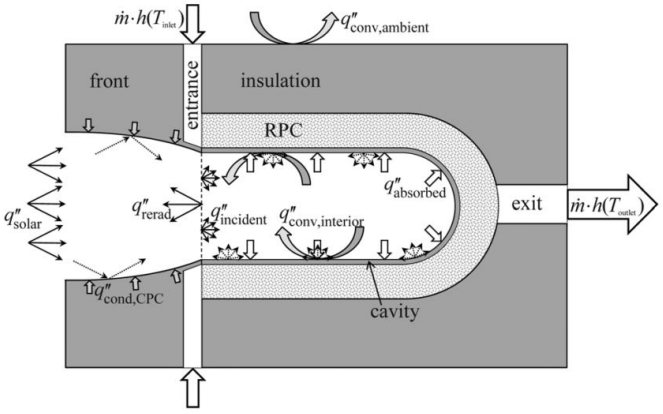

Figure 1.11: Schematic of the RPC receiver (Hischier *et al.*, 2012)

Stellenbosch University https://scholar.sun.ac.za

1.2.5 Conclusion on review of current systems

The field of pressurized air receivers is relatively young, with only two research institutions driving development to prototype and demonstration scale. No commercialized system for utility scale operation is available as yet.

Generally, limited information is available on the proposed systems. With regards to the high temperature volumetric cavity receivers, this is especially the case for the DIAPR system. No additional information on the DIAPR receiver has been published and no further research projects have been announced. The limited long-time testing of the REFOS receiver has already indicated limitations to the durability of the quartz glass window, adding to the problems with robustness and practicability of the window.

The tubular pre-heating sections are equally poorly discussed in literature. Unfortunately, the efficiency of the DIAPR's pre-heater section is not known, as the incidence flux could not be measured during tests (Kribus *et al.*, 1999). None of the DLR's tubular pre-heaters of the SOLGATE, SOLHYCO and SOLUGAS systems provided satisfactory results to date.

It can furthermore be concluded that the volumetric receivers and tubular pre-heaters proposed by DLR and WIS (and in fact also the new approaches introduced in Section 1.2.4) are cavity receivers, mostly equipped with secondary concentrators. None of the reviewed receivers are designed for a large scale surrounding heliostat field, which provides higher annual energy collection, compared to a polar field (Vant-Hull, 2012).

The conducted review of developed receivers highlights that there is a need for a central receiver that meets the following requirements:

- Effective transfer of the thermal energy that has been generated by the heliostat field;
- Utilization of the higher efficiency of a surrounding heliostat field and avoiding optical losses of secondary concentration;
- Robust, practical and cost efficient technology that is not dependent on sensitive plant elements such as quartz glass windows;
- A low pressure drop in the receiver.

Stellenbosch University https://scholar.sun.ac.za

1.3 Motivation - the SCRAP receiver concept

The SCRAP receiver, as conceived by Prof. Kröger (2008), is a novel receiver concept that addresses the shortcomings of the current receiver generation.

The SCRAP receiver concept utilizes a multitude of tubular absorber assemblies (spikes) that protrude concentrically from the receiver center. A possible layout of the SCRAP receiver is shown in Figure 1.12.

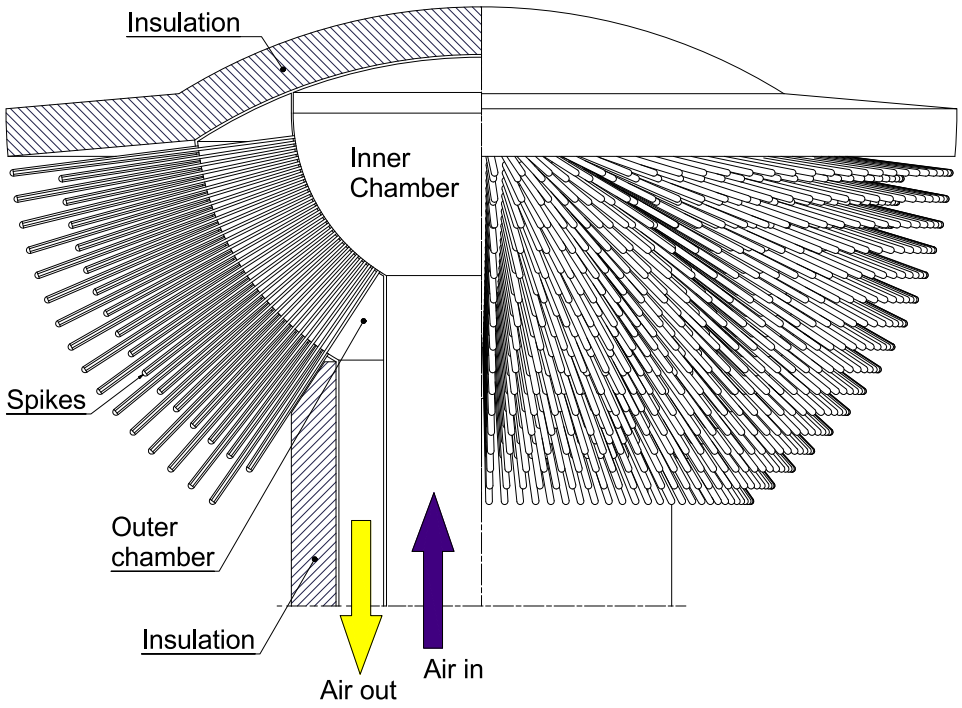

Figure 1.12: SCRAP receiver (left half in cross-section) (Kröger, 2008)

As described by Kröger (2008), each spike consists of two concentric tubes, where the inner tube supplies the cold air stream to the spike tip from where the air flow is directed back towards the receiver center through the outer tube. The outer tube's surface is exposed to the concentrated irradiation, and in the process heated up, transferring thermal energy into the air stream. In order to enhance the heat transfer, the outer tube is internally finned, as shown in Figure 1.13.

The SCRAP receiver can be classified as an external macro-volumetric tubular pressurized air receiver. The spikes imitate a porous surface, allowing the concentrated sun beams to penetrate deeply into the structure. Furthermore, the highest cooling effect of the cold pressurized air is attained at the most exposed element, the spike tips. The air stream is heated as it flows through the internally finned tubes from the tips towards the receiver center. As a result, the highest air and absorber temperatures are expected at the spike outlets into the outer receiver chamber, thus improving the volumetric effect.

Stellenbosch University https://scholar.sun.ac.za

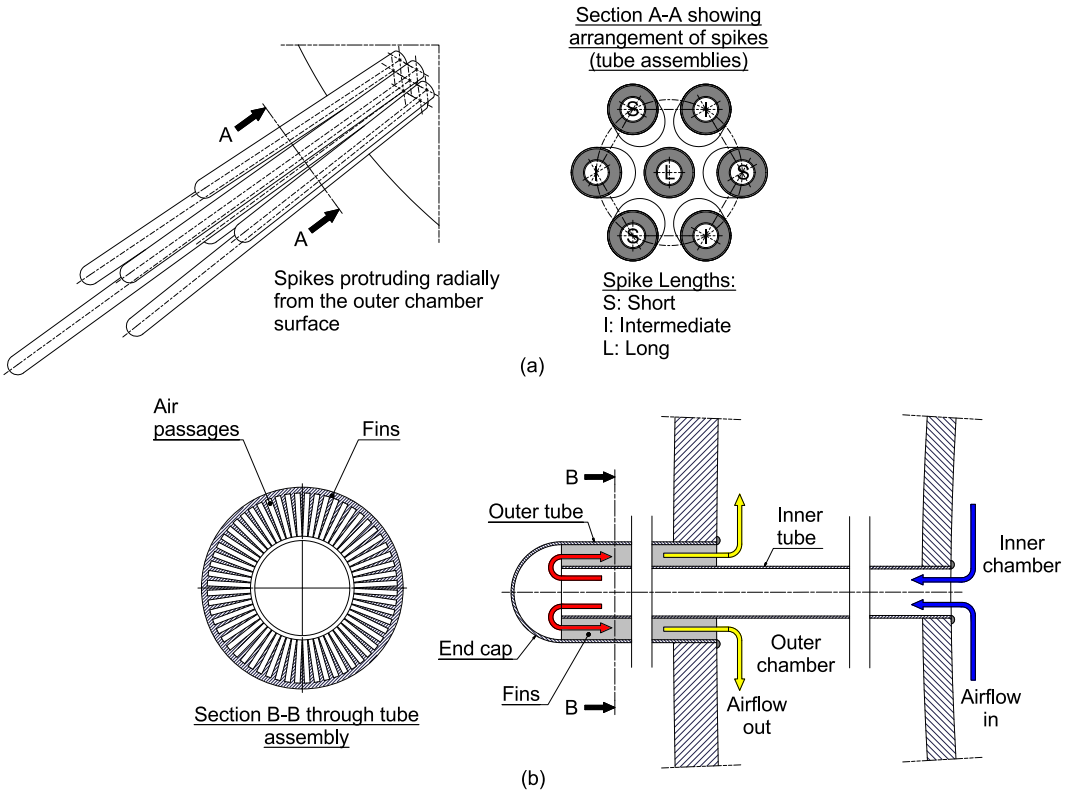

Figure 1.13: SCRAP tube assembly (spike) details: (a) tube arrangement, (b) tube geometry (Kröger, 2008)

With the highest pipe surface temperature experienced in the area of the lowest irradiation, higher fluxes may be tolerated without causing absorber pipe overheating.

In principle, a similar, but geometrically less pronounced, concept has been developed for molten salt receivers by Garbrecht *et al.* (2012). In this concept, internally finned pyramidal shapes are used to trap thermal energy and reflection (see Figure 1.14).

Stellenbosch University https://scholar.sun.ac.za

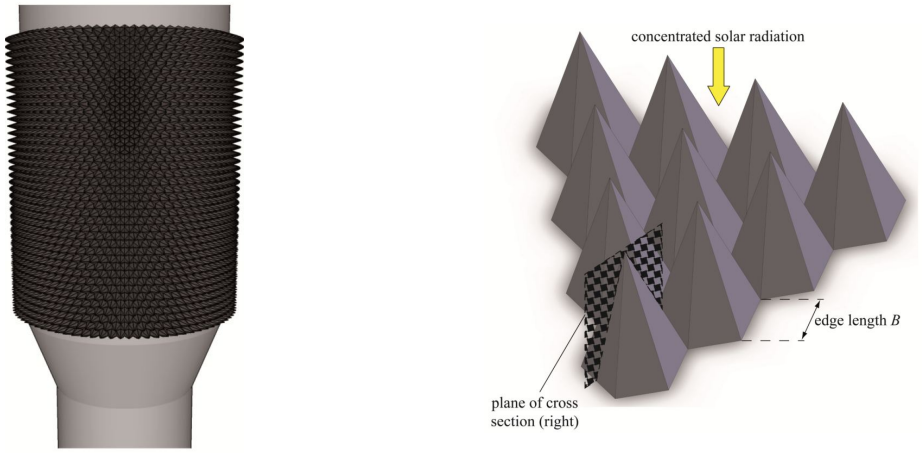

Figure 1.14: Cylindrical central receiver (left) with pyramidal absorber shapes (right) (adapted from Garbrecht *et al.*, 2012)

The simulation by Garbrecht *et al.* (2012) predicts an overall efficiency improvement when compared to a standard external tubular receiver (see Table 1.2). It is noteworthy that the highest heat loss was shifted from radiation heat loss to convection heat loss. With the radiation heat loss being dependent on the temperature to the power of four, this is an important achievement for systems operating at temperatures above the molten salt levels of 565 °C. The comparison of the results of Garbrecht *et al.* to the estimated losses of the Gemasolar plant researched by Lata *et al.* (2008) is given in Table 1.2.

Table 1.2: Losses of an external cylindrical molten salt receiver and a macro-volumetric external pyramidal molten salt receiver

Loss type	Gemasolar (Lata *et al.*, 2008)	Pyramidal (Garbrecht *et al.*, 2012)
Reflection	6.0 %	1.3 %
Convection	1.9 %	4.8 %
Radiation	4.8 %	2.8 %
Thermal efficiency	87.3 %	91.2 %

The SCRAP receiver and the receiver of Garbrecht *et al.* (2012) share a unique feature of reproducing a volumetric receiver effect in macroscopic dimension that can utilize a surrounding heliostat field.

The SCRAP concept is the only concept for a pressurized air receiver that operates without the requirement of a quartz glass window and the efficiency penalty of a CPC, which can both be necessitated by an enclosing cavity. The

Stellenbosch University https://scholar.sun.ac.za

research of Garbrecht *et al.* (2012), with their design developed for a molten salt system, supports the concept of the SCRAP system by having shown that the desired trapping effects of radiation (incoming solar and thermal between spikes) can be created.

The SCRAP receiver can be envisaged as the sole receiver to a CSP plant, where a combustor increases the air temperature to the required level. If a higher solar share is intended, SCRAP can be implemented as a pre-heater to a high temperature receiver, for example a REFOS or DIAPR type receiver. The upper operational temperature limit has to be established.

The SCRAP receiver is a novel solution to provide an efficient and robust receiver that does not require a quartz-glass or secondary concentration, can withstand high flux, and operate with an efficient surrounding heliostat field.

Stellenbosch University https://scholar.sun.ac.za

1.4 Objective

The research is divided into a number of objectives to build a knowledge foundation to confidently answer the overarching research question:

- Is the novel SCRAP central receiver a feasible concept for application in a concentrating solar power plant with pressurized air as the heat transfer fluid?

The key objectives leading to the ability to answer the research question are:

- Developing an understanding of solar flux on spikes;
- Development of an appropriate solution to achieve sufficient spike tip cooling;
- Developing an understanding of the sensitivities of geometric parameters onto spike performance;
- Prediction and improvement of receiver efficiency under reference conditions.

Stellenbosch University https://scholar.sun.ac.za

1.5 Methodology

A computer simulation was developed to predict the performance of the SCRAP receiver by investigating a spike under design point conditions. To this end, a ray-tracing study was conducted in an effort to understand sensitivities of the receiver to the heliostat field and the heliostat's dimensions.

The simulation model for the spike was expanded to include heat loss to ambient, as well as radiative thermal interaction with neighboring spikes to permit efficiency computation. To confirm the computer model, a laboratory test setup was developed and built. The experimental apparatus was conceived to validate the air-flow model as well as the heat transfer model, by measuring temperatures as well as static pressure at numerous points.

In conclusion, a sensitivity analysis was conducted to enable the proposition of an improved spike geometry.

Stellenbosch University https://scholar.sun.ac.za

Stellenbosch University https://scholar.sun.ac.za

Chapter 2

Modeling[1]

Concentrating Solar Power systems are complicated systems where subsystems depend on design and performance of other subsystems. To establish an environment to analyze the potential of the SCRAP receiver a CSP system with a reference SCRAP geometry is initially defined. Such geometry enables to perform a ray-tracing study to develop understanding of the sensitivities of the concentrated solar flux towards changes on the heliostat field. Then, a simulation model can be developed to predict the receiver's performance.

2.1 Reference receiver geometry

The dimensions of the analyzed reference SCRAP receiver geometry are summarized in Table 2.1. The tower height is based on tower heights for existing central receiver installations of similar dimension (see Appendix A).

Table 2.1: Dimensions of the SCRAP receiver for reference design

parameter	unit	value
sphere radius	[m]	2
spike radius	[m]	0.035
spike length	[m]	1.0 to 1.3
tower height	[m]	82 m

Based on a constant flux of $I_{\text{aperture}} = 1\,\text{MW}_{\text{opt}}/\text{m}^2$ at spike tips (radius from sphere center: $r_{\text{tip}} = 3.3\,\text{m}$), the optical power input can be calculated. To do so, the receiver aperture is required. Figure 2.1 illustrates the angles α and β, defining the receiver aperture area.

[1]Parts of this chapter have been published in Lubkoll *et al.* (2014), Lubkoll *et al.* (2015) and Lubkoll *et al.* (2016*c*)

Stellenbosch University https://scholar.sun.ac.za

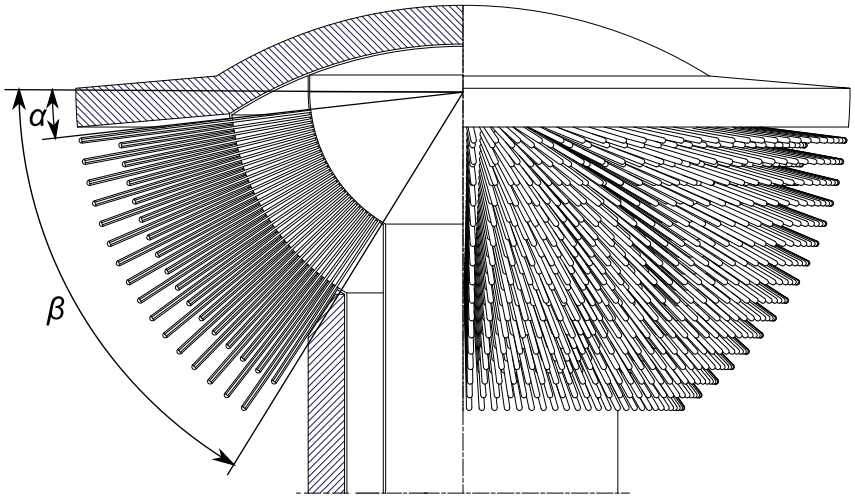

Figure 2.1: SCRAP receiver with the angles α and β describing the receiver aperture

The aperture area can be calculated as

$$A_{\text{aperture}} = \pi \left[\left(r_{\text{tip}}^2 \cos^2 \alpha + r_{\text{tip}}^2 (1 - \sin \alpha)^2 \right) - \left(r_{\text{tip}}^2 \cos^2 \beta + r_{\text{tip}}^2 (1 - \sin \beta)^2 \right) \right] \tag{2.1}$$

where α is assumed with 20° and β with 60°, resulting in an aperture of 35.8 m^2. As a consequence of the assumed constant flux, the total energy impinging on the aperture is

$$\dot{Q}_{\text{opt}} = A_{\text{aperture}} \, I_{\text{aperture}} \tag{2.2}$$

from which the thermal heat rate of the receiver $\dot{Q}_{\text{thermal}}$ can be determined by using the thermal efficiency η_{thermal}:

$$\dot{Q}_{\text{thermal}} = \dot{Q}_{\text{opt}} \, \eta_{\text{thermal}} = A_{\text{aperture}} \, I_{\text{aperture}} \, \eta_{\text{thermal}} \tag{2.3}$$

For lack of — at this point — better knowledge about the receiver performance a thermal efficiency of 80 % is guessed, resulting in a heat rate of $\dot{Q}_{\text{thermal}} = 29\,\text{MW}_\text{t}$.

Stellenbosch University https://scholar.sun.ac.za

2.2 Optical analysis

Ray-tracing software is used to develop an understanding of the impinging flux distribution along a spike and its sensitivity to parameters, such as heliostat size or heliostat field density for a simplified field layout.

The heat transfer analysis of the spikes requires understanding of the distribution of the impinging flux along a spike in order to provide a foundation for the theoretical study. A simplified representative flux model is therefore required.

Ray-tracing software can simulate optically complex environments such as a central receiver plant with a large heliostat field by starting single sun rays at arbitrary locations on a sky plane and following the rays to the point of absorption. While considering effects such as the sun half-angle (of 4.65 mrad) or reflection and blocking of rays by heliostats or other geometry (here, spikes), a ray-tracing analysis can rapidly provide useful results.

The selected software is the open source Monte Carlo ray-tracing software Tonatiuh, developed by CENER for the application in the CSP environment (selection criteria and ray-tracer validation see Appendix B).

2.2.1 Spike distribution

The homogeneous distribution of the spikes over a spherical surface is achieved by representing the spherical surface by a geodesic spherical surface. A geodesic sphere is a representation of an actual spherical surface by triangles (with the vertices located on the spherical surface). For the ray-tracing model a single icosahedron (one out of 20 equilateral triangles that together form a sphere) is further broken down into smaller triangles. This further sub-division of the icosahedra is referred to as the frequency of a geodesic sphere as shown in Figure 2.2.

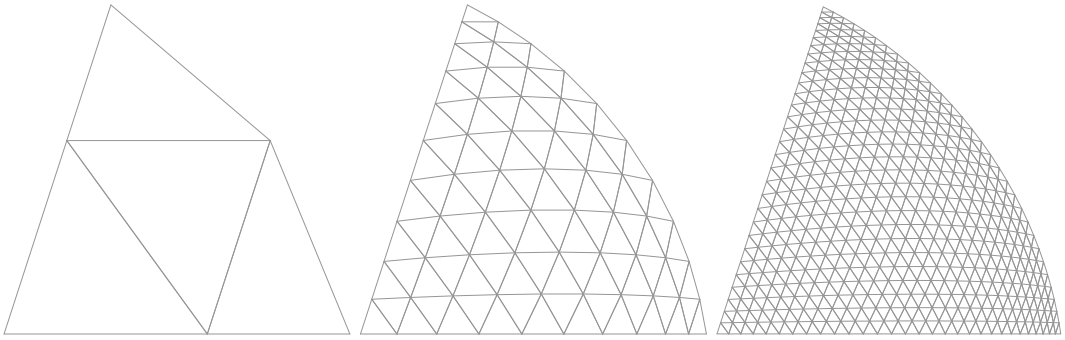

Figure 2.2: An icosahedron divided with frequencies $f = 2$, $f = 10$ and $f = 30$ (from left to right)

The subdivision of a icosahedron is performed by dividing its surface into smaller equilateral triangles and subsequently projecting each vertex onto the

Stellenbosch University https://scholar.sun.ac.za

spherical surface. Inherent to this process is that the projected triangles are not equilateral nor of identical dimension, showing different edge length depending on the position on the sphere. For the investigation of the flux impinging on a single spike this effect is of minor nature.

The software DOME (Bono, 2011) is used to generate an icosahedron of arbitrary frequency, where the vertexes serve as spike root coordinates. Based on the edge length between vertexes (distance between spikes) the frequency of the geodesic icosahedron can be adjusted to achieve a desired spike distance.

2.2.2 Ray-tracing model

The objective of modeling the SCRAP receiver with the ray-tracer is to develop a parametric system that promotes understanding of the flux distribution on the receiver and the system's sensitivities to the important parameters. Tonatiuh provides a built-in toolbox to create simple geometries and assign optical properties to these elements. To generate a flexible solution that allows changing of parameters, Tonatiuh's scripting function is used. The procedure to generate a ray-tracing model and post process the results is depicted in Figure 2.3.

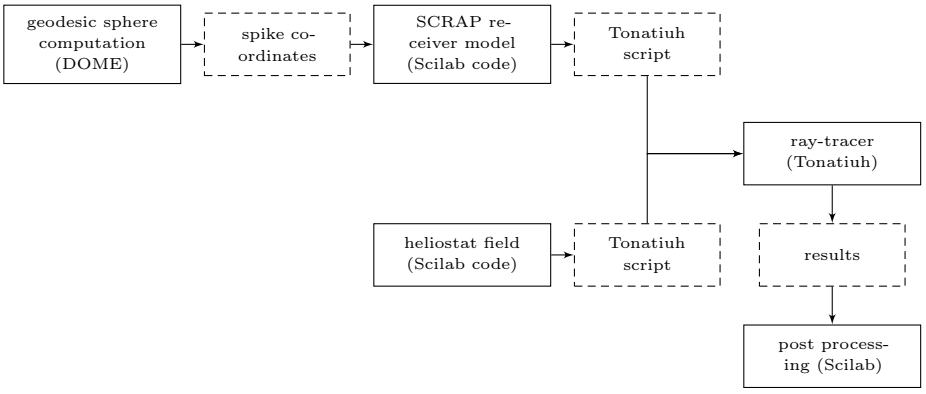

Figure 2.3: Flow chart of different software used to conduct a ray-tracing simulation in Tonatiuh (solid blocks represent computer software, dashed blocks data files).

The Tonatiuh scripting language is limited in functionality, requiring an external model being translated to Tonatiuh code. The SCRAP receiver model further utilizes an input file, containing information on the spike coordinates (as described in chapter 2.2.1). Two Tonatiuh script files were generated, one that models the SCRAP receiver and one that describes the heliostat field, both as the output files of Scilab[2] models programmed for that purpose.

[2]Scilab version 5.4.1, released 2013

Stellenbosch University https://scholar.sun.ac.za

On concluding a ray-tracing simulation Tonatiuh generates a result-file in form of an SQL database. The database stores information on photon power of the rays, the coordinates of ray hit points and information on the hit surface. Utilizing Scilab, the Tonatiuh results are further processed, e.g. to generate flux maps, such as shown Figure B.4.

2.2.3 Ray-tracing setup

A ray-tracing scenario is created that contains a quadratic heliostat field with uniform heliostat spacing in all directions, as shown in Figure 2.4b. A script allows specification of the field dimensions, the heliostat size, the gap size between heliostats and the optical properties. Each heliostat has a single flat facet and is positioned with Tonatiuh's Azimuth-Zenith tracking. All heliostats aim at the centre point of the receiver.

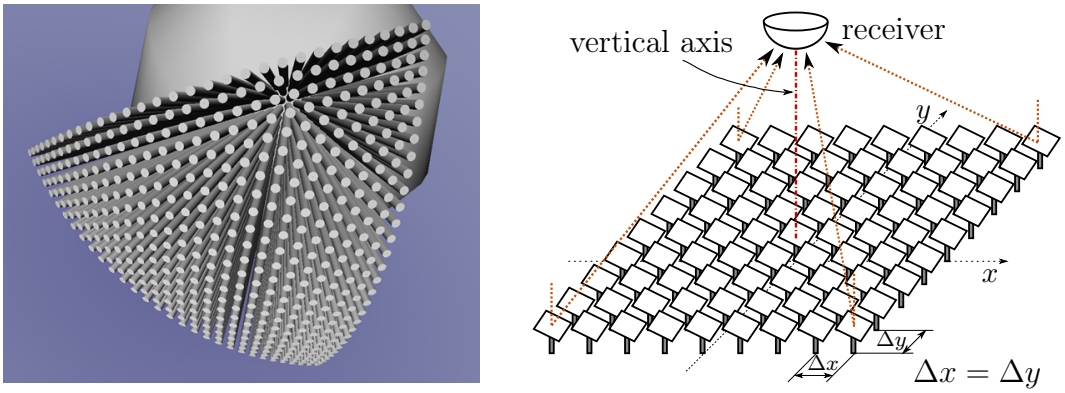

(a) (b)

Figure 2.4: (a) Tonatiuh screen-shot of a SCRAP receiver section (one icosahedron populated with cylindrical spikes) with equal spike length (1.3 m) and (b) visualization of heliostat field with investigated spike pointing along the vertical axis toward the heliostat field

A SCRAP receiver (segment) is situated in the center of the field at 82 m elevation without a tower being modeled. The tower height was established, using a curve fit on towers with surrounding heliostat fields for similar thermal receiver capacity as estimated for a SCRAP receiver. The spikes were then distributed on the surface of that sphere. The spike locations were computed using geodesic coordinates with a frequency of 30. The spikes are 1.3 m long with a diameter of 0.07 m. As all spikes protrude radially from the SCRAP center only a single spike is pointing vertically downwards. The impinging rays on that spike are recorded and saved. This way a uniform representative flux on a spike is achieved which are used as design point conditions. The sun is positioned in zenith with the DNI set at 1000 W/m^2. Mirror reflectivity as well

Stellenbosch University https://scholar.sun.ac.za

as absorptivity of the spikes (and sphere) were set to 0.9 (assuming Pyromark paint. Properties of Pyromark see Appendix N).

The relevant optical as well as environmental parameters for the ray-tracing analysis are listed in Table 2.2 as well as Table 2.3. The used geometry of the SCRAP receiver is listed in Table 2.1. The simulation ignores atmospheric effects influencing transmissivity of air.

Table 2.2: Optical parameters defined for the simulation environment

parameter	unit	value
mirror reflectivity	[−]	0.9
mirror slope error	[−]	0.002
spike absorptivity	[−]	0.9
sphere absorptivity	[−]	0.9

For the purpose of the ray-tracing study the sum of absorptivity and reflectivity was set as one. The reflectivity was specular.

Table 2.3: Environmental parameters for the ray-tracing simulation

parameter	unit	value
sun position	[−]	zenith
I_{DNI}	[W/m^2]	1000
solar half-angle	[mrad]	4.65
sun shape	[−]	pillbox[1]

[1] The pillbox sun shape is a simplified sun shape, considering the radiation from the sun to be constant over the solar half-angle. More realistic and computationally expensive is the Buie sun shape, taking the circumsolar region into consideration.

The geodesic frequency, defining the spacing between the spikes, was selected with $f = 30$, populating an icosahedron with 496 spikes. The spike at the icosahedron's center is the spike analyzed for the flux distribution. There, the distance between two neighboring spikes on their root is 18 mm.

The heliostat field consists of three heliostat sizes of 1 m × 1 m, 2 m × 2 m and 3 m × 3 m heliostats. To establish the heliostat field size the field size is increased. The heliostat field size was manually adjusted until further increase did not lead to change of flux on the investigated spike. Tonatiuh's built in azimuth-elevation heliostat tracker was used to point all heliostat's aim points onto the center point of the receiver.

Stellenbosch University https://scholar.sun.ac.za

2.2.4 Post-processing

The ray-tracing software associates a number with each surface in the ray-tracing model. Each ray impinging on a surface is allocated information of its impingement location in form of spatial coordinates, the surface number, previous surface contact and, should it be reflected, the following surface. Tonatiuh can then be directed to export hit points onto a particular surface of interest in an output file. This is of interest to reduce the output file from multiple GB data volume to some MBs.

The surface of the investigated spike was divided into a mesh, using a Scilab program. An illustration of a mesh is depicted in Figure 2.5. Each cell is an identical sized rectangular cell. The mesh size was set to an arc length covering 20° of the cylinder circumference and an edge length along the spike axis of 1/13th of the spike length (leading to 0.1 m edges for a spike length of 1.3 m).

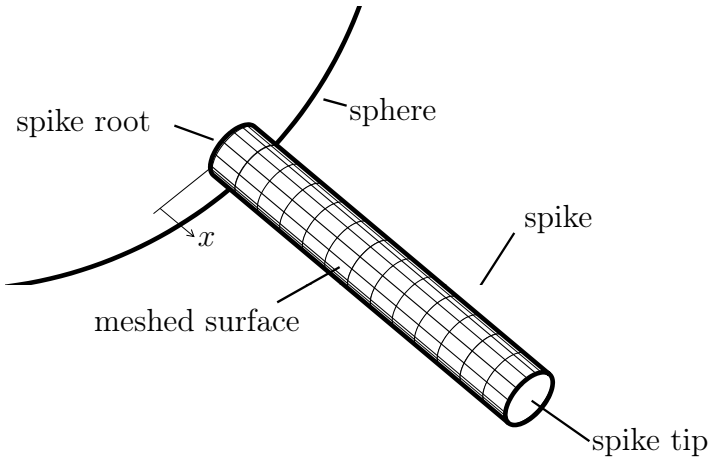

Figure 2.5: Terminology describing a spike, with x indicating the origin of the spike length

2.2.5 Results

Due to the geometry of the receiver a large number of rays is absorbed or reflected from neighboring spikes, missing the spike of interest. As a consequence, a total of 500×10^6 rays are used to generate repeatable flux maps.

With spikes of equal length, the spike tips are approximating surface elements of a virtual outer sphere enclosing the SCRAP receiver. The flux on the spike tips does consequently provide the characteristic value of operating receiver flux (flux on receiver aperture in $\mathrm{MW_{opt}/m^2}$).

The root flux value indicates the amount of energy missing the spikes and impinging on the sphere surface. Due to the symmetric configuration of the ray-tracing setup, near identical flux occurs circumferentially around a spike,

Stellenbosch University https://scholar.sun.ac.za

resulting in flux variation remaining largely a function of the axial position on the spike. On that account, the flux along the spike length is discussed.

The results of the ray-tracing analysis are normalized as a ratio of flux on the cylindrical spike surface over flux on the spike tip (approximately $300\,\mathrm{kW/m^2}$). Figure 2.6 shows the flux along the length of a spike as percentage of the flux measured at the spike tip for heliostats of the dimensions $1\,\mathrm{m} \times 1\,\mathrm{m}$, $2\,\mathrm{m} \times 2\,\mathrm{m}$ and $3\,\mathrm{m} \times 3\,\mathrm{m}$. For each case the heliostat field density is kept at 50 %[3] (mirror surface to attributed area per heliostat). Within 1.5 %, the three cases show the same total energy absorbed along the spike surface.

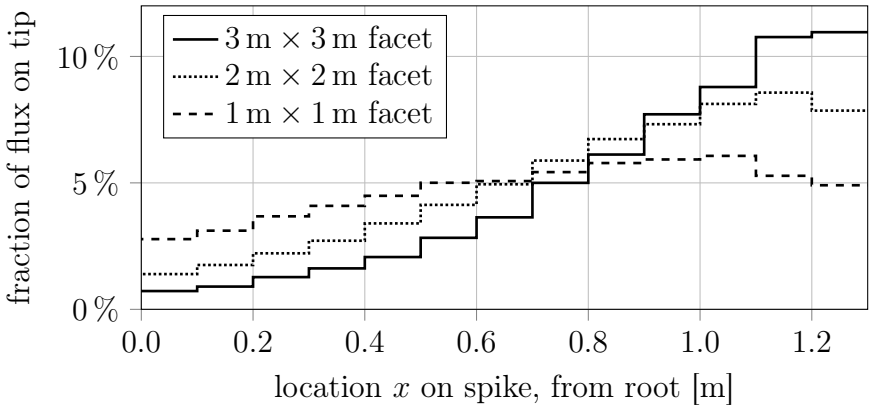

Figure 2.6: Flux along a spike for identical heliostat field density of 50 %.

It is notable that the sensitivity of the flux impinging along the spike surface from the tip down to the root is influenced by the heliostat size. Smaller heliostats achieve a higher penetration into the depth of the receiver, while larger heliostats lead to flux increasing towards the tip. This effect is expected to increase with further increase in heliostat size.

The simulated heliostats feature flat, single-facet mirrors. Canted mirrors or multi-faceted (and possibly canted) heliostats are expected to contribute further to depth penetration of flux. This finding suggests that the heliostat design has significant influence on the flux distribution.

With the observed behavior it is possible to investigate the heat transfer characteristics of a spike with reasonable understanding of concentrated solar flux required to be absorbed. With the heat transfer analysis providing understanding of desired flux along a spike a heliostat type, heliostat field layout and aiming strategy could eventually be selected accordingly, should it proof advantageous.

The flux curve for the $1\,\mathrm{m} \times 1\,\mathrm{m}$ heliostat, shown in Figure 2.6, shows a mean flux of 4.73 % of the flux on aperture, experienced on the spike tip.

[3]Heliostat field density is the ratio of cumulative heliostat facet aperture to total solar field size

Stellenbosch University https://scholar.sun.ac.za

2.3 Modeling of air flow and heat transfer

A model is developed to simulate the pressure drop and heat transfer of a single spike with straight internal fins. For this analysis it is assumed that heating from as well as heat loss to outside is uniform circumferentially and only subject to change in axial direction. This permits to assume symmetry and model the air flow and heat transfer in a slice, spanning one rectangular duct. An overview of occuring heat transfer mechanisms within a spike is shown in Figure 2.7.

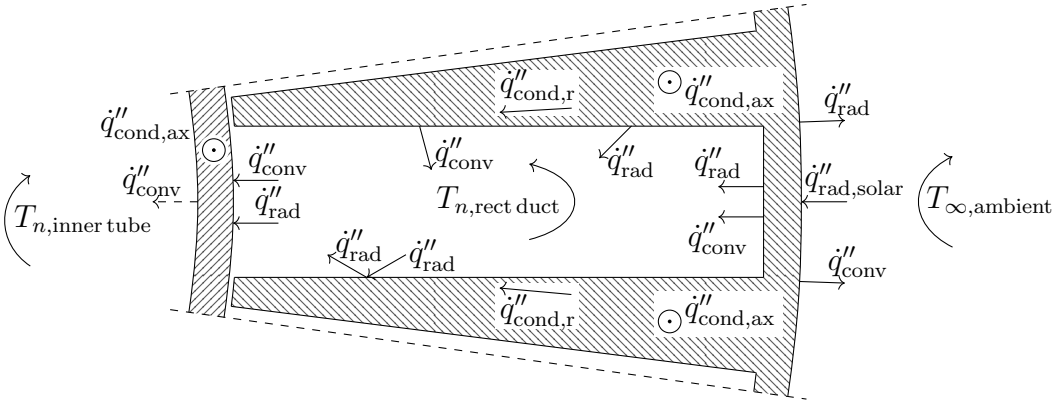

Figure 2.7: Visualization of heat transfer mechanisms within a rectangular duct's segment of a spike

2.3.1 Scope and setup of model

The scope of the simulation model is to predict the thermal characteristics of the spike, that is, the transfer from concentrated solar radiation into the pressurized air stream. Equally, the pressure drop of the air flow, as it passes through the spike is of interest. The thermal model includes thermal interaction with ambient to permit prediction of solar-thermal performance for steady state design point conditions.

The topography of the model is illustrated in Figure 2.8. The model is distinguished into three zones of which zone I is the inner tube as it passes from the inner chamber through the outer chamber. Zone II represents the spike, excluding tip (zone III), including thermal interaction between air flow in the rectangular ducts and the inner tube.

A flow chart depicting the model setup is shown in Figure 2.9. Here, the item 'auxiliary functions' contains functions to compute material properties and fluid ratios (e.g. Reynolds number). The conservation functions (mass conservation, momentum conservation and energy conservation) are contained

Stellenbosch University https://scholar.sun.ac.za

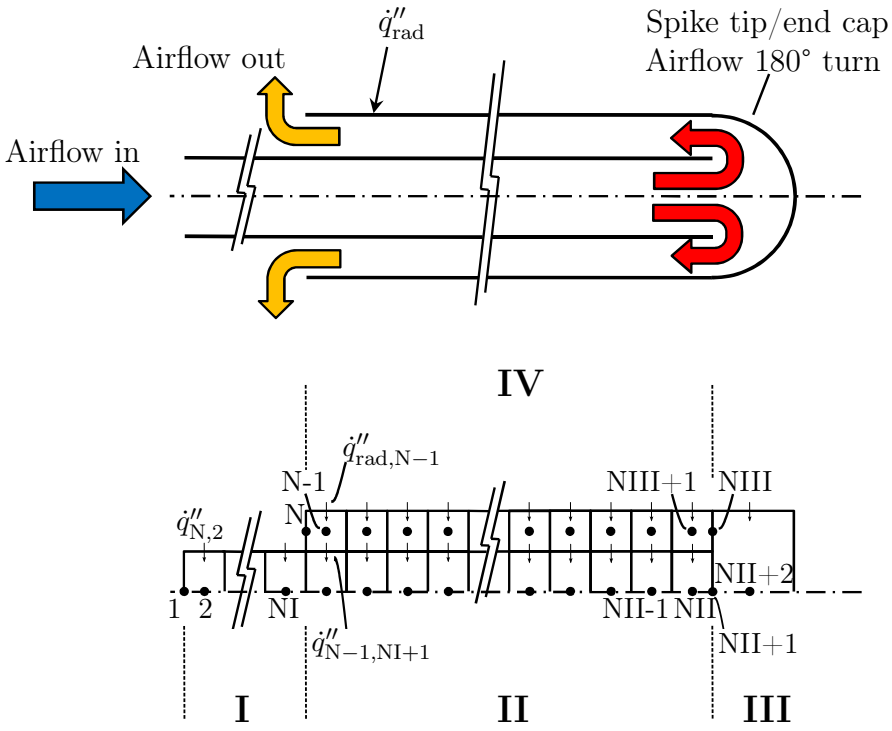

Figure 2.8: Topography of the spike simulation model. Zone I is the inner tube passing through the outer chamber (not shown), zone II is the inner tube within the internally finned outer tube (IV) and zone III is the spike tip.

in sub-programs for circular duct, spike tip and the internally finned outer tube. Following each global iteration loop, the temperature dependent properties are updated.

Additional detail to the right hand side of Figure 2.9 is illustrated in Figure C.1 in Appendix C. The model is adjusted to internally run increased iterations of sub-programs as observed to increase convergence speed. Relaxation factors are included in the model to aid stability. The computer model is programed in SciLab 5.4.1.

2.3.2 Modeling of air flow in inner tube

To compute the velocity and pressure drop of air in the circular tube the principles of momentum and mass conservation were employed. The resulting model follows iteratively the SIMPLE algorithm. For a fully developed, one-dimensional steady flow of constant density the momentum equation is:

$$\rho u \frac{\partial u}{\partial x} = -\frac{\mathrm{d}p}{\mathrm{d}x} + \frac{1}{r}\frac{\partial}{\partial r}\left(r\mu\frac{\partial u}{\partial r}\right) \tag{2.4}$$

To solve the momentum equation for a discretized pipe section, equation (2.4) is integrated over the volume of a control volume. For the one-dimensional

Stellenbosch University https://scholar.sun.ac.za

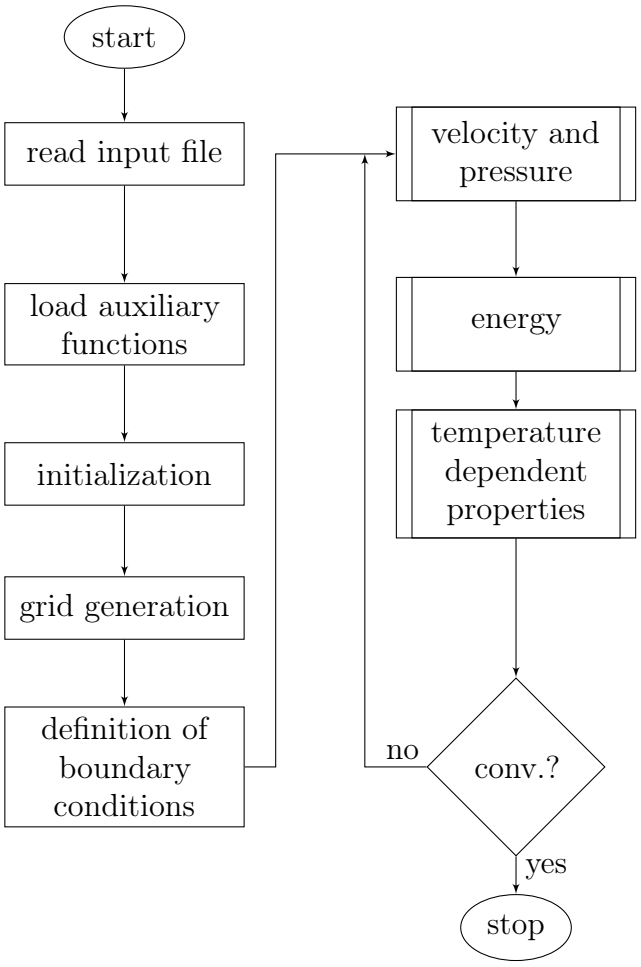

Figure 2.9: Flow chart of the one dimensional CFD code

problem only the gradient over r is considered as no mass transfer over the wall occurs. Applying the Gauss-theorem to equation (2.4) allows to instead of solving for the momentum integral

$$\int_V \rho u \frac{\partial u}{\partial x} \mathrm{d}V = \int_V -\frac{\mathrm{d}p}{\mathrm{d}x} \mathrm{d}V + \int_V \frac{1}{r} \frac{\partial}{\partial r} \left(r\mu \frac{\partial u}{\partial r} \right) \mathrm{d}V, \tag{2.5}$$

solving for the simpler surface integral:

$$\int_S (\rho u u) \mathrm{d}S = -\frac{\mathrm{d}p}{\mathrm{d}x} V + \int_S (\mu \frac{\partial u}{\partial r}) \mathrm{d}S, \tag{2.6}$$

The last integral is over the wall surface shear stress which is defined as

$$\tau_\mathrm{s} = \mu \left(\frac{\partial u}{\partial r} \right)_{r=r_\mathrm{s}} \tag{2.7}$$

Stellenbosch University https://scholar.sun.ac.za

for a circular pipe, which for turbulent flow can also be expressed as

$$u_\tau = \sqrt{\frac{\tau_\mathrm{s}}{\rho}} = -U\sqrt{\frac{f_\mathrm{D}}{8}}, \tag{2.8}$$

which can be rearranged as

$$\tau_\mathrm{s} = \mu \left(\frac{\partial u}{\partial r}\right)_{r=r_\mathrm{s}} = -U^2 \rho \frac{f_\mathrm{D}}{8} \tag{2.9}$$

by inserting the analytically known velocity profile for fully developed turbulent flow in a pipe into equation (2.7), with U being the mean flow velocity.

Applying upwind discretization, equation (2.6) at node i can be written as

$$(\rho UUA)_i - (\rho UUA)_{i-1} = -\left(\frac{p_i - p_{i-1}}{x_i - x_{i-1}}\right) V_i - U_i^2 \rho \frac{f_\mathrm{D}}{8} A_{i,\mathrm{s}} \tag{2.10}$$

for the one-dimensional solver. Solving equation (2.10) for the velocity gives

$$U_i = \frac{\left(\frac{p_{i-1}-p_i}{x_i - x_{i-1}}\right) V_i + \rho_{i-1} U_{i-1} U_{i-1} A_{i-1}}{\rho_i U_{i,\mathrm{old}} A_i + U_{i,\mathrm{old}} \rho \frac{f_\mathrm{D}}{8} A_{i,\mathrm{s}}}, \tag{2.11}$$

where the velocity of the previous iteration step $U_{i,\mathrm{old}}$ is used to enhance solver stability. For the friction factor a suitable equation, such as the Blasius' (1912) curve fit for the friction factor f_D can be used:

$$f_\mathrm{D} = 0.3164\, Re^{-0.25}, \tag{2.12}$$

which is valid for $3000 \leq Re \leq 10^5$ (White, 1991). With lower Reynolds numbers towards $Re = 2300$ equation (2.12) overestimates f_D as it fails to consider the transition zone. One could substitute equations (2.9) and (2.12) in the discretized governing equation (2.6), this, however, would limit flexibility towards using different equations to compute f_D.

To calculate the pressure drop in the circular tube, the mass conservation equation is applied. For steady, developed flow, the differential equation is

$$\frac{\partial}{\partial x}(\rho u) = 0. \tag{2.13}$$

As previously, integrating equation (2.13) over the control volume volume for the one-dimensional problem, applying upwind discretization, leads to

$$\rho_i U_i A_i - \rho_{i-1} U_{i-1} A_{i-1} = 0. \tag{2.14}$$

During the iteration process mass conservation is not necessarily satisfied, resulting in equation (2.14) being nonzero. For that case,

$$\rho_i U_i A_i - \rho_{i-1} U_{i-1} A_{i-1} = \rho_i U_i' A_i \tag{2.15}$$

Stellenbosch University https://scholar.sun.ac.za

provides a residual velocity U'. In this case, $\rho_i U_i A_i - \rho_{i-1} U_{i-1} A_{i-1}$ acts as mass source, which, to satisfy the condition of conservation of mass, has to reach zero, eventually. The residual velocity U' can be expressed as the result of a pressure drop $(\mathrm{d}p/\mathrm{d}x)'$ over the control volume (that equally drops to zero when the actual pressure drop is adjusted correctly).

Using the momentum equation (2.11), one can compute U' as

$$U_i' = \frac{\left(\frac{\mathrm{d}p}{\mathrm{d}x}\right)_i' V_i}{\rho_i U_{i,\mathrm{old}} A_i + U_{i,\mathrm{old}}^2 \rho \frac{f_\mathrm{D}}{8} A_{i,\mathrm{s}}}. \tag{2.16}$$

Combining equations (2.15) and (2.16) and solving for $(\mathrm{d}p/\mathrm{d}x)'$ gives

$$\left(\frac{\mathrm{d}p}{\mathrm{d}x}\right)_i' = \frac{\left(\rho_i U_i A_i - \rho_{i-1} U_{i-1} A_{i-1}\right)\left(\rho_i U_i A_i + U_{i,\mathrm{old}}^2 \rho \frac{f_\mathrm{D}}{8} A_{i,\mathrm{s}}\right)}{\rho_i U_i V_i}. \tag{2.17}$$

Consequently, $(\mathrm{d}p/\mathrm{d}x)'$ multiplied by the control volume length δ_x provides the pressure drop over a control volume. The pressure can thus be adjusted, using a relaxation factor α_p as:

$$p_i = p_{i,\mathrm{old}} - \alpha_p \left(\frac{\mathrm{d}p}{\mathrm{d}x}\right)_i' \delta_{x,i}. \tag{2.18}$$

When the simulation has converged, p_i has approached $p_{i,\mathrm{old}}$ and $\left(\frac{\mathrm{d}p}{\mathrm{d}x}\right)_i'$ will be zero.

2.3.3 Modeling of air flow in rectangular ducts and correction for secondary flows

The computation of the air velocity and pressure drop in the rectangular ducts follows the same principle as outlined above in subsection 2.3.2. Re, however, is calculated from the hydraulic diameter d_h.

The occurrence of secondary flows within a rectangular duct in the turbulent flow regime requires amendment of the pressure drop computation. Secondary velocity distribution may lead to an underestimation of friction factors by up to 10 % (Kröger, 2004). Jones (1976) introduced a modified Reynolds number Re^* for the calculation of the friction factor for turbulent flow in smooth rectangular ducts. The modified Reynolds number Re^* is defined as

$$Re^* = C\, Re \tag{2.19}$$

with

$$C = \frac{2}{3}\left(1 + \frac{w}{h}\right)^2 \left[1 - \frac{192w}{\pi^5 h} \sum_{n=0}^{\infty} \frac{1}{(2n+1)^5} \tanh\left(\frac{(2n+1)\pi h}{2w}\right)\right], \tag{2.20}$$

where the modifying value of C is a geometry function of the duct's aspect ratio w/h. Plotting C out of Equation (2.19) over the duct's aspect ratio from zero (parallel plates) to one (quadratic duct shape) illustrates the modification range proposed by the work of Jones, as shown in Figure 2.10.

Stellenbosch University https://scholar.sun.ac.za

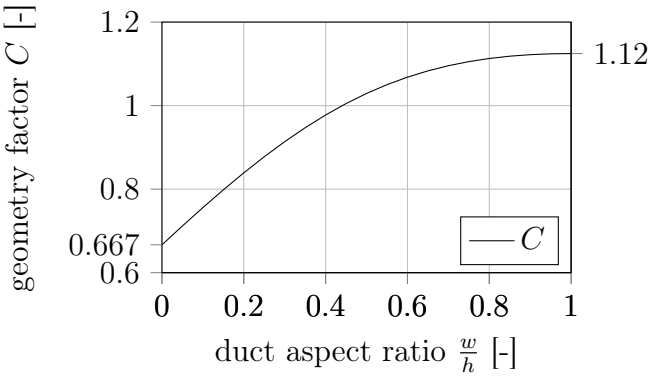

Figure 2.10: Geometry factor C over a rectangular duct's aspect ratio w/h

2.3.4 Modeling of heat transfer in inner tube

The convective heat transfer into the air stream is modeled by satisfying the principle of energy conservation. Here, axial conduction within the air stream is neglected as it is of noteworthy effect only for small Péclet numbers Pe (Michelsen and Villadsen, 1974). The principle of energy conservation dictates that

$$\sum \dot{Q} = 0. \tag{2.21}$$

The thermal energy $\Delta\dot{Q}$ introduced into the air stream as it passes through a control volume can be computed from the change in specific enthalpy from inlet to outlet as

$$\Delta\dot{Q} = \dot{m}\Delta h \tag{2.22}$$

with the air flow rate $\dot{m}$ being constant. From

$$c_\mathrm{p} = \left(\frac{\partial h}{\partial T}\right)_p, \tag{2.23}$$

from which, after rearranging, the change in specific enthalpy can approximately expressed as

$$\Delta h = c_\mathrm{p}\Delta T. \tag{2.24}$$

Thus, $\Delta\dot{Q}$ can be calculated as

$$\Delta\dot{Q} = \dot{m}c_\mathrm{p}\Delta T. \tag{2.25}$$

The change in thermal energy, $\Delta\dot{Q}$, over a control volume can be calculated, using equation (2.25) as:

$$\Delta\dot{Q} = \dot{m}c_\mathrm{p}(T_{\mathrm{m},i} - T_{\mathrm{m},i-1}), \tag{2.26}$$

where $T_{\mathrm{m},i-1}$ and $T_{\mathrm{m},i}$ are the control volume inlet and outlet mean temperature, respectively. The specific heat, c_p, is calculated as the mean value as $c_\mathrm{p} = (c_{\mathrm{p},i-1} + c_{\mathrm{p},i})/2$.

Stellenbosch University https://scholar.sun.ac.za

For the purpose of this model equation (2.26) is split into representing an advective thermal energy content of air entering the control volume and an advective thermal energy content of air exiting the control volume. The energy contained in the flow upstream of a node is

$$\dot{Q}_{i-1,\mathrm{adv}} = (\pi r_\mathrm{s}^2 U \rho)_{i-1}\, c_\mathrm{p}\, T_{\mathrm{m},i-1}. \tag{2.27}$$

The convective energy flow into the control volume by heating from the channel wall

$$\dot{Q}_{i,\mathrm{conv}} = (2\pi r_\mathrm{s} \delta_x)_i\, \dot{q}''_{\mathrm{s},i} \tag{2.28}$$

and the resulting downstream energy flow exiting the control volume is

$$\dot{Q}_{i,\mathrm{adv}} = (\pi r_\mathrm{s}^2 U \rho)_i\, c_\mathrm{p} \left(T_{\mathrm{m},i} + \left(\frac{\mathrm{d}T_{\mathrm{m},i}}{\mathrm{d}x} \right)'_i \delta_{x,i} \right). \tag{2.29}$$

Applying conservation of energy principle $\dot{Q}_{i-1,\mathrm{conv}} + \dot{Q}_{i,\mathrm{heating}} = \dot{Q}_{i,\mathrm{conv}}$

$$\left(\frac{\mathrm{d}T_{\mathrm{m},i}}{\mathrm{d}x} \right)'_i \delta_{x,i} = \frac{(r_\mathrm{s} U \rho)_{i-1}\, c_\mathrm{p}\, T_{\mathrm{m},i-1} + 2\delta_{x,i} \dot{q}''_{\mathrm{s},i} - (r_\mathrm{s} U \rho)_i\, c_\mathrm{p} T_{\mathrm{m},i}}{r_\mathrm{s} U_i \rho_i c_{\mathrm{p},i}}. \tag{2.30}$$

As with the pressure drop computation, the code is converged when $(\mathrm{d}T/\mathrm{d}x)'$ approaches zero. The updated temperature at a node is calculated with a relaxation factor:

$$T_{\mathrm{m},i} = T_{\mathrm{m},i,\mathrm{old}} + \alpha_T \left(\frac{\mathrm{d}T_{\mathrm{m},i}}{\mathrm{d}x} \right)'_i \delta_{x,i}. \tag{2.31}$$

Forward discretization is applied for the heat transfer computation. In equation (2.30) $\dot{q}''_{\mathrm{s},i}$ is the heat flux from the tube wall into the flow. The selection of heat transfer coefficients is discussed in subsection 2.5.

2.3.5 Modeling of convective heat transfer in rectangular ducts

The energy balance for computing the convective heat transfer within the rectangular ducts is solved in the same way as outlined for the inner circular tube. Here, $\dot{Q}_{i,\mathrm{conv}}$ is defined as the sum of all convective heat transfer from the fin surface (or its increments), the outer tube's inner wall w as well as the cooling by the inner tube's wall.

2.3.6 Trapezoidal fins

With ducts of rectangular shape the cross section of the fins results in a trapezoidal shape. The transverse conductive heat transfer through a fin as well as the convective heat transfer from a fin to the air stream can be compared

Stellenbosch University https://scholar.sun.ac.za

in the Biot number. The transversal Biot number on the fin root is calculated as

$$Bi = \frac{w_{\text{root}}/2\,h}{k}, \tag{2.32}$$

where w_{root} is the width of the fin root, h the convective heat transfer coefficient from the fin to the air stream and k the fin material's thermal conductivity. Bi is therefore dependent on the internally finned tube geometry, the assumptions leading to the heat transfer coefficient and the fin material properties. The Biot number represents a ratio of the internal heat transfer resistance to the external heat transfer resistance. A low Biot number ($Bi \leq 0.1$) permits for the simplification of ignoring transverse temperature gradients, hence the temperature gradient only being considered radially (Kröger, 2004).

Employing the reference geometry, the Biot number can be estimated using equation (2.32). Assuming a thermal conductivity k of the metal of about 20 W/m K, a duct width w of 3 mm and a fin root width w_{root} of 6.01 mm provides that for Reynolds numbers exceeding 23 000 the Biot number is above 0.1. The Reynolds numbers expected for the SCRAP receiver are significantly lower (see chapter 5) and $Bi \leq 0.1$ can be assumed.

Consequently, the trapezoidal fin is meshed in radial direction only, ignoring a transversal temperature gradient. A subroutine computes the temperatures for each control volume (1 to m) of the fin as shown in Figure 2.11. Each fin control volume 1 to m thermally interacts with the air stream in node i through convection, using the same heat transfer coefficient, computed for duct flow in node i. A wall node 0 interacts with ambient conditions. The wall node's position is fixed, while the remaining nodes are distributed in uniform spacing along the fin, depending on the defined resolution.

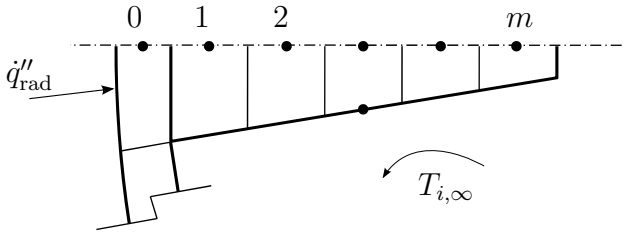

Figure 2.11: Exemplification of the topography of a trapezoidal fin

The thickness of the wall increment 0 is fixed at the wall thickness, resulting in $T_{\text{o}} = T_{\text{i}} = T_0$. With an assumed thermal conductivity of 20 W/m K the resulting temperature difference over a 2 mm wall would be 4 K (assuming a flux of 50 kW/m^2 is applied at thermal efficiency of 80 %). Thus, this simplification should lead to an under or over estimation, depending on which side of the wall considered, of about 2 K which is considered acceptable.

Stellenbosch University https://scholar.sun.ac.za

Heat transfer model

The applied meshing of the trapezoidal fin is illustrated in Figure 2.11. A node 0 provides the wall temperature. The following number of nodes 1 to m through the fin are solved using an energy balance, where the sum of all thermal conduction in axial and radial direction as well as the thermal convection to the air stream are zero:

$$\sum \dot{Q}_{\text{cond,radial}} + \sum \dot{Q}_{\text{cond,axial}} + \sum \dot{Q}_{\text{conv}} = 0 \tag{2.33}$$

The convective heat transfer from the fin elements to the free stream is simplified by using a constant Nu throughout the fin length. It is noted that a constant heat transfer coefficient over the fin length can lead to notable errors (Huang and Shah, 1992).

Linking of fin model and outer wall

The first node 1 of the trapezoidal fin ($m = 1$)is linked to a wall node 0. The outer tube wall is represented by a single node (thus no temperature gradient radially over the wall thickness). An energy balance for a single duct can thus be written as:

$$\dot{Q}_{\text{rad},solar} + \dot{Q}_{\text{rad},\infty} + \sum \dot{Q}_{\text{conv},\infty} + \dot{Q}_{\text{conv},i} + \sum \dot{Q}_{\text{cond}} + \dot{Q}_{\text{rad,i},i} = 0, \tag{2.34}$$

where $\dot{Q}_{\text{rad,solar}}$ is the solar radiation heating of the outside surface over the duct and the fin root and $\dot{Q}_{\text{conv},i}$ the convective heat transfer from the tube wall into the duct and $\sum \dot{Q}_{\text{cond}}$ the sum of all axial and radial heat conduction into the fin. $\dot{Q}_{\text{rad,i},i}$ is the thermal radiation from the inner wall towards the colder inner tube (introduced in subsection 2.6).

A possible temperature depression on the fin root is unaccounted for as node 0 spans over the inner duct (as for symmetry half a duct is modeled, node 0 spans over 50 % of the duct). As a consequence, the wall temperature over the fin root is slightly overestimated while the wall temperature over the duct w is slightly underestimated. As the duct width is of similar dimension to the outer wall thickness, the transversal heat resistance is equally ignored. As a result, an analytical energy balance can be established to compute the wall temperature for each iteration step.

2.3.7 Axial heat conduction

The trapezoidal fin as well as the outer spike wall can experience notable temperature gradients axially. This necessitates the implementation of axial conduction into the model. Due to symmetry, transversal conduction is zero. The axial conduction considers the temperature of the neighboring wall node upstream $(n-1)$ as well as the neighboring node downstream $(n+1)$.

Stellenbosch University https://scholar.sun.ac.za

2.3.8 Spike tip — Jet impingement cooling

The cooling of the tip's inner metal surface is achieved by an impinging air jet, intended to provide relatively high local heat transfer capabilities. Impingement jet cooling, using pressurized air jets are also researched for utilization in other fields of CSP, such as cavity receivers for parabolic dish applications (Wang *et al.*, 2015).

Here, in the heat transfer simulation model developed, the spike tip is modeled as a single node, covering pressure drop and heat transfer for the entire tip in one control volume. The heat transfer occurring due to impinging air flow on the inner wall of the spike tip is simulated using the commercial CFD software ANSYS® FLUENT (Release 15.0). To provide the ability to solve the spike tip in a single node, an averaged heat transfer coefficient, h_{tip}, is required. While it is noted that CFD models may deviate notably from measured results (Zuckerman and Lior, 2006), the purpose of this analysis is to obtain a reasonable heat transfer coefficient and understand the implication on required nozzle[4] dimensions in order to model the interaction between h_{tip} and the accompanying pressure drop.

The aim of the heat transfer analysis of the spike tip is to extract an average Nusselt number that can be used for the spike simulation model, providing the ability to serve as proof of concept. A precise representation of local heat transfer within the spike tip, and consequently, a locally precise CFD model are not aspired to as part of this study. This is due to the significant potential geometrical improvements within the spike tip region. Some examples are the nozzle shape, axial nozzle position, shape of inlets into rectangular ducts/fin fronts, potential protruding of these into the tip region. The nature of analyzing such geometrical variations and their effect onto local heat transfer capabilities as well as the pressure drop demand an individual in depth research undertaking.

To obtain an averaged heat transfer coefficient, h_{tip}, a CFD model is developed and varying nozzle sizes are investigated with the Nusselt number being compared. To identify a suitable turbulence model in FLUENT, a reference case from literature was reproduced, where a jet is directed onto a flat plate. Satisfactory agreement was found when the k-ε model was used (see Appendix G). To predict impingement cooling on a spike tip, analysis on an annular surface is conducted, omitting the fins in the outer tube section, permitting utilization of a two-dimensional mesh. Figure 2.12 shows a sketch of the two-dimensional axis-symmetric geometry used to analyze the spike tip in CFD. To vary the nozzle diameter r_{nozzle} was changed, while leaving r_{i} constant.

The mesh was refined as part of a sensitivity analysis until the results appeared to have stabilized (see Appendix H for grid independence procedure).

[4]A nozzle may be required at the end of the inner tube to accelerate the air stream locally for improved cooling

Stellenbosch University https://scholar.sun.ac.za

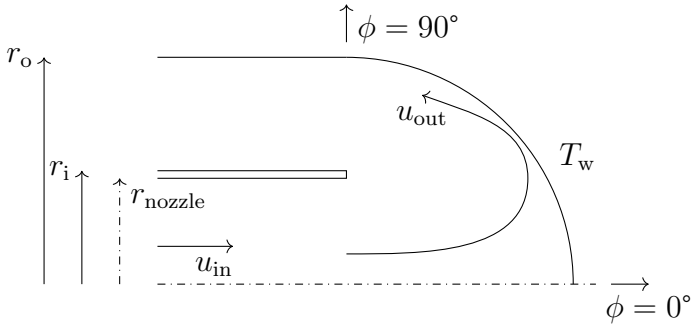

Figure 2.12: Sketch of the axis symmetric two-dimensional geometry employed as reference case for impingement jet cooling CFD model

Figure 2.13 shows the local Nusselt number, Nu_ϕ, over a section of the tip surface over a range of Reynolds numbers. The mass flow rate for each case is identical. The differing nozzle sizes are simulated by using according inner tube diameters in order to generate reproducible fully developed flow profiles.

The remaining model dimensions are identical with the reference case dimensions such as an outer tube of 66 mm inner diameter and an inner tube of 30 mm outer diameter. The inner diameter of the inner tube is varied in order to represent the nozzle diameter. User defined functions were used to provide a fully developed flow profile. Figure 2.13 illustrates the local Nusselt numbers over the angle ϕ for nozzle sizes from 5 mm to 26 mm. Here, the Nusselt number is calculated as $Nu = (hd_{nozzle})/k$, where h is the local heat transfer coefficient and k the thermal conductivity of air at nozzle exit.

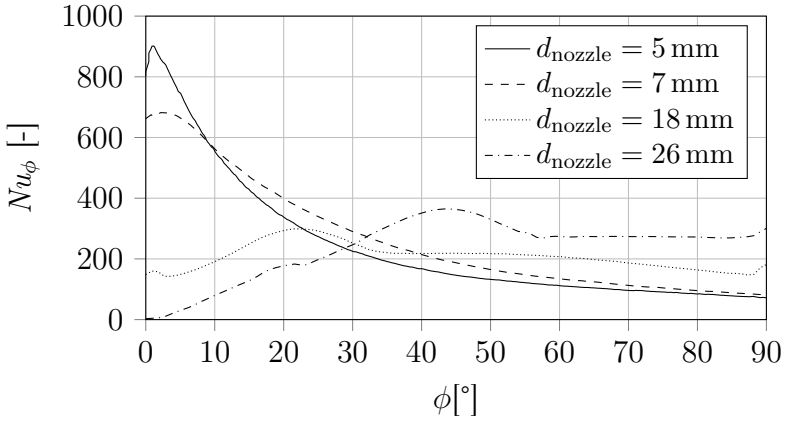

Figure 2.13: Local Nusselt number Nu_ϕ for different nozzle diameter d_{nozzle} from 5 mm to 26 mm over spike tip position for constant mass flow rate $\dot{m} = 0.026$ kg/s. Angle $\phi = 0°$ is the center point coaxial with the spike and $\phi = 90°$ the point where the tip connects to the outer tube.

For a large nozzle of 26 mm, the local Nusselt number $Nu_{\phi=0}$ reaches a

Stellenbosch University https://scholar.sun.ac.za

minimum at the center point ($\phi = 0°$) due to the local stagnation area being too large. As the nozzle diameter decreases the peak in Nu_ϕ shifts towards $\phi = 0°$, which is desired due to peak flux at this point. The mean heat transfer coefficient h_{tip} is calculated from the area averaged Nusselt number $\overline{Nu}$ as $h_{\text{tip}} = \overline{Nu}\, k_{\text{air}}/d_{\text{nozzle}}$. Figure 2.14 shows the averaged heat transfer coefficient as a function of the nozzle diameter.

A curve fit over the h_{tip} data points allows to reproduce reasonable heat transfer coefficient accuracy for other nozzle diamaters:

$$\begin{aligned} h_{\text{tip}} =& (-7.067 \times 10^7 d_{\text{nozzle}}^3 + 7.018 \times 10^6 d_{\text{nozzle}}^2 - \\ & 2.095 \times 10^5 d_{\text{nozzle}} + 2.5233 \times 10^3)\,\text{W}/(\text{m}^2\,\text{K}) \end{aligned} \tag{2.35}$$

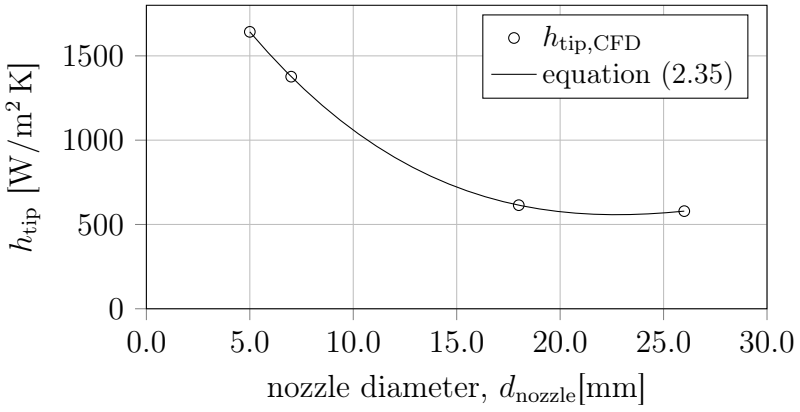

Figure 2.14: Heat transfer coefficient h_{tip} for different nozzle diameter d_{nozzle} from 5 mm to 26 mm over spike tip position for constant mass flow rate $\dot{m} = 0.026\,\text{kg/s}$.

Between the nozzle diameters of 26 mm and 18 mm the improvement in h_{tip} is marginal. In between these data points the stagnation zone at the center of the impingement disappears and the heat transfer coefficient sees increased rise at the center point. Further reduction in d_{nozzle} results in increasing h_{tip}.

2.3.9 Spike tip — pressure drop

The pressure drop model consists of four equations. The generic pressure drop equation

$$\Delta p = \xi \frac{\rho u^2}{2} \tag{2.36}$$

is used to compute the pressure drop for a nozzle, Δp_{nozzle}, the pressure drop representing the 180° turn in flow direction, Δp_{tip}, as well as the pressure drop for the flow entering the rectangular ducts, Δp_{duct}. Bernoulli's equation is applied to compute the pressure drop/recovery with the change in flow

Stellenbosch University https://scholar.sun.ac.za

cross-sectional section between the inner tube and the rectangular ducts, Δp_A. Table 2.4 provides an overview over the variables used for computation of the pressure drops.

Table 2.4: Friction coefficients ξ applied to computation of pressure drop at spike tip

pressure drop	friction coef.	comment	reference
Δp_{nozzle}	$\xi_{nozzle} = 0.04$	$u = u_{nozzle}$	(VDI, 2010)
Δp_{tip}	$\xi_{tip} = 0.1$	$u = u_{nozzle}$	(Idelchik, 1986)
Δp_{duct}	$\xi_{duct} = 0.3$	$u = u_{duct}$	(VDI, 2010)
ΔA_{duct}	Bernoulli	[-]	

The friction coefficients ξ_{nozzle} as well as ξ_{duct} duct are conservative values from literature. Improvements in inlet shape can reduce ξ_{duct} by more than an order of magnitude.

The friction coefficient for the spike tip, ξ_{tip}, is extracted from Idelchik (1986). The spike tip is envisaged with a nozzle to accelerate air flow and achieve a sufficient jet impingement cooling effect. The analysis of the heat transfer coefficient shows that a nozzle permits increasing the heat transfer coefficient notably.

Idelchik (1986) provides empirical values for ξ_{tip} for nozzle distance of $H/d_{nozzle} \leq 2$. Idelchik's data suggest that rounded edges well as increased distance $H/d_{nozzle} \leq 2$ (within the range of 0.1 to 2.0) assist in reducing ξ_{tip} to values as low as $\xi_{tip} = 0.1$. Idelchik provides the data for various area ratios of the downstream outer annular cross sectional area A_o to the nozzle cross sectional area A_{nozzle}, where increased ratios A_o/A_{nozzle} show to reduce ξ_{tip} towards larger H/d_{nozzle}. The largest A_o/A_{nozzle} provided is of 2.1, whereas A_o/A_{nozzle} for the investigated nozzle diameters is between 5 and 140. A friction coefficient of $\xi_{tip} = 0.1$ is therefore assumed.

The experimental setup confirms this assumption of relatively low ξ_{tip} (see section 4.4.1), where, for the experimental geometry, with $H/d_{nozzle} = 1.27$, ξ_{tip} is expected anywhere between 0.15 to 1.10, according to Idelchik's data, depending on which r/d_{nozzle} being selected (r being the radius on the nozzle's outlet edge). With the experiment not being equipped with a nozzle, the ratio $A_o/A_{nozzle} = 5.5$, as $d_{nozzle} = 25\,\text{mm}$. The nozzle's edge is on the outside equipped with a $1\,\text{mm} \times 1\,\text{mm}$ chamfer, which, if translated into r leads to the ratio $r/d_{nozzle} = 0.04$, suggesting ξ_{tip} in the range of 0.72 to 1.1.

The CFD model employed to identify mean Nusselt numbers as discussed previously in chapter 2.3.8 further suggests the assumption for ξ drawn from Idelchik is suitable. Simulation results suggest a ξ of about 0.2 being adequate. The model, however, features sharp edges instead of rounded edges as applied for the experimental setup as well as assumed for an actual geometry.

Stellenbosch University https://scholar.sun.ac.za

Zuckerman and Lior (2006) shows that Nusselt numbers of impinging jets are mainly dependent on the Reynolds number but in the range of $2 \leq H/d_{\text{nozzle}} \leq 10$ show reasonable stability towards the change in position. This permits, accepting an underestimation of the heat transfer capabilities, to assume nozzle position to be at $H/d_{\text{nozzle}} = 2$.

2.4 Coupling of heat transfer between rectangular ducts and circular inner tube

Due to thin wall thickness, radial heat conduction within the inner tube wall is neglected, resulting in $T_{\text{s,i}} = T_{\text{s,o}}$.

The heat transfer problem is simplified with the assumption that on the outer wall of the tube heat transfer only occurs from the wall to air stream in the rectangular duct and no heat transfer occurs between the fin tips and the walls. Figure 2.15 illustrated the heat convecting surfaces.

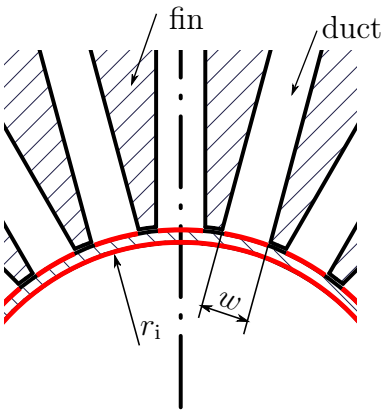

Figure 2.15: Illustration of the heat transfer assumption that the rectangular outer ducts convect heat inwards via the duct width w (approximately an element of the inner tube's outer surface). The inner tube convects heat over the entire surface $2\pi r_{\text{i}}$.

The axial temperature gradients within the pipe walls can be significant and thermal conductivity in the axial direction is considered. The inner tube thermally connects the two cross-flowing air streams via convective heat transfer, being influenced by axial conduction along the inner tube.

2.5 Selection of Nusselt number

Nusselt number equations for circular tubes are in good agreement with measured results for rectangular ducts if the equivalent hydraulic diameter d_{h} is

Stellenbosch University https://scholar.sun.ac.za

applied. The selection of equations to calculate the Nusselt numbers in the simulation model are outlined in this chapter.

2.5.1 Selection of Nusselt number for the air flow in the inner tube

A compact equation to compute the Nusselt number for gases of $0.5 \leq Pr \leq 1.0$ is

$$Nu_{\mathrm{H}} = 0.022 Pr^{0.5} Re^{0.8} \tag{2.37}$$

for constant heat rate (Kays *et al.*, 2005). For the case of the boundary condition of constant surface temperature, Kays *et al.* (2005) recommend

$$Nu_{\mathrm{T}} = 0.021 Pr^{0.5} Re^{0.8}. \tag{2.38}$$

Equations (2.37) and (2.38) are of similar nature and allow direct extraction of an average equation as an initial assumption for the simulation model (a spike will not likely be experiencing either of the ideal boundary conditions but experience some heat transfer condition in between):

$$Nu = 0.0215 Pr^{0.5} Re^{0.8}. \tag{2.39}$$

Equation (2.39) is used to calculate the Nusselt number for the air stream within the inner tube.

2.5.2 Selection of Nusselt number for the air flow in the rectangular ducts

Different equations for the Nusselt number are required for the heating of air flow in the rectangular ducts. Due to the limited size of the experimental setup, an equation is required that permits calculation of local heat transfer coefficients. As shall be seen later, the reference design of a spike leads to Reynolds numbers in the low turbulent flow regime ($Re \leq 10\,000$), requiring a different, suitable Nusselt number.

For the experimental case, the modified Gnielinski equation was selected as it permits to include the region of thermal development of the flow by providing local Nusselt numbers, Nu_x, Gnielinski (2010):

$$Nu_x = \frac{(f_{\mathrm{D}}/8) Re\, Pr}{1 + 12.7\sqrt{f_{\mathrm{D}}/8}\,(Pr^{2/3} - 1)} \left[1 + \frac{1}{3}\left(\frac{d_{\mathrm{h}}}{x}\right)^{2/3}\right]. \tag{2.40}$$

The Gnielinski equation is valid for Re of $10^4 \leq Re \leq 10^6$ (Gnielinski, 2010). The ability to account for the developing thermal boundary layer is of interest for the spike tip region. The flow entering the rectangular ducts at the tip, where the flow direction is turned by 180°, is unlikely to be of uniform distribution.

Stellenbosch University https://scholar.sun.ac.za

However, comparing equation (2.40) with the conventional global Nusselt number equations (2.37 & 2.38) that do not at all consider the local variation as a result of developing thermal boundary layers, permits drawing conclusions on the significance of being able to predict the heat transfer accurately in these regions.

When simulating a spike under reference conditions, the Re within the rectangular ducts may drop to lower turbulent values or perhaps even a laminar flow regime. A variation of Gnielinski's equation is

$$Nu = \frac{(Re - 1000)Pr(\xi/8)}{1 + 12.7\sqrt{\xi/8}\,(Pr^{2/3} - 1)}, \tag{2.41}$$

which, while similar to equation (4.6), does not provide local heat transfer coefficients but is extended to Re of $2.3 \times 10^3 \leq Re \leq 10^6$ (Kays *et al.*, 2005). Should the air flow drop into the laminar regime, Nusselt numbers based on Shah and London (1978) are used. Here,

$$Nu = 1.508882\left(\frac{w}{h}\right)^3 - 4.122727\left(\frac{w}{h}\right)^2 + 5.182207\left(\frac{w}{h}\right) + 0.008172 \tag{2.42}$$

is used to compute the Nusselt number for one narrow side w of the duct transferring heat as a function of the duct geometry (heat transfer from the air flow in the outer duct towards the colder inner duct wall). For heating of the air flow over the remaining three sides (fin walls and outer w),

$$Nu = 9.29451\left(\frac{w}{h}\right)^4 - 25.2036\left(\frac{w}{h}\right)^3 + 27.1205\left(\frac{w}{h}\right)^2 - 15.8021\left(\frac{w}{h}\right) + 7.87845 \tag{2.43}$$

is used. Both equations, (2.42) and (2.43) are curve fits to the mean between equations provided for constant heat rate as well as constant surface temperature (see Appendix F).

2.6 Internal radiative heat transfer

Radiative heat transfer within the spike is implemented as significant temperature gradients across surfaces occur.

2.6.1 Radiative heat transfer within a rectangular duct

Radiative heat transfer occurs between the surfaces within a rectangular duct. While the inner circular tube is cooled by the cold air stream, the outer tube and fins are heated by the concentrated solar irradiation, leading to a notable temperature difference.

Radiative heat transfer between two surfaces can be expressed as

$$\dot{q}''_{\mathrm{rad},1\to n} = \sum_{n=1}^{N} \sigma F_{1\to n}\alpha_n\varepsilon_1(T^4_{\mathrm{s},1} - T^4_{\mathrm{s},n}), \tag{2.44}$$

Stellenbosch University https://scholar.sun.ac.za

where σ is the Stefan-Boltzmann constant, α_n the absorptivity of surface n and ϵ_1 the emissivity of surface 1. $F_{1\to n}$ expresses the view factor between the two surfaces 1 and n. A robust way to automate view factor computation for a continuous geometry such as the rectangular duct is the crossed-strings method which is described in Appendix E.

The material properties α and ε are temperature dependent. For availability of suitable data a curve fit for Inconel 718 is implemented into the model (see Appendix I)[5].

Within the rectangular ducts radiative heat transfer is implemented from the fin segments as well as the internally exposed segment of the outer wall towards the surface of the inner tube. This leads to the fin segments to directly thermally interact with the inner tube. With the rectangular duct being narrow, mostly the segments towards the fin tips show notable view factors towards the inner tube. Thermal radiation from fin to fin, both radially as well as axially, is not considered. Temperature gradients are small which is combined with view factors only being notable towards segments of similar temperature.

Not considered is also the axial radiative heat transfer from surfaces associated to node i to upstream or downstream surfaces associated e.g. to nodes $i+1$ or $i-1$ as the effect is limited with narrow ducts (due to low view factors and temperature differences).

2.6.2 Radiative heat transfer within the spike tip

Due to the high solar irradiation on the spike tip, a local material temperature peak can occur, when comparing to material temperatures near the spike tip. There, radiative heat transfer is included in the model to heat (a) walls inside the first node in the circular tube (node NII in Figure 2.8) as well as the rectangular duct (node NIII+1) and (b) heat the cross section of the fins and tube that are exposed towards the tip (cross sectional surface as visible in Figure 2.15) where the rectangular ducts and inner tube end.

2.6.3 Radiative heat transfer within the circular tube

Due to symmetry assumption, circumferentially, the inner tube experiences the same temperatures. Axially radiative heat transfer along the tube is not considered as large axial temperature gradients are not expected.

[5]The material properties α and ε for aluminum are not considered as, for modeling of the experimental results, radiative heat transfer is not considered due to its minor contribution at low temperatures.

Stellenbosch University https://scholar.sun.ac.za

2.7 Thermal interaction with ambient

2.7.1 Radiative heat transfer

Each spike interacts through thermal radiation with ambient as well as with neighboring spikes. To compute radiative heat transfer

$$\dot{q}''_{\mathrm{rad},1\to2} = \sigma F_{1\to2}\varepsilon_1\alpha_2(T^4_{\mathrm{s},1} - T^4_{\mathrm{s},2}) \tag{2.45}$$

the view factor $F_{1\to2}$ between interacting bodies 1 and 2 is required, where surface 2 may be a segment of another spike or the sky. The axial incrementation of the spike's outer surface as defined in Figure 2.11 is adopted for computation of radiative heat losses. With the stated assumption of circumferentially constant conditions, each increment in the axial direction can be represented as cylinder segments when considering interaction with ambient.

The computation of view factors of such cylindrical sections to ambient as well as to other neighboring spikes (and their total of cylindrical sections) does not present a straightforward analytical solution, in particular so, as spikes behind the direct neighbors are partially blocked from direct view. The view factors — and consequently, the radiative thermal interaction between neighboring spikes — are approximated by the simulated spike being in interaction with a surrounding frustum shaped surface.

That frustum surface is aligned with the axis of the direct neighboring spikes as depicted in Figure 2.16. It is axially incremented in the same resolution as the spikes, permitting to assign to each frustum increment a spike's cylindrical surface element's temperature. The spike tip is represented as a disc, resulting in a view factor of 1 to ambient.

The view factor between a cylinder's outer surface and a concentric frustum's inner surface segments can be obtained by using readily available equations (from Howell, 2011) to compute the view factor of a cylindrical surface to concentric discs. As

$$\sum_{i=2}^{n} F_{1\to i} = 1 \tag{2.46}$$

must be satisfied all desired view factors between any cylindrical element and any frustum element can established.

Figure 2.16 illustrates the representation of the neighboring spikes by a frustum. The geometry lined out in Table 2.1 and the geodesic frequency of $f = 30$ results in a gap between the spike roots of about 18 mm. From the receiver diameter at spike root of 2 m and 3.3 m at the spike tips follows that the gap between two spikes at the tip is about 75 mm. It is accordingly understood that towards the tip the view factor to ambient may be increasingly underestimated as the gap between neighboring spikes increasingly permits undisturbed view to ambient. In this model the view factor to ambient is reduced to the disc around the spike tip (shown in Figure 2.16).

Stellenbosch University https://scholar.sun.ac.za

Between the different spikes, first order radiative heat transfer is considered, further reflection thereof is neglected. The sky's temperature is defined as 7 °C below the ambient temperature (Stine and Geyer, 2001).

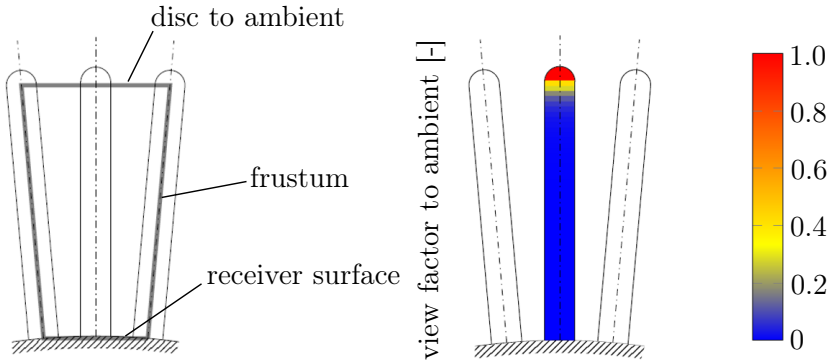

Figure 2.16: Illustration of the frustum representing neighboring spikes for computation of view factors $F_{1\to2}$ (left) and view factors to ambient for a given setup (right)

2.7.2 Convective heat loss

The convective heat transfer to ambient was simulated using a combined heat transfer coefficient for natural convection as well as forced convection

$$h_{\text{combined}} = (h^n_{\text{forced}} + h^n_{\text{natural}})^{1/n}, \tag{2.47}$$

where n is the blending parameter. Çengel and Ghajar (2011) recommend $3 \leq n \leq 4$. A smaller blending parameter leads to increased influence of the smaller heat transfer mechanism, typically the natural convection. A blending parameter of 3.2 has been used by Garbrecht *et al.* (2012), which has been proposed for cavity receivers. So, $n = 3$ serves as a conservative approach, as further used in this model.

The forced convection heat transfer coefficient over the spike is computed by Churchill and Bernstein's equation (Çengel and Ghajar, 2011)

$$h_{\text{forced, cylinder}} = \frac{k}{D}\left(0.3 + \frac{0.62Re^{1/2}Pr^{1/3}}{[1+(0.4/Pr)^{2/3}]^{1/4}}\left[1+\left(\frac{Re}{280\,000}\right)^{5/8}\right]^{4/5}\right), \tag{2.48}$$

where the air parameters are computed at the film temperature $T_{\text{film}} = (T_{\text{wind},\infty} + T_{\text{s}})/2$. The heat transfer coefficient of the tip is approximated with h for a spherical shape, using Whitaker's equation (Çengel and Ghajar, 2011):

$$h_{\text{forced, sphere}} = \frac{k}{D}\left(2 + \left[0.4Re^{1/2} + 0.06Re^{2/3}\right]Pr^{0.4}\left(\frac{\mu_\infty}{\mu_{\text{s}}}\right)^{1/4}\right), \tag{2.49}$$

Stellenbosch University https://scholar.sun.ac.za

where the air properties are computed at free stream temperature (except the viscosity μ_s, which is computed at the surface temperature T_s).

Natural convection heat transfer coefficients are based on empirical correlations provided in Çengel and Ghajar (2011):

$$h_{\text{natural, cylinder}} = \frac{k}{D}\left(0.6 + \frac{0.387Ra^{1/6}}{\left[1 + (0.559/Pr)^{9/16}\right]^{8/27}}\right)^2, \tag{2.50}$$

and

$$h_{\text{natural, sphere}} = \frac{k}{D}\left(2 + \frac{0.589Ra^{1/4}}{\left[1 + (0.469/Pr)^{9/16}\right]^{4/9}}\right), \tag{2.51}$$

where in both equations the fluid properties are based on the film temperature. Equation (2.50) is valid for horizontal cylinders.

The SCRAP receiver forms a geometry with a dense population of spikes, with increasing density towards the spike roots. The receiver is intended to trap radiation from escaping. Towards the spike roots it is equally expected that the air flow of passing ambient air is obstructed. Three wind profiles are considered in this analysis to enable quantifying the sensitivity of the air velocity distribution of a cross-wind along a spike. Figure 2.17 illustrates the considered velocity profiles, which are (a) a simple uniform profile with $u_x = u_\infty$, (b) a linear profile with no wind at the spike root increasing to $u_{\text{tip}} = u_\infty$ and (c) a quadratic profile, equally with no wind speed at the spike root and $u_{\text{tip}} = u_\infty$ at the tip.

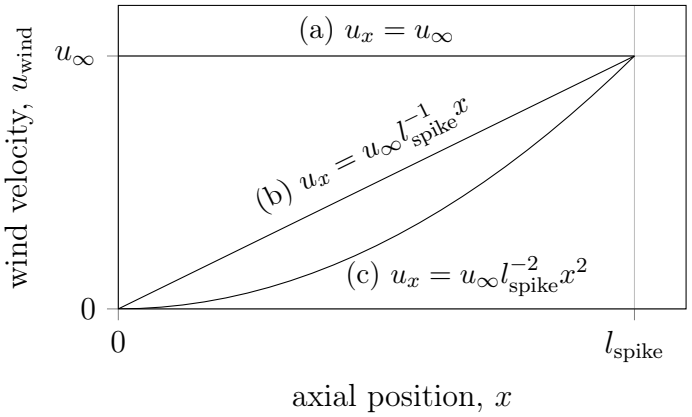

Figure 2.17: Cross-wind velocity distribution considered for natural convection analysis with 0 on the x-axis marking the spike root and l_{spike} the spike tip.

2.8 Drop from turbulent to laminar flow regime

Depending on the geometry and flow parameters selected it can occur that within the rectangular ducts an initially turbulent flow drops to Reynolds

Stellenbosch University https://scholar.sun.ac.za

numbers of $Re \leq 2300$ due to the change in air properties through to the heat input. In this case, the model treats the air flow as well as heat transfer conservatively. For $Re \leq 2300$ correlations (2.42 and 2.43) are used to compute convective heat transfer. Pressure drop is continued to be computed with turbulent flow correlations, providing higher Δp for Reynolds numbers not too far from 2300. The laminar flow regime is considered an undesired flow condition, as laminar flow tends to lead to stratification of the flow, impacting heat transfer capabilities. Further detail into transition or modeling for lower Reynolds numbers is not implemented.

2.9 Grid independence

The grid independence of the simulation environment was investigated in order to identify the required resolution permitting low computational time while equally obtaining reliable results. A resolution of $n = 80$ nodes in axial direction showed suitable for design conditions. A resolution of the fin's grid to greater than $m = 20$ did not show improved results, with the improvement between $m = 10$ and $m = 20$ being marginal. The increase in computational time with increasing the resolution is significant. Therefore, if not stated otherwise, comparative simulations are conducted with $n = 20$ and $m = 10$. Further details to the grid independence analysis are provided in Appendix D.

Stellenbosch University https://scholar.sun.ac.za

Stellenbosch University https://scholar.sun.ac.za

Chapter 3

Experimental Apparatus[1]

This chapter introduces the experimental test setup, its design and functionality as well as the measuring equipment, concluding with a brief outlook on measurement error and uncertainty.

3.1 Test setup

A test setup was designed, constructed and built at the heat transfer laboratories of the department. The design was intended to be modular and interchangeable. This permits testing of multiple phenomena or spike components (or unrelated heat transfer experiments) in a variety of configurations. The experimental test setup is initially introduced in the configuration used to investigate pressure drop and convective heat transfer within the rectangular ducts, including sensory equipment used. The section thereafter provides details on the variability of the setup.

The experimental test setup was conceived with the objective to

- validate the air flow and pressure drop model and
- validate the heat transfer model.

To reduce the amount of unknown factors influencing measurements an experimental setup was designed that operates with steam as a heating fluid, providing a constant surface temperature of nominally 100 °C.

3.1.1 Design

The experimental test setup was developed around the steam chamber, heating an internally finned section. Figure 3.1 illustrates the heated internally finned section with the location of thermocouples as well as pressure taps shown. An

[1]Parts of this chapter have been published in Lubkoll *et al.* (2015), Lubkoll *et al.* (2016*a*) and Lubkoll *et al.* (2016*b*)

Stellenbosch University https://scholar.sun.ac.za

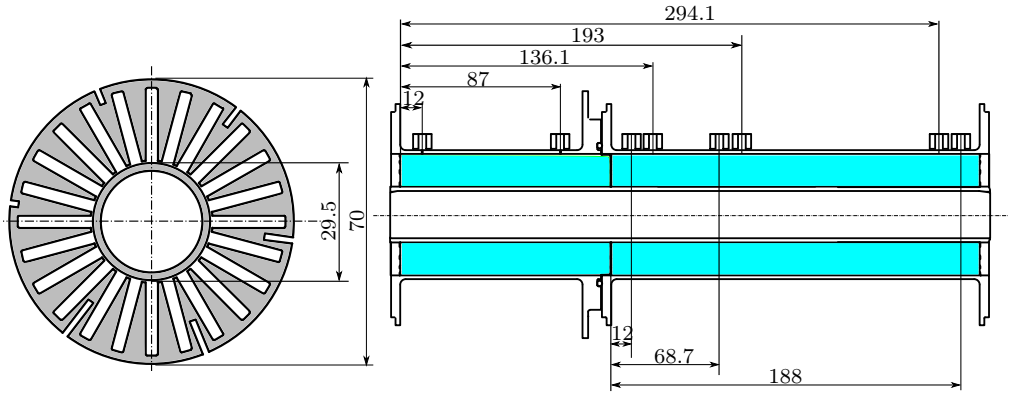

Figure 3.1: Section through internally finned tube (left) at axial position where thermocouples are inserted to depths between 2.0 mm and 10.4 mm. The right hand image indicates the axial distance of static pressure taps (distance readings above the drawing). The distance readings below the drawing show the positions of thermocouple insertion points. Both readings are in reference to the inlet into the rectangular ducts. Note that the two illustrations are not to scale.

internally finned, thermally insulated section precedes the heated section to assist the flow to stabilize and develop.

Figure 3.2 shows the test section of the setup. The photograph (left) shows the experimental section with thermal insulation cladding, excluding the outer cover. The steam compartment is insulated by another steam loop through a wall cavity and therefore not additionally insulated to ambient. The steam compartment is mounted separately (mounting arms can be seen in Figure 3.2, left) and is sealed with silicone gaskets foam towards the flanges, consequently minimizing conduction between the wall and the test section.

The test setup was designed using a number of tube elements with compatible flanges, allowing interchanging or removing of segments, should need be. While an actual spike for a solar thermal receiver consists of three sections, the inner tube, the spike tip/end cap and the internally finned outer tube, the experimental setup provides additional elements. Both configurations see the air passing through the inner tube towards the end cap. There, the flow direction is turned by 180° and enters an annular space. This annular section of 114 mm length is intended to reduce the flow stratification before entering the internally finned section.

A short internally finned section of 114 mm length is used for the air flow within the ducts to develop and the wall friction to stabilize. Using gaskets of 2.5 mm thickness, the flange is thermally insulated by an air gap towards the flange of the heated section. A 200 mm long internally finned heated section is submerged in the steam compartment. For the length of the inner tube being

Stellenbosch University https://scholar.sun.ac.za

within the heated internally finned section its outer diameter was reduced to provide an air gap of about 0.3 mm in order to eliminate thermal conduction from the fin tips to the inner tube. This was done to reproduce the geometry expected for a spike in operation in a SCRAP receiver. There, the inner tube is required to be able to freely move axially, in order to minimize stresses due to different thermal expansion between outer and inner tube.

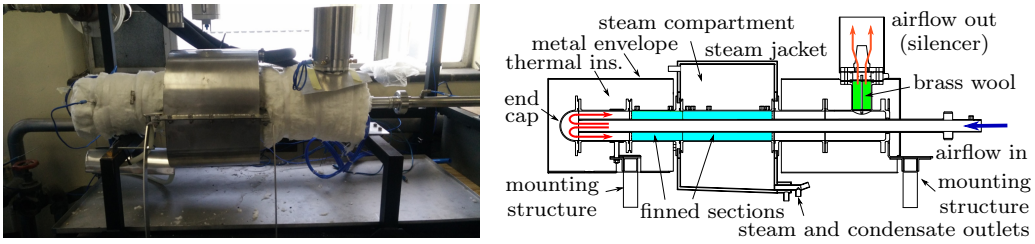

Figure 3.2: Photograph of the heated section including the steam jacket and thermal insulation layers (left) and section (right)

From the downstream flange of the heated section, equally using a 2.5 mm gasket for insulation purposes, the heated air flows through an annular segment of 114 mm length. In the last segment the air flow direction is changed by 90° upwards towards the exhaust silencer. Optionally, the duct towards the silencer can be filled with metal wool (e.g. brass or copper wool) to mix the air flow and achieve a more homogenous air temperature, should the temperature show to be stratified. An adapter flange positioned before the air exits the setup through the silencer houses three thermocouples, each inserted at a different length, to measure the air outlet temperature.

In the configuration of the test setup as presented, the research focus is on confirming the simulated pressure drop of the air flow as well as the simulated heat transfer characteristics. However, the assembly of multiple pieces permits future utilization of the test setup on further details than required for the current research. It is for instance possible to insert the short internally finned section and the end cap or only the end cap into the steam compartment to experimentally investigate heat transfer behavior in the impingement cooling region or the inlet regions. Other geometries of the internally finned section, such as a section with helically swirled fins can be tested. To cater for this flexibility, the steam compartment's fastening arms are mounted on 1 m long rails, permitting variable axial positioning.

Completing the experimental setup is an orifice plate setup to compute the mass flow rate via a differential pressure sensor and measure the system pressure via a gauge pressure sensor. A second device to take pressure drop readings is foreseen for the setup. Here, the drop in static pressure along the inner tube is measured over a distance $\Delta x = 0.5\,\mathrm{m}$, prior to the air entering the test section. Assuming fully developed flow, the air mass flow can be computed via measuring the static pressure drop. This secondary device to establish the

Stellenbosch University https://scholar.sun.ac.za

flow rate is implemented for purpose of confirming the orifice plate calculation, should need be.

Upstream of the orifice plate is a pressure regulator/air filtering unit[2] and a soft-start on/off valve. Figure 3.3 shows the complete setup. Visible on the left hand side of Figure 3.3 is one of the two steam generators employed. One steam generator (regulated; thermal rating of up to 4 kW) supplies the insulation envelope with steam, the other (regulated; thermal rating of up to 6 kW) provides steam to the steam compartment.

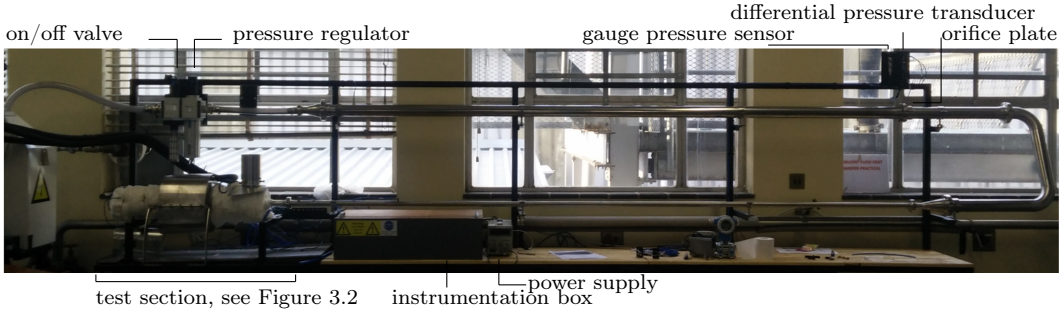

Figure 3.3: Photograph of the test rig in the heat transfer laboratory

Taking the differential pressure reading between the gauge pressure sensor located at the orifice plate and a static pressure tap 15 cm upstream of the test section (see pressure tap on inner tube in Figure 3.2) permits establishing of the inlet pressure and inlet air flow velocity into the test section. This data is then used to run comparative computer simulations. This pressure tap is connected to an air distribution manifold, serving as reference to all differential pressure readings to other downstream taps within the test section. Figure 3.1 shows the location of these pressure taps (all 0.5 mm tap hole diameter). Three taps, equally spaced by 120°, are provided at each axial position.

The rectangular ducts within the internally finned sections are defined by uniform duct width of 3.0 mm. The outer diameter of the tube is 70 mm at a wall thickness of 2.0 mm. The fin tips form an inner diameter of 30 mm. With uniform duct and fin dimensions 24 ducts are distributed over the cross section. The corners of the ducts are rounded off with $r = 0.3$ mm to permit improved manufacturing through wire cutting as well as reduce the stress concentration at the hot spot. More information on manufacturing of the internally finned tube as well as stress analysis is provided in Appendix L as well as Appendix M, respectively.

The narrow width of the ducts makes direct air temperature measurements challenging. To increase the quantity of information available on heat transfer behavior, thermocouples were inserted into the fins at six different depth. The axial location of the thermocouples is indicated in Figure. 3.1. On two further

[2]FESTO MS9-LFR filter regulator; maximal nominal air flow rate 20 000 l/min FESTO (2016)

Stellenbosch University https://scholar.sun.ac.za

axial locations three thermocouples were inserted at equal depth in order to provide a means of assessing axially symmetric behavior of the heat transfer. Figure 3.1 indicates the axial location of the thermocouples (right). The left hand side image shows a section at a point of measurement with six different depths.

3.1.2 Modularity

The test setup was developed with the objective of a modular system in mind. This was intended in order to provide a platform enabling a variety of experiments relating to research on the SCRAP spike. For this purpose the steam compartment is mounted on a rail system, permitting flexible positioning thereof. A number of foreseeable configurations of the experimental setup are illustrated in Appendix J. It is envisaged, as design improvements or further developments are made in future, that these components can be manufactured to fit into the existing experimental setup. Examples can be 3d-printed solutions for helically swirled fins or components with improved design of the duct inlet region.

3.1.3 Instrumentation

Data logger

The data logger used for the experiment is a Keysight 34972A data logger (Keysight Technologies, 2014), its relevant specifications are listed in Table 3.1.

Table 3.1: Specifications of Keysight 34972A data logger; accuracies selected from manufacturer for not exceeding 1 year period since previous calibration

parameter	value	unit
100 mV range		
range error $u_{\mathrm{L},0}$	0.004	%
accuracy in reading $e_{\mathrm{L},1}$	0.005	%
100 mA range		
range error $u_{\mathrm{L},0}$	0.005	%
accuracy in reading $e_{\mathrm{L},1}$	0.05	%

Gauge pressure sensor

As gauge pressure sensor a Firstrate FST800-10B pressure sensor is used (Firstrate, 2016), its relevant specifications are listed in Table 3.2.

Stellenbosch University https://scholar.sun.ac.za

Table 3.2: Specifications of Firstrate FST800-10B gauge pressure sensor

parameter	value	unit
pressure range	0 - 100	kPa
supply voltage	9 - 30	VDC
signal output	4 - 20	mA
accuracy $e_{\mathrm{p}_1,1}$	0.3	%
zero drift	0.02	%/°C
thermal sensitivity shift	0.02	%/°C

Differential pressure transducer

The differential pressure transducer is the Freescale MPX2050DP (Freescale, 2008), its relevant specifications are listed in Table 3.3.

Table 3.3: Specifications of Freescale MPX2050DP differential pressure transducer

parameter	value	unit
pressure range	0 - 50	kPa
supply voltage	10 - 16	VDC
signal output	0 - 40	mV
linearity $e_{\Delta\mathrm{p},1}$	0.25	%
pressure hysteresis $e_{\Delta\mathrm{p},1}$	0.1	%

3.1.4 Design and dimensions of orifice plate flow rate measurement segment

The MPX2050DP pressure transducer provides an accuracy of $\pm 0.25\,\%$ over a span of 50 kPa (Freescale, 2008). The device can withstand static pressure of up to 1500 kPa. The orifice plate flow meter was designed to work with the MPX2050DP. Availability suggested using a 60.3 mm pipe with 1.5 mm wall thickness. A pipe length of 50 diameters ($D = 60.3$ mm) was assumed to be sufficient for practical purposes.

3.2 Applicability of experimental setup to design case

The experimental test setup is designed as a laboratory experiment that, as consequence, has some deviations to the conditions experienced by a spike in design point environment (see chapter 2). For the experiment with an air

Stellenbosch University https://scholar.sun.ac.za

flow rate between 0.04 kg/s to 0.25 kg/s the Biot number Bi is expected as $0.0033 \leq Bi_{\text{exp}} \leq 0.014$. For the reference case spike (as simulated in chapter 5) the Biot number is calculated as $0.021 \leq Bi_{\text{reference}} \leq 0.023$, depending on where along the internally finned tube the parameters are considered.

The good matching in the Biot number originates in the higher heat flux being possible through condensation of steam. The 6 kW steam generator is capable of a theoretical peak flux of 136 kW/m^2 compared to the about 50 kW/m^2 assumed as the design point condition which is further reduced due to thermal losses.

The experimental setup should thus serve the purpose of reproducing heat transfer conditions envisaged for a spike while at laboratory low temperature stage. Further, the higher heat transfer rates should accentuate inaccuracies in the heat transfer model.

3.3 Calibration procedure

The type T thermocouples were calibrated using a FLUKE 9142 dry well calibrator. Individual curve fits were applied to the thermocouples by calibrating for temperatures from 20 °C to 100 °C in 10 °C intervals. An agreement of below ± 0.1 °C was achieved for the curve fits.

The differential pressure transducers were calibrated against a Betz micro-manometer for a range of up to 5000 Pa and against a mercury manometer for the range from 5000 Pa to 50 000 Pa.

3.4 Error and uncertainty

The calibration procedure of the pressure transducer leads to the ability to obtain results at an accuracy superior to the guaranteed values provided by the manufacturer. However, some effects, especially notable at lower differential pressure, such as the zero-drift over varying pressures and for instance the effect of the duration at various pressures were not captured. Consequently, the error and uncertainty analysis is conducted based on device specifications.

The design point uncertainty u_{d} of a measurement is calculated as the root-sum-square of the zero-order uncertainty u_0 of each device and the root-sum-square of its elemental errors u_x (e.g. non-linearity, hysteresis).

$$u_{\text{d}} = \sqrt{u_0^2 + u_x^2} \tag{3.1}$$

Instrument errors are typically provided from data sheets and a value of u_0 of half of the instrument resolution is used (Figliola and Beasley, 2006).

The uncertainties considered are:

Stellenbosch University https://scholar.sun.ac.za

- Measuring Δp, computed as the root-sum-square of the uncertainty $u_{\mathrm{L,d}}$ of the data logger and the uncertainty $u_{\Delta p,\mathrm{d}}$. The errors of the pressure transducer are $e_{\Delta \mathrm{p},1} = \pm 0.25\,\%$ linearity error and $e_{\Delta p,2} = \pm 0.1\,\%$ pressure hysteresis (Freescale, 2008). Temperature hysteresis errors are not considered as the pressure drop over the orifice plate is measured with air at room temperature. Therefore, $u_{\mathrm{d},\Delta p} = \pm\sqrt{e_{\Delta p,1}^2 + e_{\Delta p,2}^2} = \pm\sqrt{0.25^2 + 0.1^2}\,\% = \pm 0.269\,\%$.
  The data sheet of the data logger (Keysight 34972A data logger; measurement was within one year since previous calibration) provides $u_{\mathrm{L},0}$ as $\pm 0.004\,\%$ of range error and an accuracy in reading of $e_{\mathrm{L},1} = \pm 0.005\,\%$ (Keysight Technologies, 2014). The measurement range of the data logger is $0\,\mathrm{mV} - 100\,\mathrm{mV}$, resulting in $u_{\mathrm{L},0} = 4 \times 10^{-3}\,\mathrm{mV}$. With the full scale span of the pressure transducer of 40 mV this corresponds to $5 \times 10^{-3}\,\mathrm{kPa}$ or 5 Pa. The error $e_{\mathrm{L},1}$ on the other hand is directly dependent on the measured value at $\pm 0.005\,\%$ thereof. At $\Delta p = 5000\,\mathrm{Pa}$ the uncertainty of the data logger would be $\pm\sqrt{(5.00\,\mathrm{Pa})^2 + (0.25\,\mathrm{Pa})^2} = \pm 5.01\,\mathrm{Pa} = \pm 0.10\,\%$. The uncertainty is dominated by $u_{\mathrm{L},0}$ and at lower pressures drop values relevant in comparison to the pressure transducer's uncertainty. At higher pressure drop values, the effect of the data logger decreases in significance.

- The uncertainty in the calculation of the air expansion factor ε is calculated as $u_{\varepsilon,\mathrm{d}} = \pm 4\Delta p/p_1\,\%$ (BSI, 1984).

- The uncertainty resulting from the diameters d of the orifice plate as well as D of the upstream tube varying are expressed as $u_{d,\mathrm{d}} = 0.07\,\%$ and $u_{D,\mathrm{d}} = 0.04\,\%$. These are upper limits suggested in BSI (1984). These conservative values are used for further computation.

- The uncertainty $u_{\rho,\mathrm{d}}$ in computing the air density ρ is dependent on the deviation of the ideal gas law from actual air properties as well as the error in establishing the pressure p_1, as ρ is directly proportional to p_1. A comparison was conducted between ρ computed, using the ideal gas law and ρ provided in tabular form in literature VDI (2010). Between $p = 100\,\mathrm{kPa}$ and 1000 kPa the error e_ρ is below $\pm 0.30\,\%$ (at $T_{\mathrm{air}} = 25\,^{\circ}\mathrm{C}$).

  The pressure sensor is a Firstrate FST800-10B pressure sensor, providing an accuracy of $u_{p_1,1}$ within $\pm 0.3\,\%$ of full scale of 1000 kPa (Firstrate, 2016). As with Δp, the total uncertainty of the pressure measurement $u_{p_1,\mathrm{d}}$ is computed with including the error of the data acquisition system. The signal output is current between 4 mA and 20 mA. The error $u_{\mathrm{L},0}$ is $\pm 0.005\,\%$ of range error and an accuracy in reading of $e_{\mathrm{L},1} = \pm 0.05\,\%$ for the reading range of 0 mA and 100 mA (Keysight Technologies, 2014).

  The uncertainty in ρ is computed as the root-square-sum as $u_{\mathrm{d},\rho} = \pm\sqrt{e_\rho^2 + u_{\mathrm{d},p_1}^2}\,\%$

Stellenbosch University https://scholar.sun.ac.za

- The uncertainty in the calculation of the discharge coefficient C is 0.6 % for $\beta \leq 0.6$ and equals β % for $\beta > 0.6$ (BSI, 1984).

The total uncertainty in the flow rate measurement can be calculated as

$$u_{\mathrm{d,orifice}} = \sqrt{u_{\mathrm{d},C}^2 + u_{\mathrm{d},\varepsilon}^2 + 4\left(\frac{\beta^4}{CE}\right)^2 u_{\mathrm{d},D}^2 + 4\left(1+\frac{\beta^4}{CE}\right)^2 u_{\mathrm{d},d}^2 + \frac{1}{4}u_{\mathrm{d},\Delta p}^2 + \frac{1}{4}u_{\mathrm{d},\rho}^2}. \quad (3.2)$$

It is assumed that the geometric shape of the setup will be in accordance with the standard.

In addition, an error e_L, depending on the pipe length may be added. This uncertainty is dependent on β. The standard lists in tabular form required minimum pipe length upstream of the orifice plate, depending on further upstream devices/fittings. The test setup consists of pressure regulator followed by the flow rate regulator, followed by an expander into the pipe upstream of the orifice plate. The highest requirements listed are for two or more 90° bends in different planes. If the upstream pipe shorter than the required length (function of β), a penalty of ± 0.5 % is added to the error of equation 3.2. The standard is valid for $Re \leq 10^8$, suggesting that the guidelines are conservative at lower Reynolds numbers.

For reference, the hydraulic developing length $L_{\mathrm{hy,t}} = d\,0.623Re^{0.25}$ for a Reynolds number of 6×10^5 is 1.0455 m.

Stellenbosch University https://scholar.sun.ac.za

Stellenbosch University https://scholar.sun.ac.za

Chapter 4

Experimental Method and Results[1]

This chapter provides details on how the experiment was conducted and outlines the procedure to compare the simulation model with the experimental results.

4.1 Experimental procedure

Experiments were conducted following the procedure outlined in this section. Figure 4.1 illustrates the typical experimental procedure by showing the pressure drop $\Delta p_{\text{orifice}}$ of the pressure transducer measuring pressure drop over the orifice plate as well as the pressurized air stream's inlet, $T_{\text{air,in}}$, as well as outlet, $T_{\text{air,out}}$, temperatures. The data logging equipment was set to continuous logging, leading to an interval of about 2.6 s between reading of the same port (sampling frequency of 0.38 Hz).

Zero-reading Before the pressurized air flow is started, a set of zero-readings of all devices is recorded (1).

Stabilizing air inlet temperature The pressurized air compressors and buffer vessel are situated approximately 20 m from the experimental setup. The uninsulated pipes are exposed to ambient outside the building. This can result in temperature deviation from available bulk air to air supplied directly after opening the air flow. In (2) a couple of minutes air flowing through the system permit the air inlet temperature to stabilize.

Pressure drop readings The pressure regulator is manually actuated and the inlet air pressure is adjusted in approximately 50 kPa intervals, increasing the air mass flow $\dot{m}_{\text{air}}$ through the system (3). Each pressure level is maintained

[1]Parts of this chapter have been published in Lubkoll *et al.* (2016*b*)

Stellenbosch University https://scholar.sun.ac.za

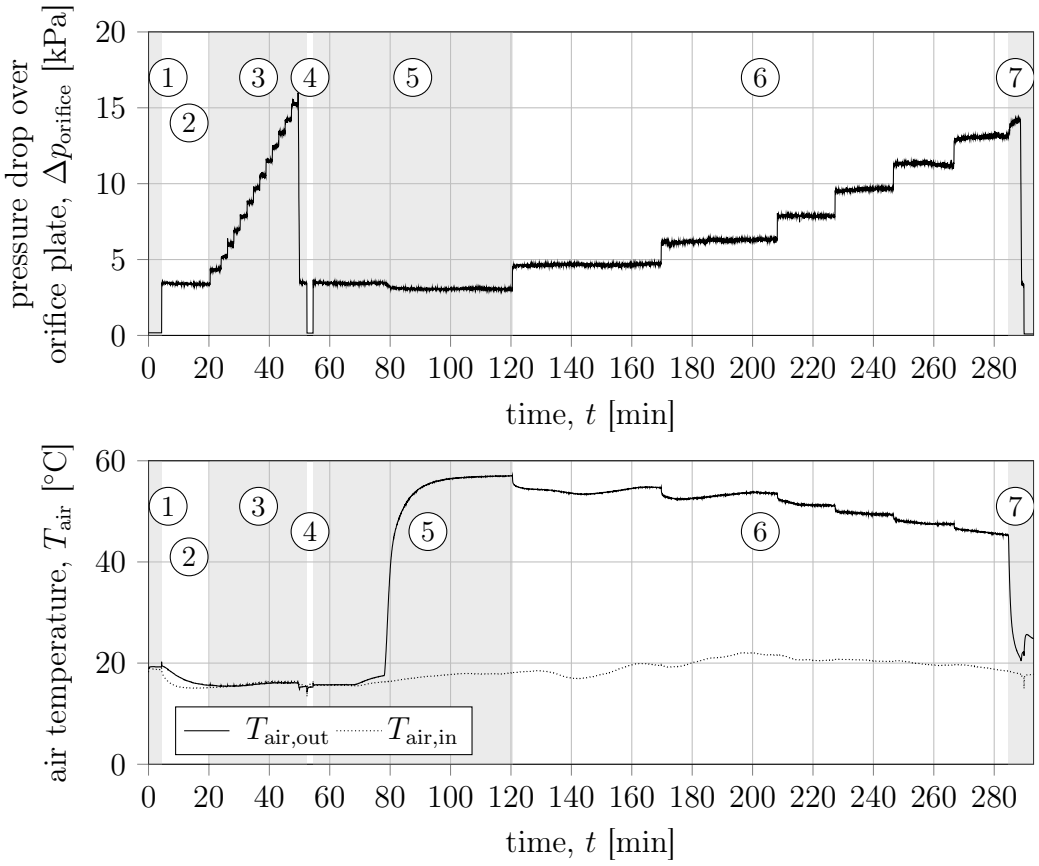

Figure 4.1: Illustration of a complete test cycle showing the pressure drop over the orifice plate, $\Delta p_{\text{orifice}}$, as an indication of air flow rate, and the air inlet and outlet temperatures, $T_{\text{air,in}}$ and $T_{\text{air,out}}$, respectively. The spikes in pressure drop readings after (1) and (4) span a single measuring point and are attributed to using the on/off valve to turn on the air flow instead of carefully increasing it, using the pressure regulator.

for approximately 2 min to increase the number of data points over which readings are averaged.

Zero-reading The air flow is turned off and the system automatically depressurizes. Another set zero-readings (4) is taken as an indication for the zero-drift of the pressure transducers.

Heating The air flow is turned on and the steam generators (one for insulation envelope, one for steam compartment) are activated (5). After approximately 70 min the steam generator heating the steam compartment' envelope supply steam and modest temperature increase in the outlet temperature is observed. Just after 80 min the steam compartment is flooded with steam and the outlet temperature readings rise rapidly. As the air is heated and expands the flow

Stellenbosch University https://scholar.sun.ac.za

rate drops slightly as the inlet air stream is regulated via the pressure regulator maintaining constant inlet pressure. The inlet pressure remains constant until steady state conditions are assumed at about minute 130 min.

Varying flow rates The procedure outlined above is repeated for further flow rates (6). The air inlet pressure is increased in intervals of approximately 100 kPa and the temperatures are observed until steady state is reached. Note that the first reading in (6) seems to be dropping in outlet temperature at the time of adjustment of the inlet pressure. The drop is, however, of the same rate as the drop in inlet temperature, indicating steady state. As the air flow rate increases, the thermal power provided by the steam needs to be increased. This is done manually by adjusting the steam generator' supply voltage. Live steam temperature readings as well as visual observation of steam flow on the steam compartment' outlet indicate sufficient steam flow rate. At approximately 170 min the steam flow rate was adjusted after observing a slight temperature drop within the steam compartment. The steam generators are adjusted manually in order to avoid pressurization of the steam system.

Cooldown After last desired steady state readings are taken, the steam generators are turned off (7). With the air outlet temperature dropping, the flow expansion is reduced and immediately an increase in pressure drop over the orifice is observed as the air flow rate increases (keeping inlet pressure constant). Approximately 5 min prior to the end of the data logging the air flow is turned off and another set of zero readings of the pressure transducers is obtained. The outlet temperature increases to meet the temperature of its mounting flange due to conduction along the sheath.

4.2 Data selection and preparation

In order to compare the experimental observations with the simulation model the data acquired from the steady state condition measurement of (3) as well as (5) and (6) requires to be analyzed and processed.

In adiabatic measurement section (3) the data set for each interval is averaged to obtain mean values, carefully inspecting the selected data for omitting transient readings. The reading of the supply voltage permits adjustment of the differential pressure reading. The readings in Volt are converted to Pa differential pressure, applying the average slope and the calibration curves for each pressure transducer. The Ampere reading of the gauge pressure sensor is converted to kPa of gauge pressure. The ambient pressure is obtained after the measurement from the university's weather station at the engineering fac-

Stellenbosch University https://scholar.sun.ac.za

ulty[2]. All thermocouple readings are corrected using their respective calibration curves.

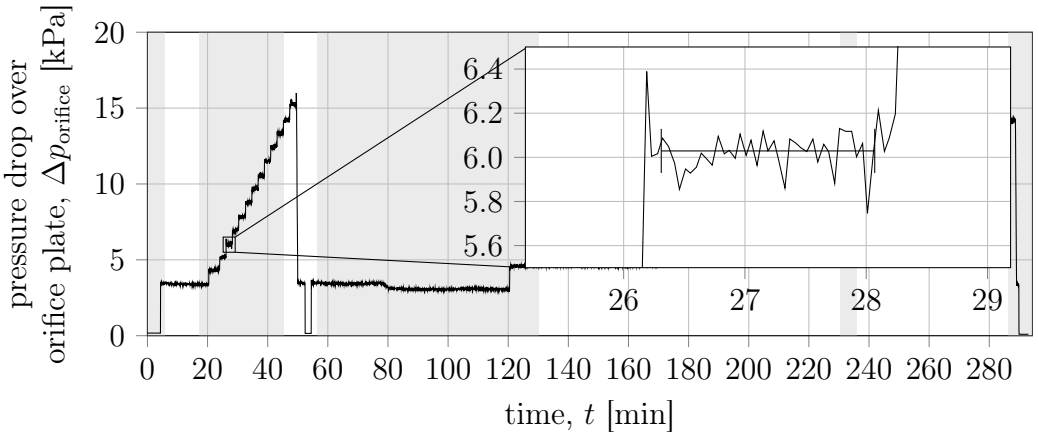

Figure 4.2: Detail of the pressure drop over the orifice plate, $\Delta p_{\text{orifice}}$, during steady state condition. The horizontal line in the excerpt shows the average pressure drop value over the duration delimited by the orthogonal end markers. These are typically placed about three data points from beginning/end of the steady state condition.

The air properties can then be computed, utilizing the equations provided in Appendix K.2. With that the air mass flow rate, $\dot{m}_{\text{air}}$ (and thus, the air velocity, u_{air}), can be computed from the static pressure drop over the orifice plate from

$$\dot{m}_{\text{air}} = CE\varepsilon\frac{\pi}{4}d^2\sqrt{2\Delta p \times \rho_1}, \tag{4.1}$$

where C is the coefficient of discharge, E the velocity approach factor and ε the air expansion factor. For further details towards computation C, E and ε according to the British standard for fluid flow in closed conduits see Appendix O. The flow velocity can be computed with from $\dot{m}_{\text{air}}$.

4.3 Simulation of experimental conditions

For each of the steady state data points generated from (3) and (6) (in chapter 4.1) the simulation model was used to generate results permitting to identify of the applicability of the model.

4.3.1 Adaption of simulation model

The simulation models required amendments to suit the scenario of the experimental setup. The experiment is conducted at air temperatures below about

[2]http://weather.sun.ac.za/graphs/barometer/

Stellenbosch University https://scholar.sun.ac.za

100 °C. A set of air property curve fits was generated for this purpose (for more detail see Appendix K.2). For the experimental modeling, the internal radiation models are deactivated to reduce computational expense.

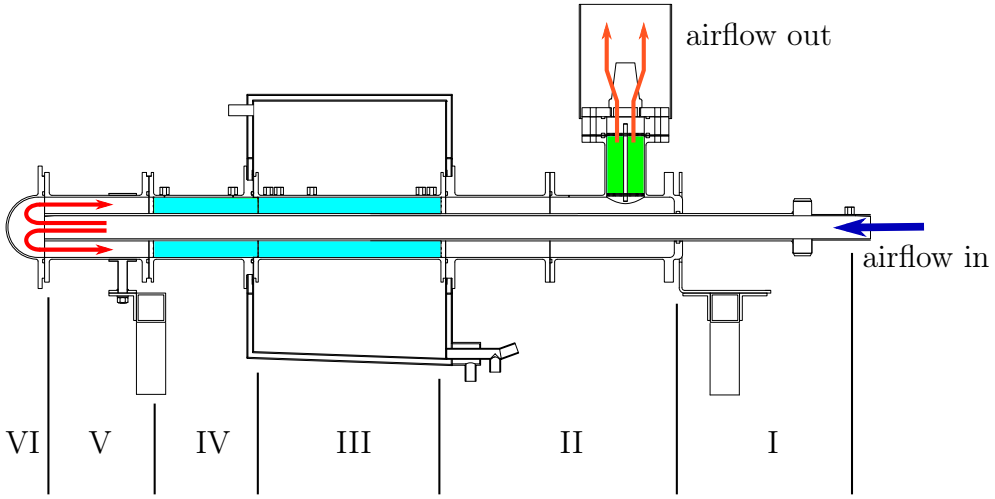

Figure 4.3: Section through experimental setup indicating areas of model adaption.

The simulation model for a spike as described in chapter 2 represents section III, VI and to some degree section II. Amendments are necessary to represent the pressure drop over the extended length of the inner tube, for the addition of the annular section in V and the internally finned section in IV. The heating of the test specimen is confined to section III, permitting representation of the named additional pressure drops within single nodes.

The pressure drop calculation over an extended length of the inner tube is straightforward by computing the friction factor f_{D} and applying the Darcy-Weisbach equation:

$$\Delta p = f_{\mathrm{D}} \frac{l\rho}{2} \frac{u^2}{d_{\mathrm{hd}}} \tag{4.2}$$

More generically, irrecoverable pressure drop over an occurrence can be expressed as a function of a friction coefficient ξ and a reference velocity (typically inlet or upstream) u_1:

$$\Delta p = \xi \frac{\rho u_1^2}{2} \tag{4.3}$$

Equation 4.3 is applied for computing the pressure drop over the spike tip (VI) as outlined in chapter 2. The pressure drop in (V) and the blunt inlet into the finned section (IV) are initially assumed with literature values and later adjusted to fit the simulation model to the experimental results. With the inlet into finned section IV including the pressure drop for the flow to develop, the pressure drop along segment (IV) can be solved by a single equation as

Stellenbosch University https://scholar.sun.ac.za

described for the inner tube. A first set of experimental results was employed to adjust ξ_{tip} as well as ξ_{duct} to fit the observed results (both are initially conservative assumption based on literature).

At (VI) the air exits the inner tube and as its flow direction is changed by 180° the cross sectional area increases, leading to pressure recovery. This is calculated applying the Bernoulli equation. The irrecoverable pressure loss as part of the flow expansion is computed using

$$\Delta p = \left(1 - \frac{A_1}{A_2}\right)^2 \frac{\rho u_1^2}{2} \tag{4.4}$$

where A_1 and A_2 are the cross-sectional areas of the inner tube and the outer annular space, respectively (VDI, 2010).

The heating of the air flow in the inner tube along section II is represented in the original model where this area constitutes the outer chamber. Consequently the pressure drop along the inner tube is split into two single node equations, one representing the pressure drop from the inlet to section II, the other the pressure drop in IV and V.

The simulation model was equipped with a number of switches that work on an on/off function to control radiative heating of the spike, constant surface temperature heating, radiative and convective (forced and natural) heat loss to ambient. A further switch was implemented to change between material properties (see Appendix K for properties of air). Here, the heating via a constant surface temperature was activated and material properties of aluminum grade 7075 T6 selected (thermal conductivity was set as 130 W/m K, irrespective of temperature). Thermal interaction with ambient as well as internal radiation were deselected.

4.3.2 Modeling of experiment

Via input files the experimental steady state results were re-produced using the simulation model. The extracted simulation parameters described in section 4.2 served as the respective input parameters.

4.4 Experimental results

The agreement between experimental measured results and the prediction using the simulation model are discussed.

4.4.1 Pressure drop and friction factor

Along the heated section, three pressure taps were implemented to measure differential static pressure to the inlet, consequently permitting computation of static pressure drop along the rectangular ducts. Table 4.1 provides the

Stellenbosch University https://scholar.sun.ac.za

measured flow conditions and measured pressure drop compared to simulated results. The pressure drop is listed as its slope over axial distance x, making a comparison between simulated and measured results more straightforward for adiabatic conditions (where change in f_D over x is negligible).

Table 4.1: Conditions of adiabatic experiment and resulting slope of pressure drop $\Delta p'$

p_{in} [kPa]	T_{in} [°C]	$\dot{m}$ [kg/s]	$\Delta p'_{sim}$ [Pa/m]	$\Delta p'_{exp}$ [Pa/m]
270	15.6	0.0408	948.3	933.2
325	15.6	0.0510	1217	1188
372	15.7	0.0598	1407	1422
419	15.9	0.0685	1583	1583
468	16.0	0.0779	1776	1717
515	16.2	0.0869	1955	1885
568	16.4	0.0967	2142	2037
615	16.5	0.106	2310	2308
662	16.7	0.115	2475	2543
714	16.8	0.125	2648	2671
765	16.8	0.134	2821	2797
813	16.8	0.143	2978	2964
858	16.8	0.152	3127	3176
909	16.8	0.162	3311	3276

It is apparent that the simulation model is consistently in excellent agreement with the pressure drop slope based on the measured experimental results. The deviation by which the experimental result is above the prediction is plotted in Figure 4.4 on the left hand side.

The right hand side of Figure 4.4 illustrates the deviation in the friction factor f_D between the coefficient computed from simulation data as well as the coefficient computed from the experimental results. The friction factor is obtained from re-arranging the Darcy-Weisbach equation (4.2) as

$$f_D = \Delta p \frac{d_h}{l} \frac{2}{\rho u^2} \tag{4.5}$$

and applying the adequate variables. The simulation model underestimates the friction factor consistently across the investigated range of flow rates. The mean deviation is 0.9 % and all data points lie within ±6 %.

Stellenbosch University https://scholar.sun.ac.za

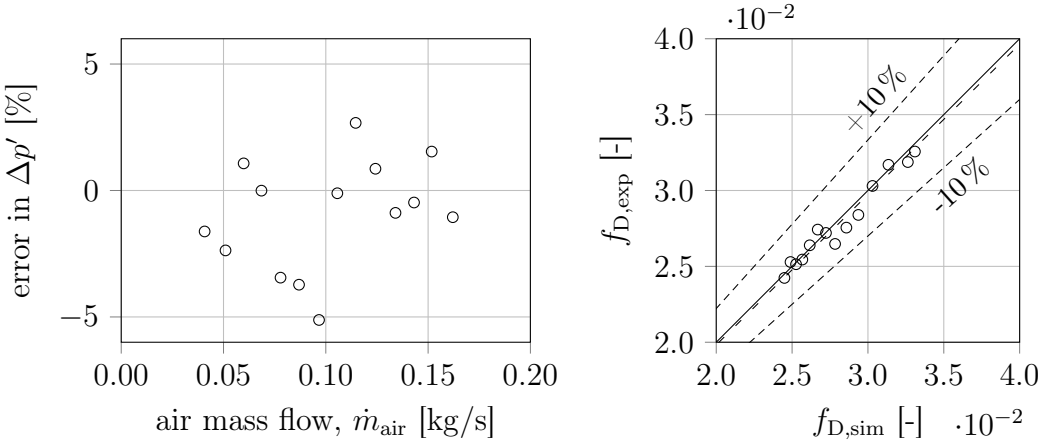

Figure 4.4: The deviation of the measured pressure drop slope error, $\Delta p'$, (left) over the comparison between $f_{\text{D,sim}}$ and $f_{\text{D,exp}}$, computed from experimental data (right). The loosely dashed line indicates the average deviation of the measurement results to the simulated data. For reference the densely dashed lines delimit $\pm 10\,\%$ devation.

4.4.2 Pressure drop over spike tip

The air flow exits the inner tube at the spike tip and is returned by 180° in flow direction. At the same time the air flow experiences expansion as the cross sectional area into the annulus increases. Then, the air flow is directed into the rectangular ducts. Each of these occurrences is modeled either using a friction coefficient ξ or pressure. Initial assumption for the friction coefficients ξ were based on literature values and were $\xi_{\text{tip}} = 0.72$ based on the nearest approximation in Idelchik (1986) and $\xi_{\text{duct}} = 1.69$, conservatively selected as applied for sharp edged inlet into a tube bundle (VDI, 2010).

Figure 4.5 shows the measured static pressure along the internally finned sections. Additionally shown are three predictions from the computer model. These represent two bounding models, one with the conservative estimates for both ξ, one with no irrecoverable pressure loss. A mean line is shown for $\xi_{\text{tip}} = 0.3$ and $\xi_{\text{duct}} = 0.1$.

Correcting the static pressure using the adjusted friction coefficients prior to the internally finned section has a marginal effect onto the pressure drop, the range spanned between the two bounding models leads to below $0.5\,\%$ deviation in pressure drop.

The spike tip would, for a receiver application, possibly be equipped with a nozzle to improve impingement cooling heat transfer characteristics. The inlets into the rectangular ducts would likely not be blunt and perhaps protrude into the tip region. As the annular space behind the tip would be omitted, the vortex might form within the rectangular ducts. These factors suggest that the design of a spike for a receiver application deserves further attention. For the purpose of this study, $\xi_{\text{tip}} = 0.3$ and $\xi_{\text{duct}} = 0.1$ serve as sufficient indicators

Stellenbosch University https://scholar.sun.ac.za

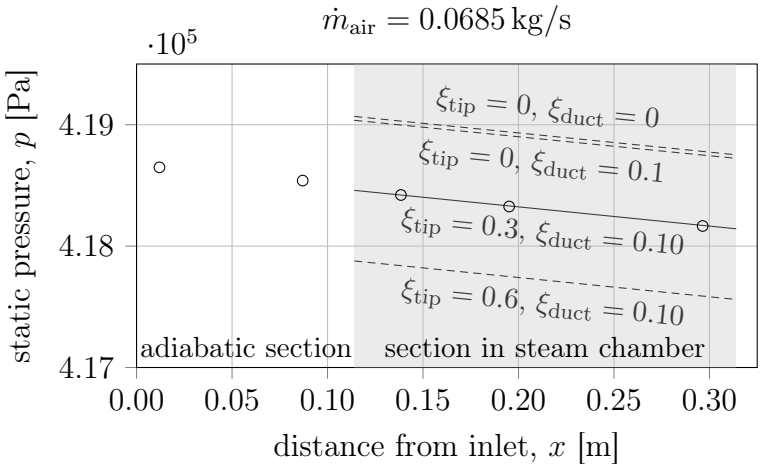

Figure 4.5: Measured static pressure data points (circles) along the internally finned adiabatic section and section within the steam chamber (no heating) compared to three simulation results for varying ξ_{tip} and ξ_{duct}.

to be used, noting that of course any number of combinations between these two coefficients could correct a line as seen in Figure 4.5 to match the current location.

4.4.3 Thermal characteristics

The thermal performance of the experimental spike sections is quantified by two means. Firstly, air temperatures are measured, namely the air inlet temperature T_{in}, the air temperature at the spike tip T_{tip} as well as the air outlet temperature T_{out} at the exhaust flange. Further insight is attained by measuring metal temperatures within the fins. To improve confidence into the results the condensate rate on the outlet of the steam compartment is measured to permit comparison with an energy balance.

The Gnielinski equation, as earlier shown in equation (2.40), was used to compute the Nusselt number as it is suitable for lower Reynolds numbers in the turbulent flow regime and permits computation of local Nusselt numbers (Gnielinski, 2010):

$$Nu_x = \frac{(f_{\text{D}}/8)Re\,Pr}{1 + 12.7\sqrt{f_{\text{D}}/8}\,(Pr^{2/3} - 1)} \left[1 + \frac{1}{3}\left(\frac{d_{\text{h}}}{x}\right)^{2/3}\right] \tag{4.6}$$

Equation (4.6) computes the Nusselt number at any position x, where $x = 0$ at the beginning of the internally finned heated section.

Figure 4.6 shows the measured outlet air temperature, $T_{\text{air,out,exp}}$, compared to the simulated temperature, $T_{\text{air,out,sim}}$. With increasing air flow rate $\dot{m}_{\text{air}}$ the outlet temperatures decrease as one would expect. The measured temperature was consistently lower than the simulation model's prediction. With the

Stellenbosch University https://scholar.sun.ac.za

measured spike tip temperatures, $T_{\text{air,tip,exp}}$, being slightly higher than the predicted, $T_{\text{air,tip,sim}}$. This deviation was slightly more pronounced when plotting the differential temperatures, ΔT_{air}, between the spike tip temperature, $T_{\text{air,tip}}$, and the outlet temperature.

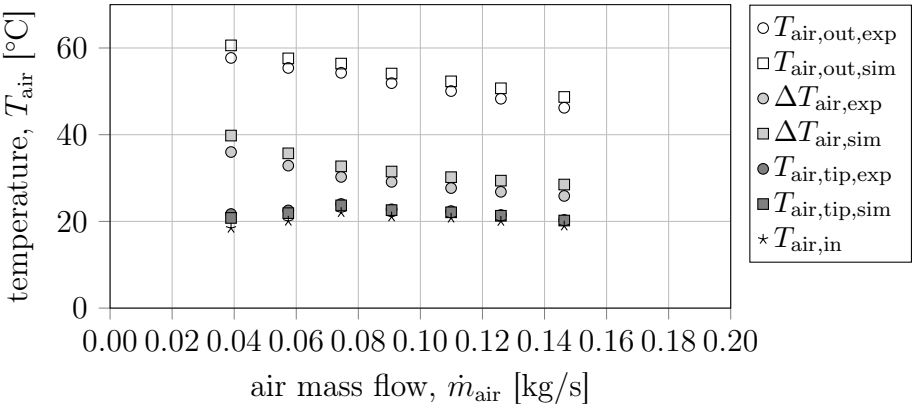

Figure 4.6: Comparison of measured $T_{\text{air,out,exp}}$ to simulated $T_{\text{air,out,sim}}$ outlet air temperature for different air mass flow rates $\dot{m}_{\text{air}}$. The markers $\Delta T_{\text{air,out,exp}}$ and $\Delta T_{\text{air,out,sim}}$ indicate the temperature rise between the spike tip temperature (measured, $T_{\text{air,tip,exp}}$, and simulated, $T_{\text{air,tip,sim}}$, respectively) and air outlet.

Figure 4.6 does indicate that the simulation model, while showing a fairly stable offset, predict the changes with increased air flow rate well.

A further comparative check on the experimental results was conducted by taking condensate readings to establish two sets of energy balances. From weighing the condensate and using the enthalpy of condensation, h_{fg}, to compute an estimate for the temperature rise $\Delta T_{\text{air,bal}}$ via

$$\Delta T_{\text{air,bal}} = \frac{\dot{Q}_{\text{con}}}{\dot{m}_{\text{air}} c_{\text{p,air}}} \tag{4.7}$$

with

$$\dot{Q}_{\text{con}} = \dot{m}_{\text{con}} h_{\text{fg}}. \tag{4.8}$$

Using the total condensate flow rate to calculate the temperature increase $\Delta T_{\text{air,bal}}$ provides a upper boundary to the possible air outlet temperature, as it excludes heat losses to ambient.

A lower boundary was established by taking condensate reading when the air flow was at 0 m/s. Here, experimental setup was heated and over time the heat would spread axially through conduction until a steady state condition between heating and losses to ambient (conductive and convective) is reached. Through heating with steam the experienced highest temperatures are about 100 °C. Lacking the cooling effect of the forced convection through the internal air flow the convective and conductive losses are higher than during experiments.

Stellenbosch University https://scholar.sun.ac.za

Therefore, when deducting this condensate measurement from condensate measurements during an experiment a minimal boundary was created.

Figure 4.7 shows the temperature increase in the air flow between the air inlet temperatures and the simulates/measured air outlet temperatures. Here, the two boundaries established through the energy balances are also shown.

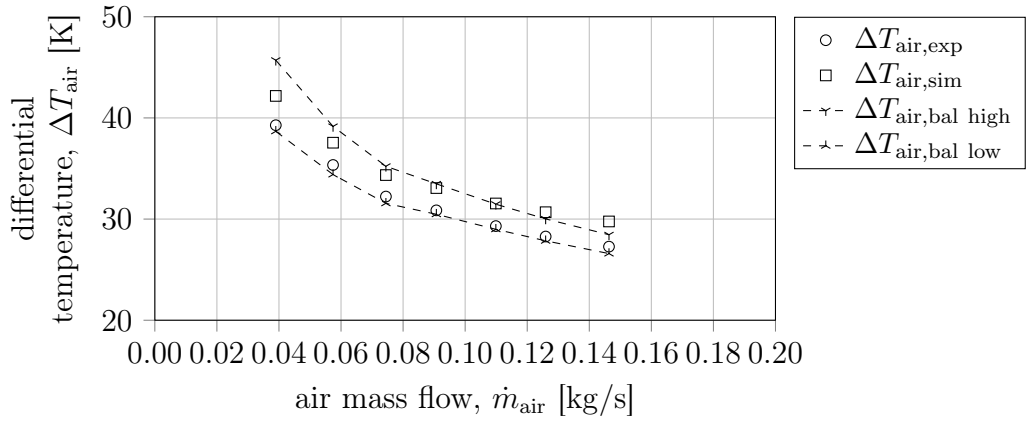

Figure 4.7: Differential temperature between air inlet temperature measurement, $T_{\text{air,in}}$, and outlet temperature measurement, $T_{\text{air,out,exp}}$, compared to differential temperature simulation at tip, $T_{\text{air,tip,sim}}$, and outlet, $T_{\text{air,out,sim}}$. The top and bottom line delimit the range between the temperatures increase computed from the energy balance $\Delta T_{\text{air,bal}}$.

Notably, the measured temperature rise was closer to the lower boundary at low air flow rates and approached the upper boundary at higher air flow rates. Such a trend can be explained by lower air flow rates resulting in higher air as well as material temperatures in the setup and resulting higher thermal losses. With higher flow rates, temperatures and thermal losses reduce. Consequently, the line indicating the lower energy balance becomes increasingly conservative.

A similar observation can be made from Figure 4.8, where the heat rate $\dot{Q}$ is plotted from various sources. These are the differential air temperatures between inlet and outlet (from simulation as well as experiment) and computed from the condensate measurement. Included is the error ε between the simulation as well as experimental heat rate. The deviation ε between the simulated heat rate and the experimental heat rate is relatively stable at around 7 %.

Fin temperature measurements Initially, the design of the experimental setup foresaw an 0.5 mm air gap between the flange of the heated section and the flange of its neighboring sections. It turned out impractical to maintain a constant gap while providing mechanical strength and simultaneously a known, low, thermal conduction across the distancing material. As a result it was opted to mount a silicone gasket between the flanges. This way, the conductive

Stellenbosch University https://scholar.sun.ac.za

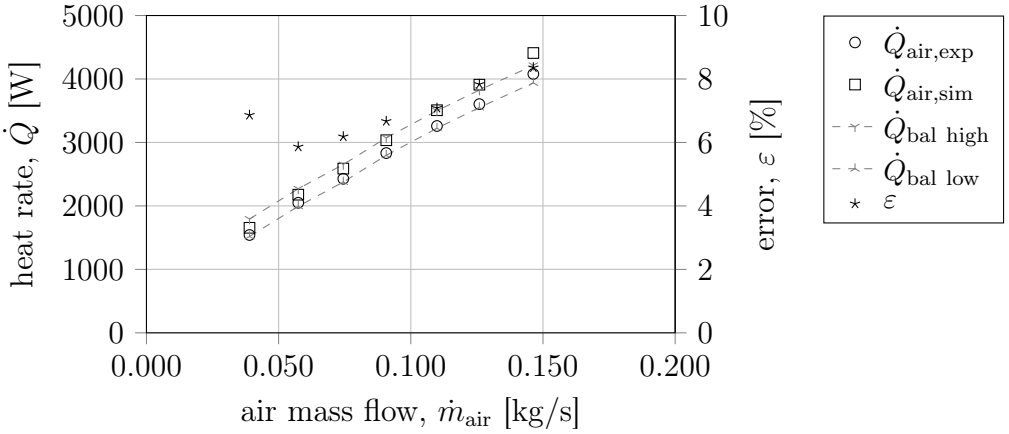

Figure 4.8: The heat rate $\dot{Q}$ computed from differential air temperatures as well as from condensate measurement. The deviation between the simulation model and experimental result is shown on the right axis.

surface, thickness and material properties are known, while at the same time the bolts tightening the flange can be adequately tightened.

The consequence was a quantifiable thermal conduction across the flange of approximately 2.5 mm thickness (after tightening the bolts) gasket installation. A consequence of the increased gap, compared to the initial 0.5 mm is that the gap axially separating the fins of the heated section and the upstream section equally increases by 2.5 mm. Resultingly, the air flow pattern may be disturbed when entering the heated section. Further, the air flow increasingly impinges on the face surface of the heated sections' fins. Both effects may result in equation (4.6) underestimating the Nusselt number.

Figure 4.9 shows the temperature distribution axially along the center plane of a fin (for $\dot{m}_{\text{air}} = 0.0390\,\text{kg/s}$). Two further plots for the flow rates of $\dot{m}_{\text{air}} = 0.0907\,\text{kg/s}$ and $\dot{m}_{\text{air}} = 0.146\,\text{kg/s}$ are shown in Figure 4.10 and Figure 4.11, the plots illustrating the results for the remaining flow rates are contained in Appendix P.

It is notable through the provided images, ranging through low, medium and high flow rates, that relatively good agreement between measured and predicted temperatures for the central and outlet side thermocouples appears. With increasing flow rate, the inlet side thermocouples increasingly show lower measurements than predicted over the entire depth of the fin (radial direction). This can be due to a locally underestimated heat transfer coefficient. Further, the entrance region is experiencing the highest heat transfer, as the local Nusselt number is high, paired with the coldest air temperature, resulting in the highest radial heat flux through the fins. It is thus expected that effects of thermocouple holes reducing radial conduction (by reducing conductive cross sectional surface) are most pronounced here.

Stellenbosch University https://scholar.sun.ac.za

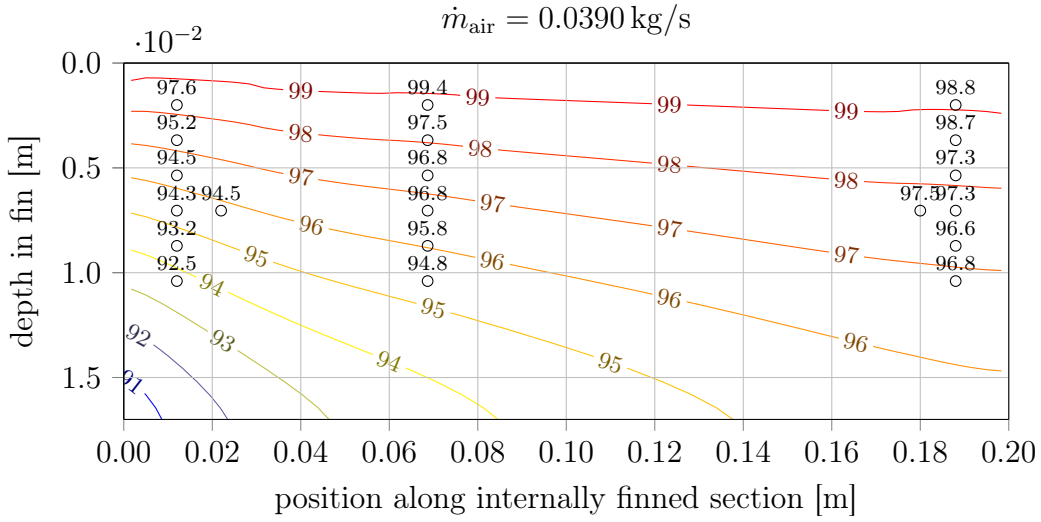

Figure 4.9: Contour plot of simulated temperature profile along fin center in heated section for $\dot{m}_{\text{air}} = 0.0390\,\text{kg/s}$. The y-axis shows the depth in the fin with 0 being the outer surface exposed to the steam. Experimental results are shown above the respective black circles, indicating the position of the measurements.

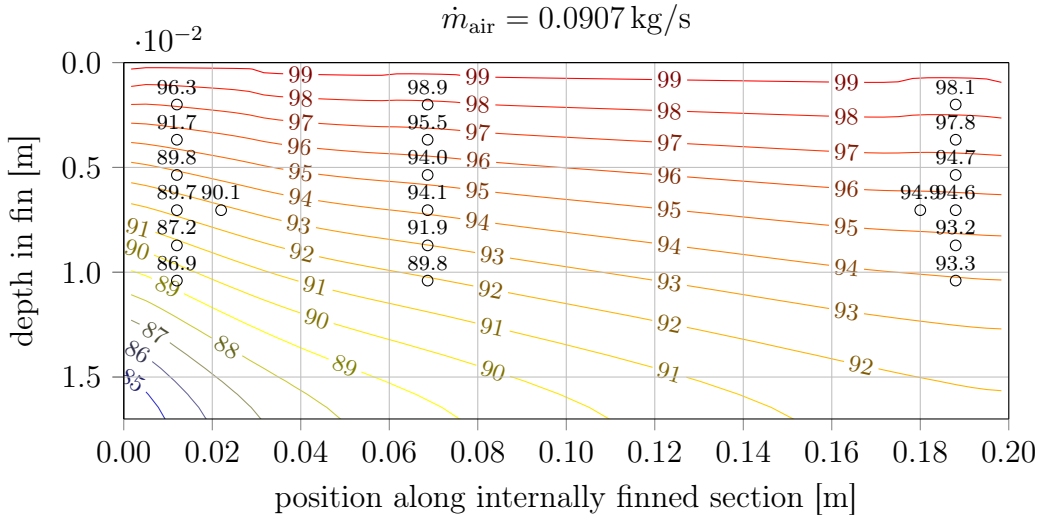

Figure 4.10: Contour plot of simulated temperature profile along fin center in heated section for $\dot{m}_{\text{air}} = 0.0907\,\text{kg/s}$. The y-axis shows the depth in the fin with 0 being the outer surface exposed to the steam. Experimental results are shown above the respective black circles, indicating the position of the measurements.

Stellenbosch University https://scholar.sun.ac.za

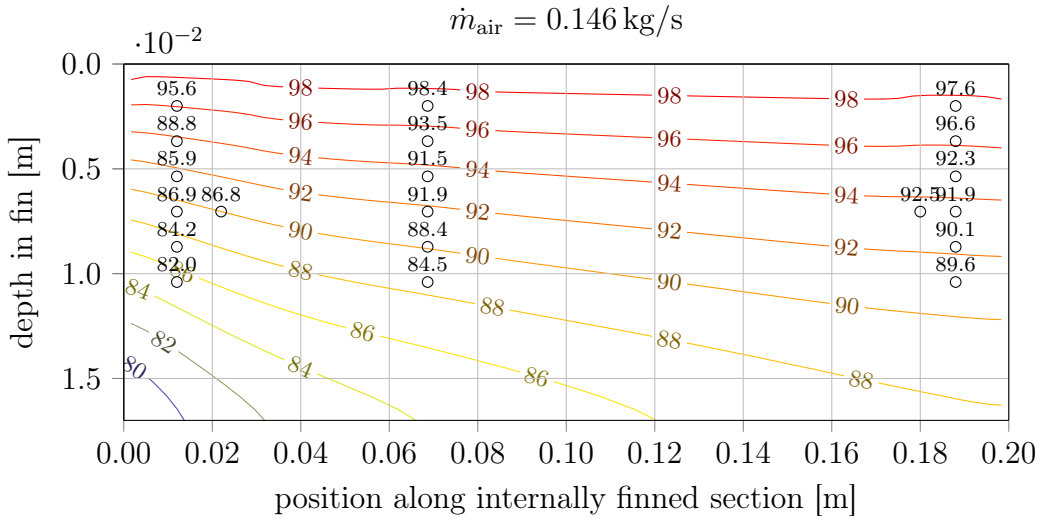

Figure 4.11: Contour plot of simulated temperature profile along fin center in heated section for $\dot{m}_{\text{air}} = 0.146\,\text{kg/s}$. The y-axis shows the depth in the fin with 0 being the outer surface exposed to the steam. Experimental results are shown above the respective black circles, indicating the position of the measurements.

4.5 Conclusion

This section summarizes the results of the conducted experiment, initially. Further attention is devoted to an analysis of factors that have influence the on the experimental readings with the purpose of quantifying these.

4.5.1 Conclusion of experimental results

The interpretation of the experimental part under adiabatic conditions confirms the suitability of the simulation model. The deviation in pressure drop along the internally finned section does not exceed 10 %, while the average deviation over a series of measurements showed to be minor with below 2 % mean over prediction of the model. Friction coefficients for the spike tip as well as the blunt entrance into the rectangular ducts were established from experimental data empirically.

The thermal characteristics discussed in subsection 4.4.3 indicate reasonable reproduction of actual behavior observed with the simulation model. The measured outlet temperate was, however, consistently below the model prediction, an effect slightly increasing with increasing air flow rates. The deviation in heat transfer from the steam side to the pressurized air flow through the spike body was estimated at about 7 %, varying by about ± 1.5 % for different flow rates without showing notable trends of deviation correlating to flow rates. The simulation model shows good agreement in representing the behavior of outlet

Stellenbosch University https://scholar.sun.ac.za

temperature in response to varying air flow rates, confirming its suitability.

A further analysis of the temperature measurements within the fins indicates that towards fully developed flow conditions (outlet side) the agreement between the simulation and experimental measurements increases, supporting the model. A similar Biot number, Bi, for experiment as well as possible real operating conditions suggest suitability of the fin model in its presented form for the purpose of modeling a spike under CSP application conditions.

The results suggest in summary that sufficient confidence can be given to the model quality to utilize the model to predict and understand the performance characteristics of a spike and the SCRAP receiver.

4.5.2 Correction of experimental results

This subsection aims to address a number of influences on the temperature measurement and the potential effect on the measurement result. More detail on the influences and their quantification can be found in Appendix Q.

The most notable influences on the temperature measurement are axial thermal conduction over flanges and convective heat transfer to the inner tube between the heated section and the outlet. Conduction of heat could be approximated by mounting thermocouples on flanges. Convective heat transfer to the inner tube presented itself challenging to quantify due to the flow path of the air being initially parallel to the inner tube but then being redirected 90° upwards.

Figure 4.12 shows the differential temperature when applying the minor corrections for thermal conduction upstream and downstream of the heated section as well as the mounting bracket. As outlined in Appendix Q the corrections tend to cancel each other out, shifting each measurement point by 0.3 K towards the simulated value.

Stellenbosch University https://scholar.sun.ac.za

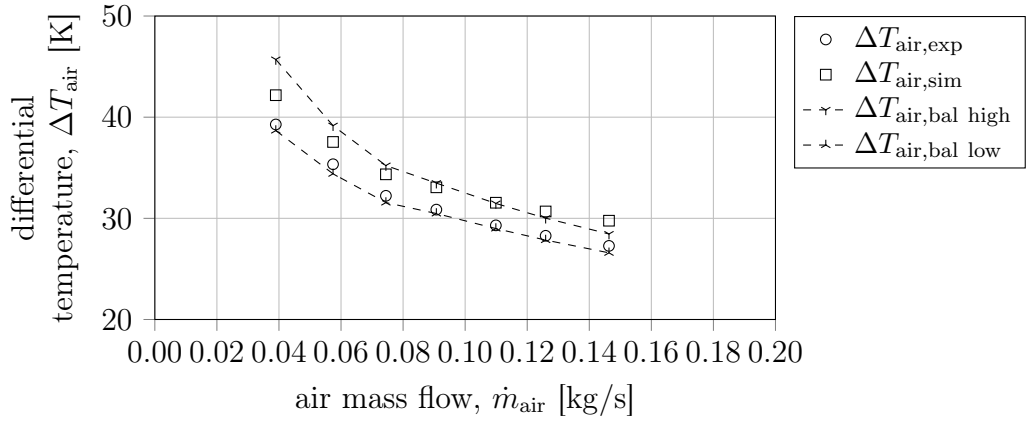

Figure 4.12: Differential temperature between air inlet temperature measurement, $T_{air,in}$, and outlet temperature measurement, $T_{air,out,exp}$, compared to differential temperature simulation at tip, $T_{air,tip,sim}$, and outlet, $T_{air,out,sim}$. The top and bottom line delimit the range between the temperatures increase computed from the energy balance $\Delta T_{air,bal}$.

Stellenbosch University https://scholar.sun.ac.za

Chapter 5

Performance Prediction of the SCRAP Receiver

The performance potential of the SCRAP receiver is established in this chapter. Initially, a single spike is considered, using the reference design, with the goal to vary design parameters to improve understanding on impact of changes on performance. Further, initial conclusions on the performance of a complete SCRAP receiver are drawn.

5.1 Performance of a single spike at reference design

A reference design is provided as a benchmark, using the geometry introduced in chapter 2. Additionally, the nozzle at the spike tip is selected with $d_{\text{nozzle}} = 10\,\text{mm}$ and the flux along the spike is uniform with $60\,\text{kW/m}^2$, which at 4.74 % of the flux on aperture correlates to a value of $1.27\,\text{MW/m}^2$. With an air velocity of $u_{\text{in}} = 10.1\,\text{m/s}$ an air flow rate of $0.0326\,\text{kg/s}$ results. The ambient wind velocity is assumed as $u_\infty = 0\,\text{m/s}$. The resulting reference air outlet temperature is 801 °C. Figure 5.1 illustrates the development of the air temperature as well as the static pressure as the air passes through the spike.

Within the inner tube, the air flow is at a Reynolds number of around 50×10^3. In the rectangular ducts the Reynolds number drops to about 3000.

The pressurized air temperature is increasing from 300 °C at $x = 0\,\text{m}$ to 426 °C when reaching the spike tip. There, the high flux and high heat transfer of the impingement cooling increase the temperature by 89 K to 514 °C. The remaining 287 K are introduced within the rectangular ducts. The significant amount of pre-heating of the air within the inner tube of 126 K is explained by the high temperature of the inner tube wall of between 522 °C and 654 °C, resulting in differential temperature between wall and air flow of $100\,\text{K} \leq \Delta T \leq 355\,\text{K}$. Towards the spike tip a local rise in the inner tube's

Stellenbosch University https://scholar.sun.ac.za

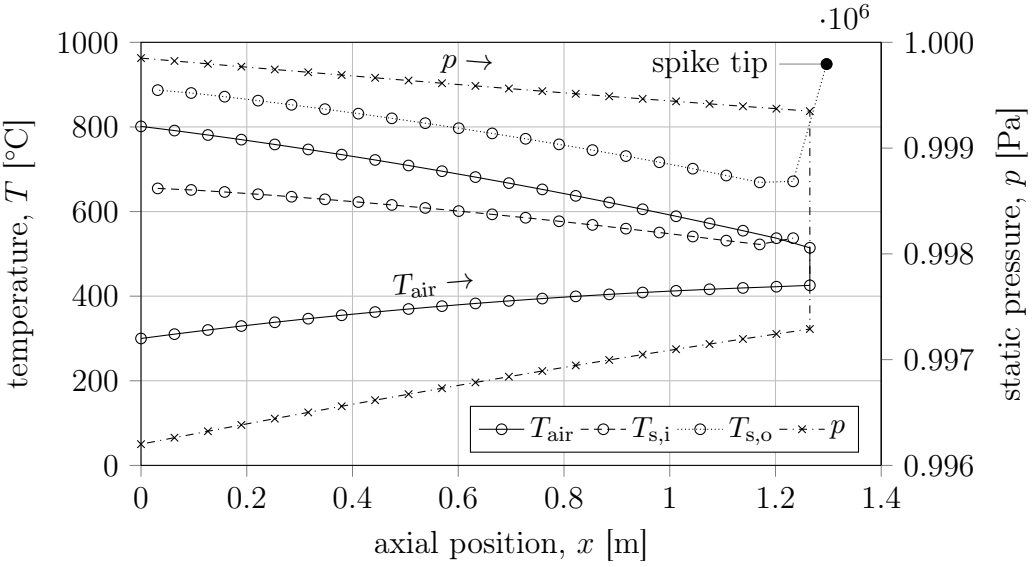

Figure 5.1: Performance characteristic of a spike with reference geometry. Shown are the air temperature, T_{air}, the inner tube's temperature, $T_{\text{s,i}}$, the outer tube's temperature, $T_{\text{s,o}}$, as well as the static pressure, p. The initial 0.6 m of the inner tube passing through the outer chamber are not shown, assuming adiabatic condition through thermal insulation (note inflicted pressure drop, as $p_{x=0}$ is below 1 MPa). T_{air} as well as p are shown for the flow from $x = 0\,\text{m}$ to the tip node at $x = 1.265\,\text{m}$ and then through the internally finned outer tube backwards to $x = 0\,\text{m}$, with $\rightarrow$ indicating the direction of flow.

temperature is attributed to the exposure of the inner tube to radiative heat transfer from the tip.

The outer tube's temperature experiences two peaks, one at the spike tip of $T_{\text{tip}} = 949\,^{\circ}\text{C}$ and one at the spike root of $T_{\text{root}} = 887\,^{\circ}\text{C}$. At the tip, the differential temperature between the metal and the air stream is $\Delta T_{\text{metal,air}} = 523\,\text{K}$ when compared to the air temperature exiting the inner tube. Downstream the spike tip, $\Delta T_{\text{metal,air}}$ drops to 134 K and reaches its lowest point at the spike root — the location experiencing the highest metal temperature — at 86 K.

The drop in static pressure of the air flow over the spike is computed with a total of $\Delta p = 3799\,\text{Pa}$ of which 2056 Pa, or about half, occur over the spike tip. The fins show a stable radial temperature gradient of $49\,\text{K} \leq \Delta T_r \leq 52\,\text{K}$.

Figure 5.2 shows the development of the air density, ρ, as the air temperature, T_{air}, increases. Accordingly, the air velocity, u_{air}, increases with dropping air density. For the shown geometry, the cross sectional area in the inner tube is $531\,\text{mm}^2$, whereas the cross sectional area within the rectangular ducts sums up to $1242\,\text{mm}^2$, resulting in the mentioned notable drop in u_{air} over the spike tip. The heating of the air flow over the tip control volume effects a notable local step in density.

Stellenbosch University https://scholar.sun.ac.za

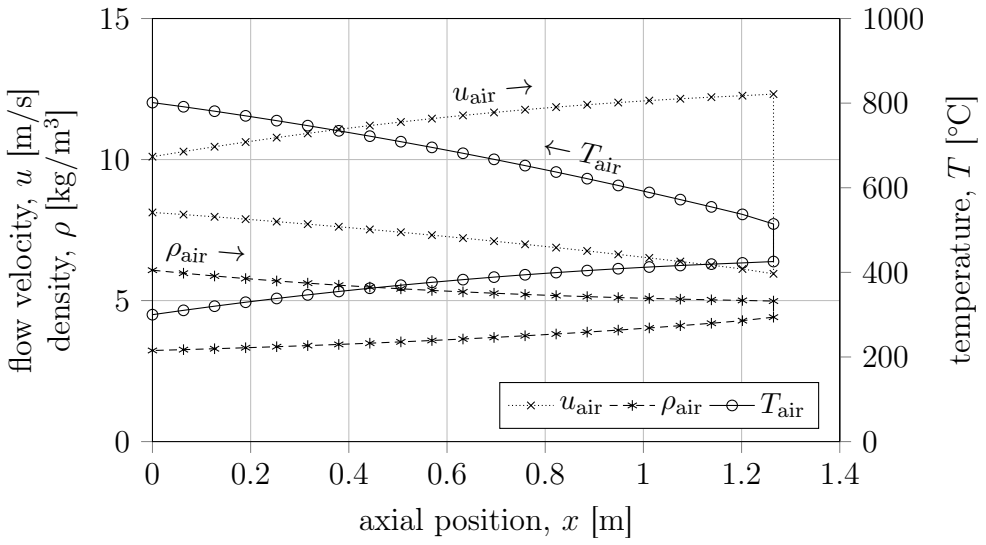

Figure 5.2: Development of air density, ρ, as the air flow is heated as it passes through the spike. The increasing air velocity, u_{air}, as a result of the air expansion can be observed. As the absolute air temperature almost doubles from 573 K to 1074 K it's density drops from 6.08 kg/m^3 to 3.23 kg/m^3. For all curves, $\rightarrow$ indicating the direction of flow

The efficiency of the spike using the reference geometry under a flux on aperture of 1.27 MW/m^2 and zero wind speed is computed as 85.2 %. Of the losses amounting to 14.8 %, radiative heat loss contributes 5.3 %, leaving a remaining 9.5 % of natural convection.

5.2 Sensitivity to wind speed

The performance of a spike of reference geometry is outlined above for zero wind speed. Nonetheless, natural convection contributes to the thermal losses almost twice as much as compared to radiative heat losses. Figure 5.3 illustrates the drop in air outlet temperature, when, under the same mass flow rate and flux, the ambient (cross-)wind speed is increased from $u_\infty = 0$ m/s to $u_\infty = 5$ m/s.

As expected, with a constant mass flow rate, the air outlet temperature drops with increasing wind speeds. At zero ambient wind, the air outlet temperature reaches $T_{\text{air,out}} = 801\,^\circ$C, resulting in a solar-thermal efficiency, η, of 85 %. With increasing wind speeds $T_{\text{air,out}}$ drops, reaching 768 °C at $u_\infty = 5$ m/s. There, η, too, reduces to 79 % (despite significantly reduced surface temperatures).

Stellenbosch University https://scholar.sun.ac.za

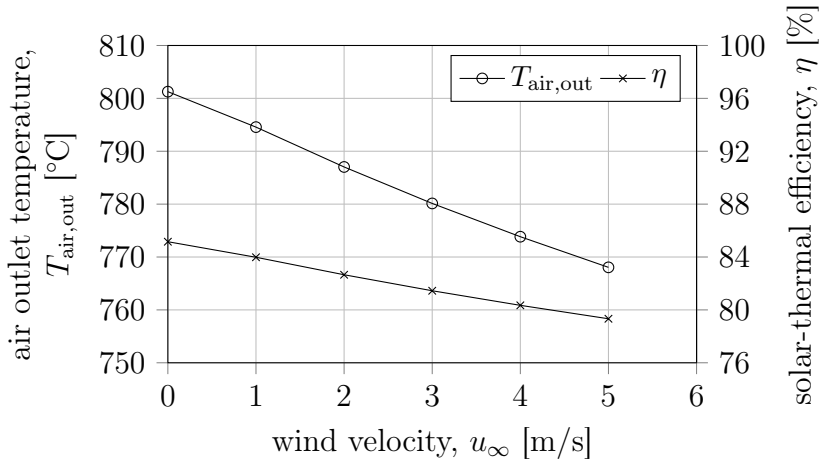

Figure 5.3: Sensitivity of air outlet temperature, $T_{\text{air,out}}$, and solar-thermal efficiency, η, to ambient wind speed, u_∞, at constant mass flow rate, $\dot{m}_{\text{air}}$.

5.3 Sensitivity to flux distribution

The ray-tracing analysis showed that is possible to influence the flux distribution along a spike. The modeling results shown previously assumed a uniform, constant flux of 60 kW/m^2 along the spike. Here, the effect of flux distribution weighing toward the spike tip and towards the spike root are considered. The three profiles compared are illustrated in Figure 5.4.

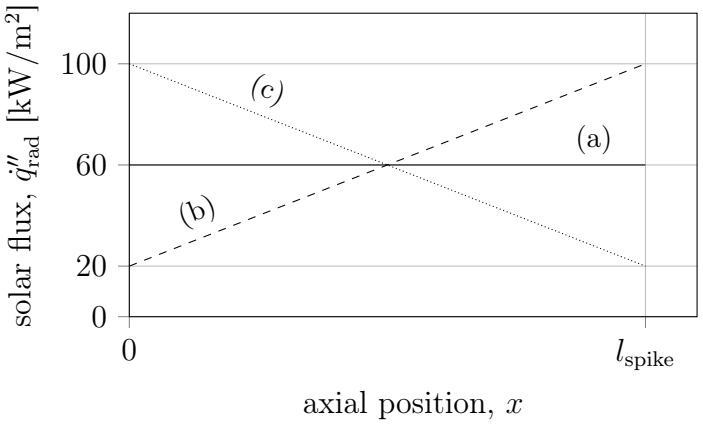

Figure 5.4: Three flux profiles considered: (a) constant uniform flux along x, (b) flux peaking at tip, linear drop to minimum at root and (c) flux peaking at root, linear drop to minimum at tip.

With an ambient wind velocity of 0 m/s the flux profile has limited impact on the spike's performance with $T_{\text{air,out,(a)}} = 801\,°\text{C}$, which reduces to $T_{\text{air,out,(b)}} = 794\,°\text{C}$ for the flux concentrated towards the tip and increases to $T_{\text{air,out,(c)}} =$

Stellenbosch University https://scholar.sun.ac.za

808 °C for flux penetrating deeper into the receiver, towards the root. The temperature profiles of the spike surface as well as the air flow, as it is passing through the rectangular ducts are shown in Figure 5.5.

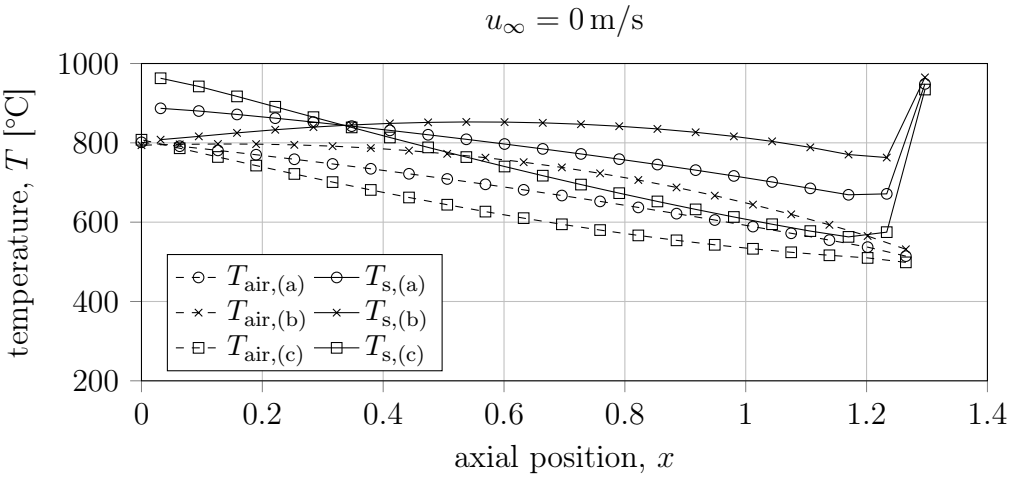

Figure 5.5: Material surface temperature, T_s, and air temperature, T_air, for flux distributions (a), (b) and (c) at $u_\infty = 0\,\mathrm{m/s}$.

While the air outlet temperatures are similar, within $\pm 10\,\mathrm{K}$, it can be seen that the location of peak flux defines the region of strongest heating. With the flux being highest towards the tip (case b), significant differential temperatures between material and air flow of up to 200 K are observed. This leads to locally good heating of the air flow but on the downside to increased temperature in surfaces with high view factor to ambient. The low flux towards the spike root barely balances the heat losses to ambient as well as the inner tube, resulting in about level air temperature.

When selecting a flux profile where the peak is experienced at the spike root (case c), the material temperature towards the exposed tip is notably lower by approximately 200 K when compared to case (b). The material temperature as well as differential temperature to the air stream increase towards the spike root.

With increased ambient air flow, leading to forced convection heat losses, the phenomenon observed in Figure 5.5 is expected to be more pronounced. Figure 5.6 illustrates the same scenario as above, however at an ambient wind velocity of $u_\infty = 3\,\mathrm{m/s}$ (assuming the quadratic wind flow profile along the spike).

With the ambient wind speed of $u_\infty = 3\,\mathrm{m/s}$ the improvement of performance of the case (c) increases, when compared to (a) and (b). For flux profile (a), the air outlet temperature drops by 21 K, for profile (b) by 24 K, while for profile (c) by 19 K.

Stellenbosch University https://scholar.sun.ac.za

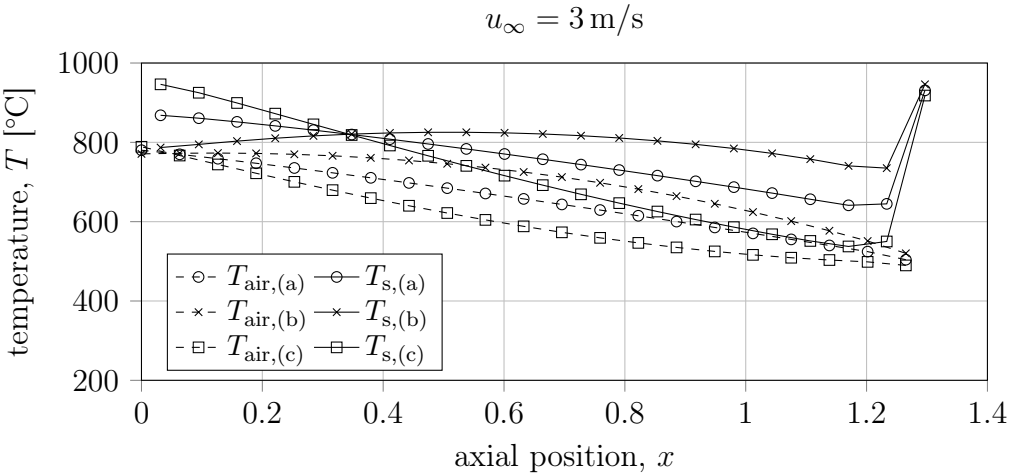

Figure 5.6: Material surface temperature, T_s, and air temperature, T_air, for flux distributions (a), (b) and (c) at $u_\infty = 3\,\mathrm{m/s}$.

For both scenarios, with and without wind, the peak surface temperature for cases (a) and (b) lies at the spike tip. For case (c) the spike tip is approximately 30 K lower, owing to both, lower pre-heating of air in the inner tube as well as improved conductive and radiative cooling effects within the spike. For case (b), the material temperature along the spike reaches its highest point in between tip and root at approximately 850 °C and 826 °C for the cases with wind and without wind, respectively. The peak temperatures are at the root for case (c) at 962 °C and 946 °C, respectively.

In conclusion, a flux distribution weighed towards the spike root improves the thermal performance of the system by increasingly exploiting the volumetric effect, that is, moving peak temperatures to places deep in the structure. There, exposure to forced convection and radiation heat loss is reduced. In consequence, the spike root becomes the location experiencing the hottest metal temperatures.

Stellenbosch University https://scholar.sun.ac.za

5.4 Improvement of design

Chapter 2 provided a reference geometry of a spike as well as the computer model to predict its performance characteristics. Chapter 4 confirmed the validity of the computer model. In the beginning of this chapter, the reference geometry was used to establish a performance baseline. Here, a sensitivity analysis is used to predict potential improvements. The outer dimensions of the investigated spike remain constant to exclude variations in behavior such as convective heat loss or flux distribution. Changes in these require more elaborate models representing these in order to provide reliable data.

5.4.1 Sensitivity of design to internal geometry

A parametric study is conducted with the aim to understand the effect of changes of geometry within a spike. Of interest are the resulting heating of the fluid as well as the pressure drop in the internally finned spike section. The varied geometric parameters are the inner tube's outer diameter, d_{i}, the rectangular duct's width, w, as well as the fin tip's permissible minimal width, $t_{\mathrm{tip,fin}}$. Separately, the nozzle diameter, d_{nozzle} is considered.

Fixed values over all cases are, the spike's length and outer diameter, the inlet air mass flow rate $\dot{m}_{\mathrm{air}}$, as well as the solar flux and ambient conditions.

With changing the internal geometry, the ducts and fins change in geometry and number (e.g. the annular space can accommodate more ducts as they are narrower). Of interest in this section are the abilities to improve heat transfer while at the same time observing the effect on the pressure drop along the ducts. In order to obtain performance data, the spike is irradiated with a constant flux of $60.0\,\mathrm{kW/m^2}$ and exposed to a wind speed of $u_\infty = 0\,\mathrm{m/s}$, the same conditions as applied to analyzing the reference geometry.

The sensitivity of the spike performance to geometry changes is analyzed with considering each geometry from 70 % to 130 % of its design point value. Figure 5.7 illustrates the effect of varying parameters onto the air outlet temperature, T_{air}.

The effect of varying the width of the fin tips on the outlet temperature is marginal, appearing nearly as a horizontal line in Figure 5.7. Smaller fin tips allow for more ducts to be packed into the annular space. The effect of increased surface area is countered by lower heat transfer coefficients due to the resulting lower flow rate as well as reduced heat conduction ability in radial direction of the narrower fins.

Increasing the inner tube's diameter leads to an increase in the air outlet temperature. Owing to a smaller annular space a higher number of shortened rectangular ducts is distributed in the outer tube.

A smaller inner tube diameter leads to a decrease in the number of ducts and as a consequence reduced exposed surface area for heat transfer, and increased hydraulic diameter, d_{hd} (in the rectangular ducts). The largest effect is observed

Stellenbosch University https://scholar.sun.ac.za

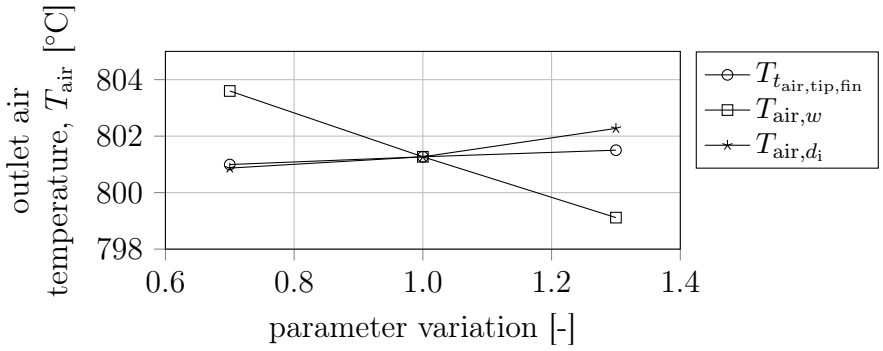

Figure 5.7: Sensitivity of the air outlet temperature T_{air} to variations of inner tube's outer diameter, d_i, the rectangular duct's width, w, as well as the fin tip's permissible minimal width, $t_{tip,fin}$

when varying the duct width w. A narrower duct permits an increased number of channels to fit into the annular space, increasing the surface area, while equally reducing d_{hd}. Despite the increase in the number of ducts the total cross-sectional area is reduced, leading to increased flow velocity, further aiding the heat transfer.

The effect on the peak surface temperature T_s of the spike outer surface, exposed to ambient, is shown in Figure 5.8.

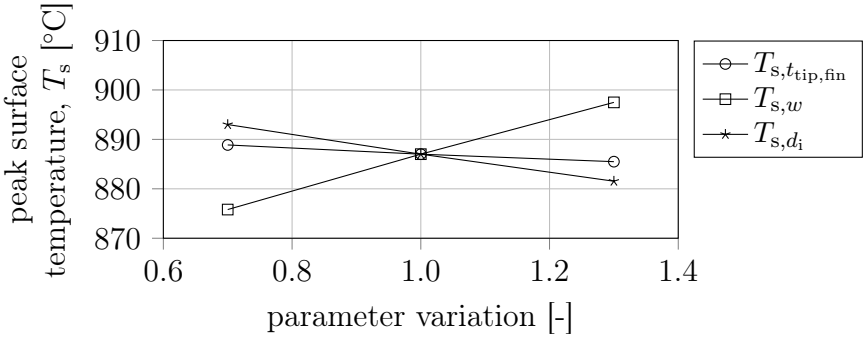

Figure 5.8: Sensitivity of the spike's surface temperature T_s to variations of inner tube's outer diameter, d_i, the rectangular duct's width, w, as well as the fin tip's permissible minimal width, $t_{tip,fin}$

The differences in performance are more pronounced when looking at the material temperature. Here, the changes effect up to above 10 K variations. Naturally the pattern in Figure 5.8 is the opposite of the trends indicated in Figure 5.7, as heat not transferred into the air-stream, raising the air outlet temperature must be lost to ambient. This effect can be observed when analyzing the heat loss to ambient as shown in Figure 5.9.

Stellenbosch University https://scholar.sun.ac.za

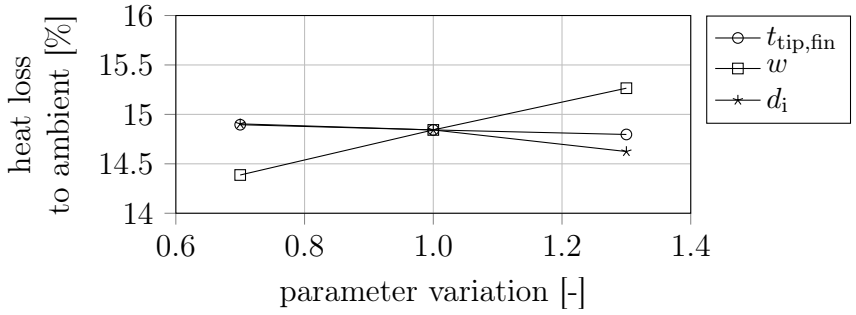

Figure 5.9: Sensitivity of the spike's heat loss to ambient to variations of inner tube's outer diameter, d_{i}, the rectangular duct's width, w, as well as the fin tip's permissible minimal width, $t_{\mathrm{tip,fin}}$

It can be seen from Figure 5.9 that, under the investigated conditions, reducing the surface temperature of the spike by about 20 K translates to a performance gain of approximately 1 %. The variations in internal geometry affect the flow cross-sectional area as well as duct shape, consequently varying the pressure drop. Figure 5.10 shows the pressure drop for the same set of variations.

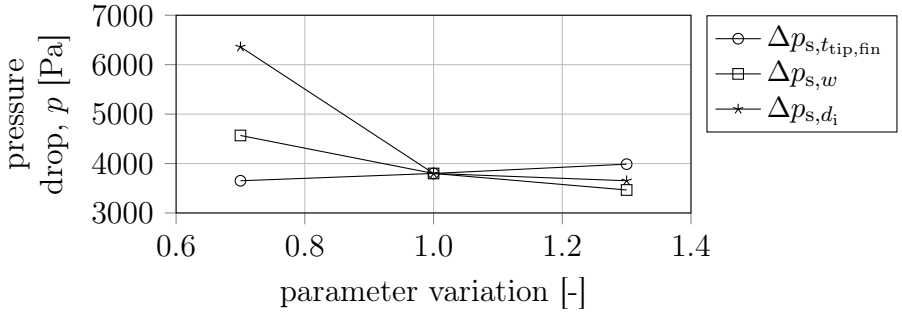

Figure 5.10: Sensitivity of the pressure to ambient to variations of inner tube's outer diameter, d_{i}, the rectangular duct's width, w, as well as the fin tip's permissible minimal width, $t_{\mathrm{tip,fin}}$.

Figure 5.10 demonstrates that improving heat transfer characteristics has varying cost attached in form of pressure drop. It appears that increasing the inner tube's diameter not only results in improved heat transfer characteristics but also contributes to a reduced pressure drop. The 30 % reduced d_{i} shows strongly increased pressure drop due to the increased flow velocity in the smaller inner tube. Reducing w results in increased pressure drop as the flow's cross sectional is reduced and the air flow velocity increased.

A narrower fin tip width, as shown earlier, does not lead to notable contribution in heat transfer enhancement, does, however, show influence on the

Stellenbosch University https://scholar.sun.ac.za

pressure drop, with a narrower fin tip reducing the pressure drop by almost 10 %, when comparing the 130 % tip width to the 70 % tip width.

5.4.2 Sensitivity of design to nozzle design

The nozzle at the spike tip defines the jet impinging on the tip. Sufficient cooling needs to be generated by the impinging jet in order to enable the system to operate at high concentrated solar flux levels. With the tip being exposed to ambient, a consequence of high tip temperatures is the radiative heat loss. Smaller nozzles provide higher *Re* jets, increasing the heat transfer capabilities. The downside is the increased pressure drop. This analysis discusses the sensitivity of the spike's performance taking thermal losses and pressure drop into consideration. Nozzles from $d_{\text{nozzle}} = 5\,\text{mm}$ to $d_{\text{nozzle}} = 26\,\text{mm}$ (which represents no nozzle for the reference geometry) are considered.

All data presented is for a spike of reference geometry and conditions. The air mass flow rate was held constant at $\dot{m}_{\text{air}} = 0.0326\,\text{kg/s}$. Figure 5.11 illustrates the effect of changing d_{nozzle} onto the air outlet temperature,$T_{\text{air,out}}$, as well as the spike tip temperature, T_{tip}.

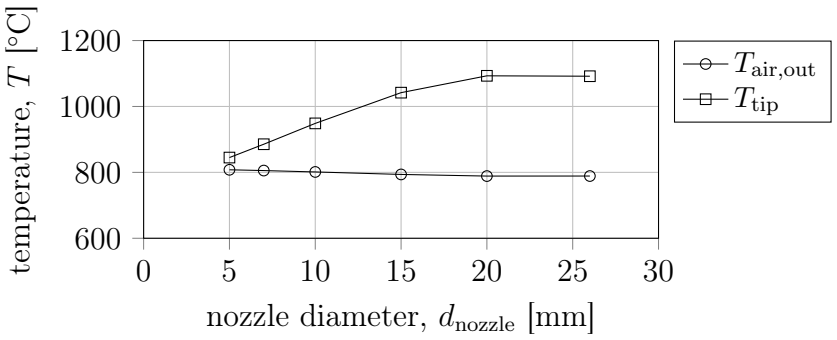

Figure 5.11: The effect of the nozzle diameter, d_{nozzle} onto the air outlet temperature, $T_{\text{air,out}}$, as well as the spike tip temperature, T_{tip}.

It can be observed that decreasing nozzle diameters result in drastically falling spike tip temperatures, T_{tip}. As a consequence the air outlet temperature, $T_{\text{air,out}}$, increases slightly, due to the increased amount of heat passed onto the air stream when impinging onto the spike tip. Figure 5.12 illustrates the correlating total pressure drop, Δp_{spike}, of the air flow passing through the spike. With remaining geometry being identical, the differences in Δp_{spike} are attributed to the tip (when neglecting minor impact of different air temperature on flow velocity). Also shown is the radiative heat heat loss of the investigated spike to ambient as a fraction of the absorbed solar radiation, $\dot{Q}_{\text{rad,loss}}/\dot{Q}_{\text{in}}$.

As expected from Figure 5.11, the falling spike tip temperature results in a reduction of radiative heat loss to ambient. It is notable that the improvement on heat loss abates towards smaller nozzle diameters, attributed to the spike

Stellenbosch University https://scholar.sun.ac.za

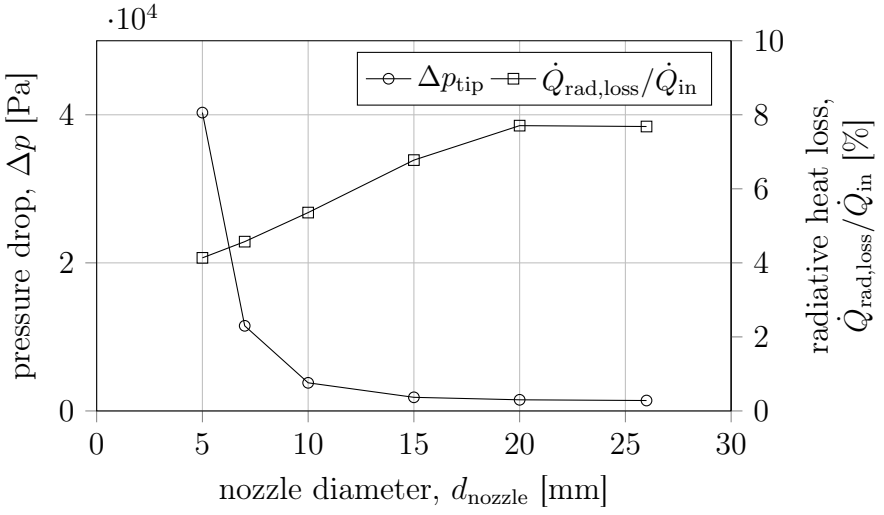

Figure 5.12: The effect of the nozzle diameter, d_{nozzle} onto the pressure drop over the nozzle as well as the turn in flow direction by 180°. radiative heat loss of the investigated spike to ambient, $\dot{Q}_{\text{rad,loss}}/\dot{Q}_{\text{rad,abs}}$.

tip not being the sole contributor to radiative heat loss. It can, however, be noted that the spike tip performance is dominant on the radiative heat loss of a spike.

The pressure drop, combined over the nozzle as well as the change in flow direction, for large nozzle diameters is negligible with about 113 Pa for a nozzle of 26 mm diameter (= no nozzle). With reducing nozzle diameters the pressure drop increases drastically. At $d_{\text{nozzle}} = 10\,\text{mm}$ the pressure drop amounts to 2.5 kPa, increasing to 10 kPa for $d_{\text{nozzle}} = 7\,\text{mm}$ and further to 39 kPa for $d_{\text{nozzle}} = 5\,\text{mm}$.

5.4.3 Improvement potential of design

Based on the observations made in the parametric study an improved design is selected. This design is aimed to show the potential with which the performance can be improved, rather than attempting identification of an optimal geometry.

A suitable improved design of the spike is dependent on a number boundary conditions. One such limitation is the permissible minimal width t of the fin tips. The fin tips must permit a reliable manufacturing process as well as over the lifetime of the receiver withstand the inner tube resting on them as well as sliding over them due to thermal expansion. A minimal fin tip width of 1.0 mm is set as a boundary to satisfy such needs. Detailed analysis of manufacturing processes as well as mechanical loads and effects of a life-time operations may permit refining this boundary in future. The duct width is bound to a minimum width of 2.0 mm as a safe guard to omit risk of blocking of the air passages through particles or fouling over the years. To improve performance a nozzle of $d_{\text{nozzle}} = 7\,\text{mm}$ is selected.

Stellenbosch University https://scholar.sun.ac.za

Using the two proposed bounding values as given, the largest $d_\mathrm{i} = 19.5\,\mathrm{mm}$ of the parametric study is selected. The air flow rate is adjusted to again achieve the target air outlet temperature of 800 °C. The air mass flow rate is increased to $\dot{m}_\mathrm{air} = 0.0352\,\mathrm{m/s}$ (from $0.0326\,\mathrm{kg/s}$). Due to increased flow rate as well as the reduced nozzle size, the pressure drop increases from 3.8 kPa to 12.6 kPa (of which 10.8 kPa are attributed to the spike tip, meaning that increased air flow rate and adapted geometry result in a modest increase of 402 Pa). Figure 5.13 shows the air temperature as well as the temperatures of the inner and outer tube material.

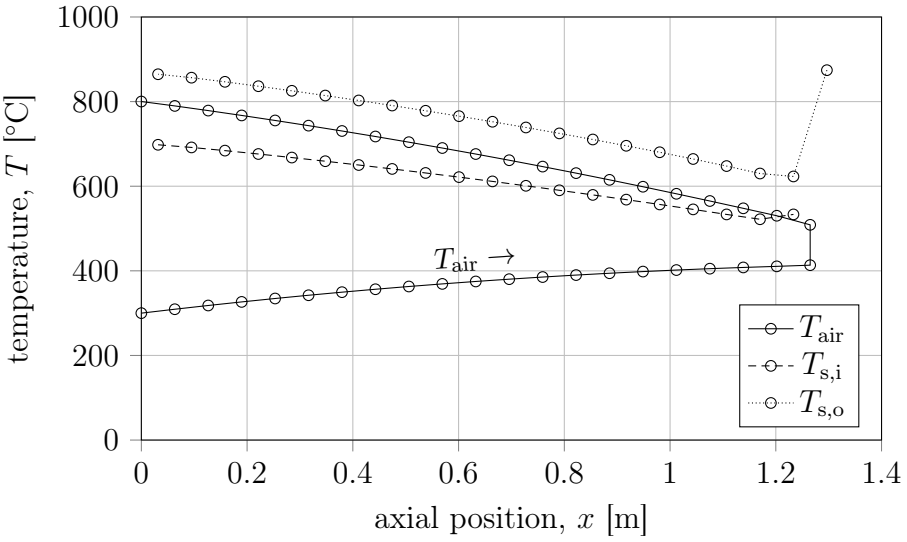

Figure 5.13: Performance characteristic of a spike with improved geometry. Shown are the air temperature, T_air, the inner tube's temperature, $T_\mathrm{s,i}$, and the outer tube's temperature, $T_\mathrm{s,o}$.

Comparing Figure 5.13 to Figure 5.1 it is noted that the surface temperatures are lower for the improved design, leading to reduced heat losses. The peak material temperatures are reduced from $T_\mathrm{tip,reference} = 949\,°\mathrm{C}$ and $T_\mathrm{root,reference} = 887\,°\mathrm{C}$ to $T_\mathrm{tip} = 874\,°\mathrm{C}$ and $T_\mathrm{root} = 864\,°\mathrm{C}$. The reduced surface temperature also shows in lower differential temperature between the metal and the air flow of between 92 K near the tip and 65 K at the spike root.

The calculated solar-thermal efficiency is $\eta = 86.7\,\%$, of which the radiative heat loss amounts to 4.2 % and the natural convection to 9.1 %, showing an overall improvement of 1.5 % when compared to the reference geometry.

5.5 System pressure drop

The pressure drop over the spike with the reference geometry is computed with 3799 Pa. This must be considered in the context of a system pressure drop

Stellenbosch University https://scholar.sun.ac.za

analysis where air flow from a compressor up a tower and back to the turbine is taken into account. The pressure drop of such a system is largely dependent on sizing of the ducts employed. In Appendix R a pressure drop analysis for the central receiver system introduced in chapter 2 is conducted. A system with a pipe diameter of $d = 1.0\,\mathrm{m}$ showed a total pressure drop of 7957 Pa, out of which 3799 Pa are attributed to the spike model. Increasing the pipe diameter to $d = 2.0\,\mathrm{m}$ results in a reduction in system pressure drop to 4027 Pa.

Any optimization of such a system is dependent on cost of pressure and temperature resistant ducting and thermal insulation thereof, countered by the drop in gas turbine efficiency due to system pressure drop. The pressure drop of 4 kPa – 8 kPa compares favorably to the assumed operating pressure level of $p = 1\,\mathrm{MPa}$. The improved design outlined above, featuring a pressure drop of 12.6 kPa leads to a total receiver system pressure drop of 12.8 kPa to 16.8 kPa (128 mbar to 168 mbar). Predominantly, with higher spike pressure drop, the contribution of the CSP plant components to the system pressure drop seem to become less significant.

The SCRAP's modeled pressure drop appears to be within international benchmark, when compared to available information on alternative receiver technologies, such as the SOLGATE multi-tube coil receiver, reported at 120 mbar pressure drop (Solgate Report, 2005). The analysis shows that the choice of internal geometry impacts the pressure drop, permitting design of spikes in accordance to a pressure drop as boundary condition.

5.6 Summary

The solar-thermal performance of a spike and the SCRAP receiver was analyzed under an averaged surface flux of $\dot{q}''_{\mathrm{rad}} = 60\,\mathrm{kW/m^2}$, representing a flux on aperture of $1.27\,\mathrm{MW/m^2}$. The SCRAP receiver showed to be able to remove the thermal energy it is exposed to. The two areas of peak metal temperature are the spike root as well as the spike tip. Which of the two is experiencing higher temperature depends on design as well as flux assumptions.

The particular geometry considered would be less suitable for operation under lower flux, should the target outlet air temperature of 800 °C be desired. This is due to the observation that lower flow rates lead to the possibility of the air flow in the rectangular ducts (at least partially) dropping into the laminar flow regime. The drop in the Nusselt number from turbulent flow in the low turbulent Reynolds numbers into these of laminar flow is not necessarily large, as the geometry of the narrow rectangular ducts results in good heat transfer coefficients (see chapter 2 and appendix F). However, effects of stratification should be considered before making conclusive remarks on operation in the laminar regime.

Adapting internal geometry permits increasing of the thermal performance, while maintaining low pressure drops. Further increase is possible, depending

Stellenbosch University https://scholar.sun.ac.za

on the assumption for permissible pressure drop.

Depending on geometry selected and assumptions made, a volumetric effect is partially achieved. The spike tips, the most exposed part of the structure may experience the highest surface temperatures. On the other hand, the majority of the surface is within the structure and experiences low view factors and wind protection. The hottest section of the spike itself is expected to occur towards the root.

The receiver appears to favor flux penetrating deeper into the structure to increase solar-thermal performance. However, it needs to be noted that the Nusselt number equation used does not provide a local Nusselt number, underestimating the peak in heat transfer, as the air flow enters the rectangular ducts. Such effects should improve the performance of the spike, in particular with higher flux towards the tip.

The receiver shows vulnerability towards ambient wind, resulting in a notable drop in performance even at lower wind speeds.

Stellenbosch University https://scholar.sun.ac.za

Chapter 6

Conclusion

The SCRAP receiver concept is a suitable technology to pre-heat pressurized air as a heat transfer fluid for a concentrating solar power plant.

6.1 Contribution

The first objective was to develop an understanding of spatial distribution of concentrated solar flux on the SCRAP receiver. Chapter 2 discusses the ray-tracing model employed to simulate sun rays, reflected via a heliostat field, impinging on the absorber surfaces of the receiver. A simplified design case was developed and it was found that the spatial distribution of flux on the absorbers is influenced by the heliostat, with smaller heliostats resulting in reflected sun rays tending to penetrate deeper into the structure, whereas larger heliostats resulting in increased flux towards the outer, exposed part of the receiver.

The ability to cool the high flux experienced at the spike tip by means of jet impingement cooling was analyzed in Chapter 2 by developing a CFD model of the spike tip region. The model showed that without a nozzle the jet resulted in insufficient cooling averaged over the tip as well as a large stagnation area at the center, which would result in the location being exposed to the highest solar flux being at risk of insufficient cooling. Analysis employing various nozzle diameters in order to increase the jet velocity showed that the peak heat transfer increases and shifts towards the center point with decreasing nozzle diameters. It was shown that sufficient cooling over the spike tip can be obtained, using jet impingement as local heat transfer enhancement.

The sensitivity of the receiver performance to changes of internal geometric parameters within a spike was investigated in Chapter 5. Here, the diameter of the inner tube, d_{i}, the width of the rectangular ducts, w, as well as the width of the fin tips, $t_{\mathrm{tip,fin}}$, were varied from 70 % to 130 % in a parametric study. It was shown that the heat transfer can be improved when comparing to the reference scenario, resulting in improved solar-thermal efficiency as well as

Stellenbosch University https://scholar.sun.ac.za

reduced differential temperature between the spike material and the pressurized air, which could be reduced from 134 K to 92 K at the highest point towards the spike tip and from 86 K to 65 K at the lowest point at the spike root. The dominant limitation in the performance improvement is the resulting pressure drop. The pressure drop of the air flow passing through a spike in the reference geometry was predicted with 3799 Pa, of which about half is attributed to the impingement jet cooling at the spike tip. The pressure drop, and as a consequence, spike performance can be adjusted, according to the permissible pressure drop as boundary condition provided by a Brayton cycle design.

At a ambient wind velocity, u_∞, of 0 m/s, the solar-thermal efficiency was modeled with 86.7 % for an improved design, based on the findings of the parametric study. Susceptibility of the performance to ambient wind conditions is noted, where a wind velocity of 5 m/s leads to an increase in convective heat losses from 9.5 % to 15.9 %, while at the same time causing the outlet air temperature to drop by 33 K, when holding the air flow rate constant. The large convective heat losses are attributed to the large, exposed surface area. The low radiative heat losses of about 4 % for the improved design indicates that the volumetric effect on macro scale can be achieved. Figure 5.1 shows that the two hottest spots are the spike tip as well as the root of the spike. Compared to the total surface of a spike, the tip is of relatively small surface area (even though fully exposed to ambient), resulting in low view factors of the majority of the hot surface to ambient.

Compared to alternative proposed concepts for pre-heating of pressurized air, the SCRAP receiver shows competitive performance. The solar-thermal performance can exceed the performance delivered to date, typically being limited to about 80 %. At the same time, the receiver is not limited to either the utilization of polar solar field layouts, nor the inherent optical losses when employing cavity receivers.

Stellenbosch University https://scholar.sun.ac.za

6.2 Further work

This research undertaking has provided a foundation to justify further work on the SCRAP receiver concept. A number of suitable steps are briefly outlined to carry research on the receiver forward.

6.2.1 Testing of a spike cluster on sun

A cluster of spikes, which at minimum could be a spike with a set of surrounding spikes, should be manufactured from an alloy suitable for high temperature application (e.g. Inconel) for the purpose of being experimentally tested on concentrated sunlight or in a solar simulator.

6.2.2 Simulation of performance under realistic operating conditions

The design point scenario employed in this research neglects two phenomena a real SCRAP receiver would likely be exposed to. Around a spike the flux is unlikely to be uniform, circumferentially. Research is required to predict to what magnitude a discrepancy in circumferential flux may occur. This understanding leads to the ability to analyze the effect on the air flow patterns within a spike, and understanding the risk of choking of a spike. This would be a scenario where a high flux exposed section leads to high heating of the air flow, thus, increasing the pressure drop in that duct(s). A runaway problem occurs where air then increasingly passes through low flux passages, permitting a hot side to further overheat.

In a more global perspective a similar question needs to be answered when considering spikes on various sides of a receiver, experiencing not necessarily similar flux levels.

6.2.3 Interaction with ambient

The SCRAP receiver is shown to be sensitive to convective heat loss. A SCRAP receiver, exposed to wind, would by its geometric nature shield itself from wind passing through, as the spikes form a labyrinth for the air flow. To what extent this assumption is applicable can be analyzed in a dedicated research project.

Hinging on this adiabatic analysis can be developed another set of answers with regards to the question whether natural convection from a larger SCRAP receiver could induce, through buoyancy effects, a constant forced convection, even at $u_\infty = 0\,\mathrm{m/s}$.

The modeled heat losses assumed an air temperature of $T_{\mathrm{ambient}} = T_\infty$. Naturally, with closely packed spikes, heating of the air through natural and forced convection should increase T_{ambient} and consequently reduce convective heat losses below modeled values.

Stellenbosch University https://scholar.sun.ac.za

6.2.4 Helically swirled fins

A concept to improve the heat transfer characteristics of a spike is — instead of straight fins as analyzed here — using helically swirled fins. This has two useful effects. Firstly, the heat transfer is expected to be improved by inducing secondary flow patterns into the air flow.

Secondly, the helical shape permits each air stream to pass circumferential positions multiple times, countering effects of non-uniform flux distribution. This is expected to reduce the risk of chocking (as outlined above) as well as result in more uniform air heating, besides increased thermal efficiency

6.2.5 Impingement jet cooling

For the purpose of this analysis the spike tip was modeled in a minimalistic fashion as a single node in the heat transfer model. A detailed CFD study is expected to assist in accurately predicting heat transfer capabilities of an impinging jet as well as the accompanying pressure drop. Furthermore, such an analysis can be used to identify suitable geometry for the tip region to enhance heat transfer/reduce pressure drop.

6.2.6 Material considerations and manufacturing

The FEM analysis has shown that stress due to pressurizing the system can be reduced by adjusting the design. Further consideration to stress under operating conditions is required. The ability to perform rapid start up times is relevant for receiver technologies and material stress under transient conditions tend to limit such.

The prototype was manufactured using wire cutting which is not a suitable process for large scale manufacturing due to cost as well as limitations in specimen dimensions. Other manufacturing processes have been tested or discussed and further work is needed to identify a solution, assuming large scale roll out.

Stellenbosch University https://scholar.sun.ac.za

Appendices

Stellenbosch University https://scholar.sun.ac.za

Stellenbosch University https://scholar.sun.ac.za

Appendix A

Central Receiver Tower Height

Optimization of an entire CSP plant utilizing the SCRAP receiver is outside the scope of this work. The tower height for the simulation is based on a comparison of average tower heights of constructed CSP systems. Figure A.1 shows the tower height for a number of smaller plants with available data. It has to be noted that at times it is not clear if the provided height is the tower height, or the receiver height. For the scope of this investigation the effect is seen as insignificant. The outcome is a representative tower height to get a realistic model for the ray-tracing application.

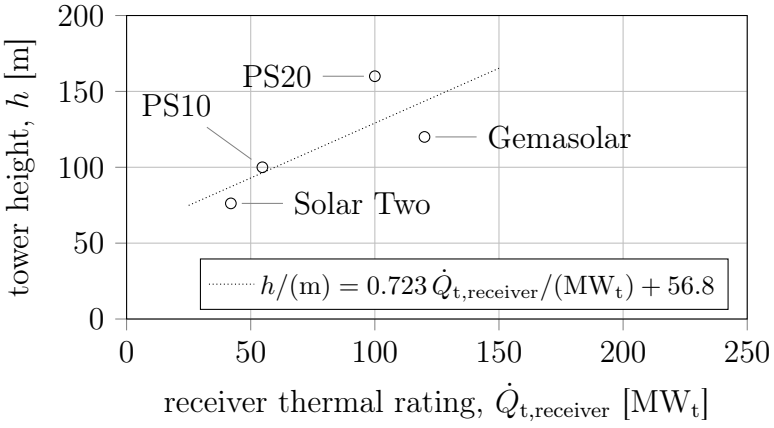

Figure A.1: Tower height h of central receiver plants over the receiver thermal rating $\dot{Q}_{\mathrm{t,receiver}}$ for relatively small CSP plants

The central receiver systems shown in Figure A.1 contains systems with polar fields (PS10 and PS20) as well as systems with surrounding fields (Solar Two and Gemasolar). A SCRAP receiver of 35 $\mathrm{MW_t}$ receiver capacity is further assumed to have tower height of 82 m, which lies on a linear curve fit through the data points of Figure A.1.

Stellenbosch University https://scholar.sun.ac.za

Stellenbosch University https://scholar.sun.ac.za

Appendix B

Validation of Tonatiuh Ray-Tracing Software

B.1 Selection of a ray-tracing software

Several programs have been developed with the purpose of simulating the optical aspects of CSP plants. Of the codes with ray-tracing capability only NREL's SolTrace and CENER's Tonatiuh are available free of charge (Bode and Gauché, 2012). Software developed with the application in the optical industry seems not to be directly usable to simulate complex systems using the sun's light (Wendelin *et al.*, 2013).

As opposed to SolTrace, Tonatiuh provides a visualization of the simulated optical system configuration. This directly enables the user to visually inspect the configured geometry, thereby eliminating an error source for ray-tracing simulations[1].

A more important factor is that SolTrace has shown to be unstable when simulating a high number of rays. Stability issues in running SolTrace with a large number of rays were reported amongst others by Blanco *et al.* (2009). Simulating a heliostat field and a complex three dimensional target requires a large number of rays to obtain results of good quality: Blanco *et al.* reported stability issues in the range of 2.5×10^6 rays, while SCRAP simulations are operated between 50×10^6 rays and 500×10^6 rays, owing to the geometric complexity.

Tonatiuh provides results of similar quality to the more established SolTrace, judging from comparisons between the two ray-tracers (see section B.2). Hence, Tonatiuh is selected over SolTrace for its stability and GUI advantages.

[1]Ray-tracing software typically requires components to be defined within individual coordinate systems. A receiver assembly is achieved by positioning components relative to one another. This leads to complicated cascaded coordinate systems. Visual inspection is helpful in the initial stage to confirm correct angle calculations.

Stellenbosch University https://scholar.sun.ac.za

B.2 Validation of Tonatiuh by developers

Blanco *et al.* (2009) compared the results of the software to the SolTrace counterpart. Simplified versions of the EuroDish a LS3 parabolic trough collector and the NREL solar furnace are simulated. The results for the solar furnace and the LS3 parabolic trough collector are in very good agreement. The EuroDish simulation led to a maximum error in calculated flux of 3 %, the largest deviation of the investigated concentrators. Errors for total impinging solar power on target and distribution of hit points were lower. It has to be noted that Blanco *et al.* only operated simulations with up to 2.5×10^6 rays due to stability issues with SolTrace.

Blanco *et al.* further used data of the French CNRS-PROMES central receiver facility THEMIS to further validate the software. This validation was not aimed at investigation of a multi-reflection system like the kind of Blanco *et al.* in (2010). In this work the authors compared the images cast by different facets (for ideal facet canting and actual facet canting) of a single heliostat to the real image, recorded with a camera system. As a result Blanco *et al.* (2011) state a maximum deviation in flux distribution of 3.6 % from the simulated to the real image. The simulations were limited to canting errors only and the authors expected further improvement with the incorporation of heliostat facet surface errors.

Mutuberria *et al.* (2012) expanded the work on the CNRS-PROMES facility in an attempt to establish the effect of gravity on the heliostat shape and the resulting image. All facets of a heliostat were measured for different elevation angles, using a photogrammetry technique. The images of the real heliostat were reproduced in Tonatiuh, using the measured actual heliostat shape. Tonatiuh showed accurate reproduction of the images, suggesting that the investigated photogrammetry approach provides useful results.

Further, a new ray-tracer named Solfast is under development by CNRS-PROMES researchers. To validate their work, a comparison between Tonatiuh, SolTrace and Solfast simulation results was provided (Roccia *et al.*, 2012). They compared the results of the three ray-tracers for the THEMIS central receiver facility. The three programs were in good agreement with their results for the flux on the receiver target. However, more detailed analysis of the accuracy than plots was not provided. Further, Solfast showed good agreement with Tonatiuh for the EuroDish and good agreement with SolTrace for the LS2 parabolic trough collector.

The Tonatiuh ray-tracer shows good agreement with other ray-tracing software and in the (limited) validation with test data. For the purpose of this investigation, to develop an understanding for the flux distribution and to investigate sensitivities, the confidence in accuracy of the results is seen as sufficient.

Stellenbosch University https://scholar.sun.ac.za

B.3 Validation of Tonatiuh against reproduceable problems

With the general applicability of the Tonatiuh ray-tracer extracted from literature, the author has performed a number of ray-tracing simulations on problems reproduceable with basic analytical solutions. These are to confirm correct application of the ray-tracer as well as understanding the functionality of reflection. This analysis is further of importance as Tonatiuh is little documented and the full functionality of reflection requires analysis.

B.3.1 Multiple reflection

Reproducing a scenario with multiple reflections of rays is relevant to understand the effect of complex geometries, such as the SCRAP receiver, onto the flux on its surface(s). A simple case with multiple mirrors reflecting rays is illustrated in Figure B.1.

In Tonatiuh, the user specifies a DNI when configuring a simulation. Tonatiuh automatically assigns each ray the same photon power, depending on the number of rays generated, so that the total sum of rays represents the defined DNI. When a ray strikes a surface of a 10 % reflectivity, consequently every 10th ray (on average) is reflected from the surface. This reflected ray maintains its assigned power. However, the software counts all ray hit points, including those of rays that are further reflected. In a simple example, a mirror with 100 % reflectivity directs beams onto a target with 100 % absorption. As a result 200 % of total hit-points are counted.

To correct for that effect and maintain the energy balance, the user can omit (remove) previous hit-points of reflected rays in order to maintain a total energy balance. Alternatively, one can count all hit points but during post-processing needs to manipulate (reduce) the photon power for each surface, according to the reflectance settings.

The latter approach has two significant advantages. Firstly, when reducing the photon power the number of counted hit-points on each surface is higher, leading to a more rapid convergence of the results. Secondly, it is computationally expensive to follow and store the path of all rays through a complicated geometry such as the SCRAP receiver to establish their amount of reflections. Tonatiuh can provide an output file for selected geometries or all geometries. For a large amount of rays, the output files reach multiple megabyte of size for a single SCRAP spike. It is thus impractical to follow all rays or even a cluster of neighboring spikes to establish paths of rays.

The procedure applied in post-processing (also in simulation of the SCRAP receiver) was to multiply photon power for a surface by $(1 - \rho)$, where ρ is the surface's reflectance, correcting for the power contained in the reflected rays.

Stellenbosch University https://scholar.sun.ac.za

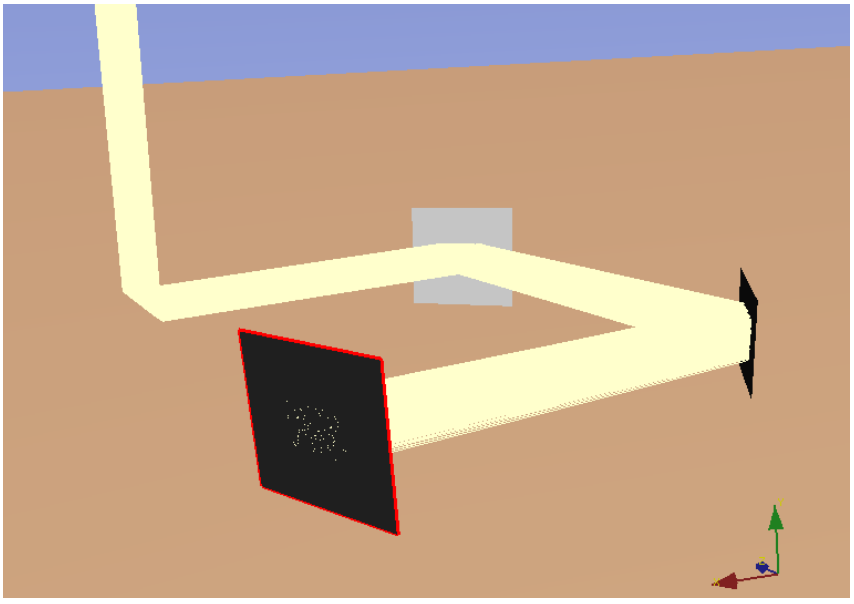

Figure B.1: Visualization of a test setup with a series of three mirrors reflecting rays onto a target (red frame).

B.3.2 Reflection of light onto a cylinder

Another test to validate the correctness of a configuration is to simulate a simple setup where a single mirror reflects solar beams onto a single cylindrical target as shown in Figure B.2.

In the simulated case, the mirror is angled at 22.5° to reflect the rays onto the center point of a cylindrical tube. From the center point the tube is extruded to a length of 13 m. The remaining measurements are a heliostat size of 10 m × 10 m and a distance from the origin of the cylinder to the center point of the heliostat of 50 m in horizontal as well as vertical direction. The cylinder's radius is 0.35 m. Reflectivity of the mirror is selected with 100 % and the absorptivity of the tube is set with 100 %.

The resulting flux on the cylinder cap of the single heliostat at a DNI of 1000 kW/m^2 is 0.703 kW/m^2. A geometric calculation of the cosine effect confirms this with an expected flux of 0.707 kW/m^2. As the rays from the heliostat impinge on the cylinder at an angle of 45°, consequently the same flux is expected for the bottom of the cylinder surface. This is confirmed by Figure B.3, illustrating the flux along the irradiated bottom of the cylinder. It has to be noted that the cylinder surface was meshed in the post-processing process (as illustrated in Figure 2.5) and a cell covers an angle of 20° in the given case (due to the mesh configuration the bottom line is actually the average of the first cell in each direction, as these expand from 0° to ±20°). Thus a slight drop in flux for a mesh cell is expected and the flux of around 0.703 kW/m^2 is not reached.

A further observation in Figure B.3 is a drop in flux to zero at about the

Stellenbosch University https://scholar.sun.ac.za

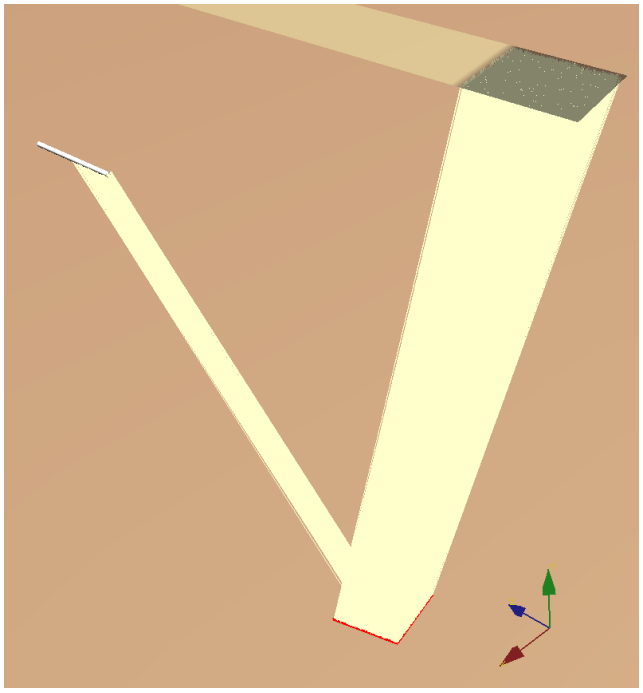

Figure B.2: Visualization of a test setup with a mirror reflecting rays onto a cylindrical absorber (missing rays (spillage) are not visualized).

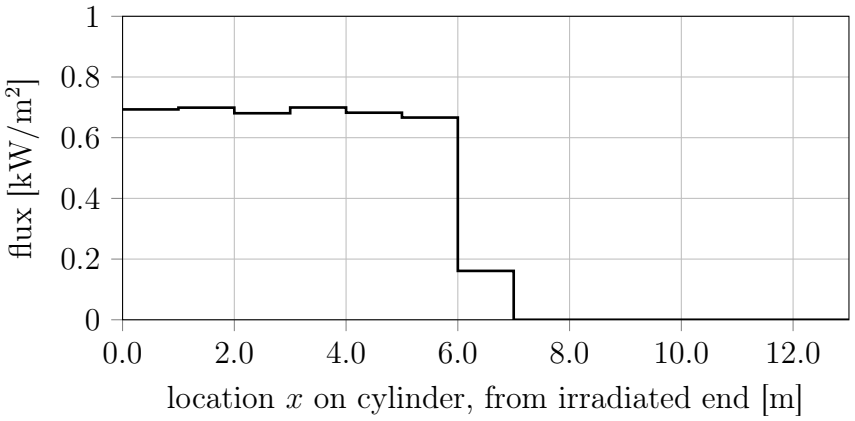

Figure B.3: Flux along the irradiated bottom of the cylinder, where 0 m is the irradiated end of the body

7 m mark, where the heliostat's reflection does not further reach the cylinder surface. A simplified geometrical model estimates 6.18 m without, or 6.66 m, when including the sun half-angle for the furthest rays to strike the cylinder. This confirms Figure B.3, where each data point represents a rectangular cylinder surface element of 1 m length. The data point at meter 6.5 thus represents ray hit points between meter 6 and meter 7. Consequently it is in agreement with the theoretically derived values above, that the 7.5 m data

Stellenbosch University https://scholar.sun.ac.za

point is of value zero.

A three dimensional plot of the flux on the mesh representing the cylinder surface is illustrated in Figure B.4.

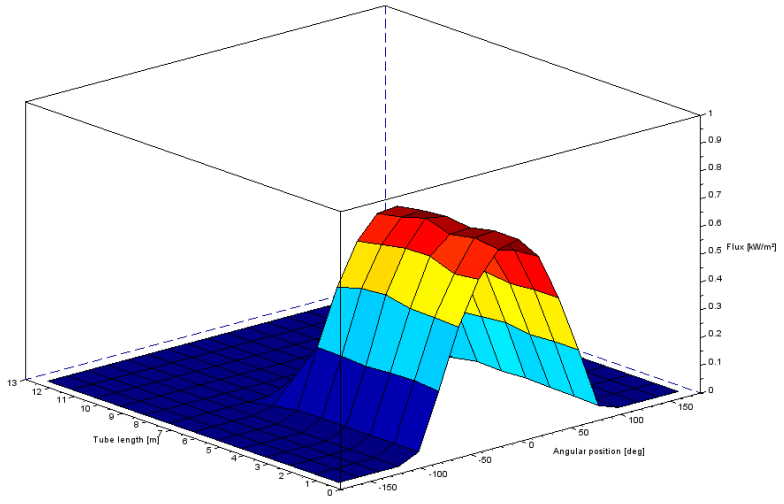

Figure B.4: Flux on the cylinder surface (0° equals to bottom side of the cylinder)

It can be seen that the magnitude of the flux around the circumference of the cylindrical absorber is representing an expected shape of a cosine curve. The imping flux drops to zero at angles of about ±90° (The data points at 90° represent the range from 80° to 100°, therefore shows a value above 0).

In conclusion, Tonatiuh's dealing with reflection and its general functionality for ray-tracing is seen as sufficiently understood to utilize the software with confidence.

Stellenbosch University https://scholar.sun.ac.za

Appendix C

Additional Information to Simulation Model

Stellenbosch University https://scholar.sun.ac.za

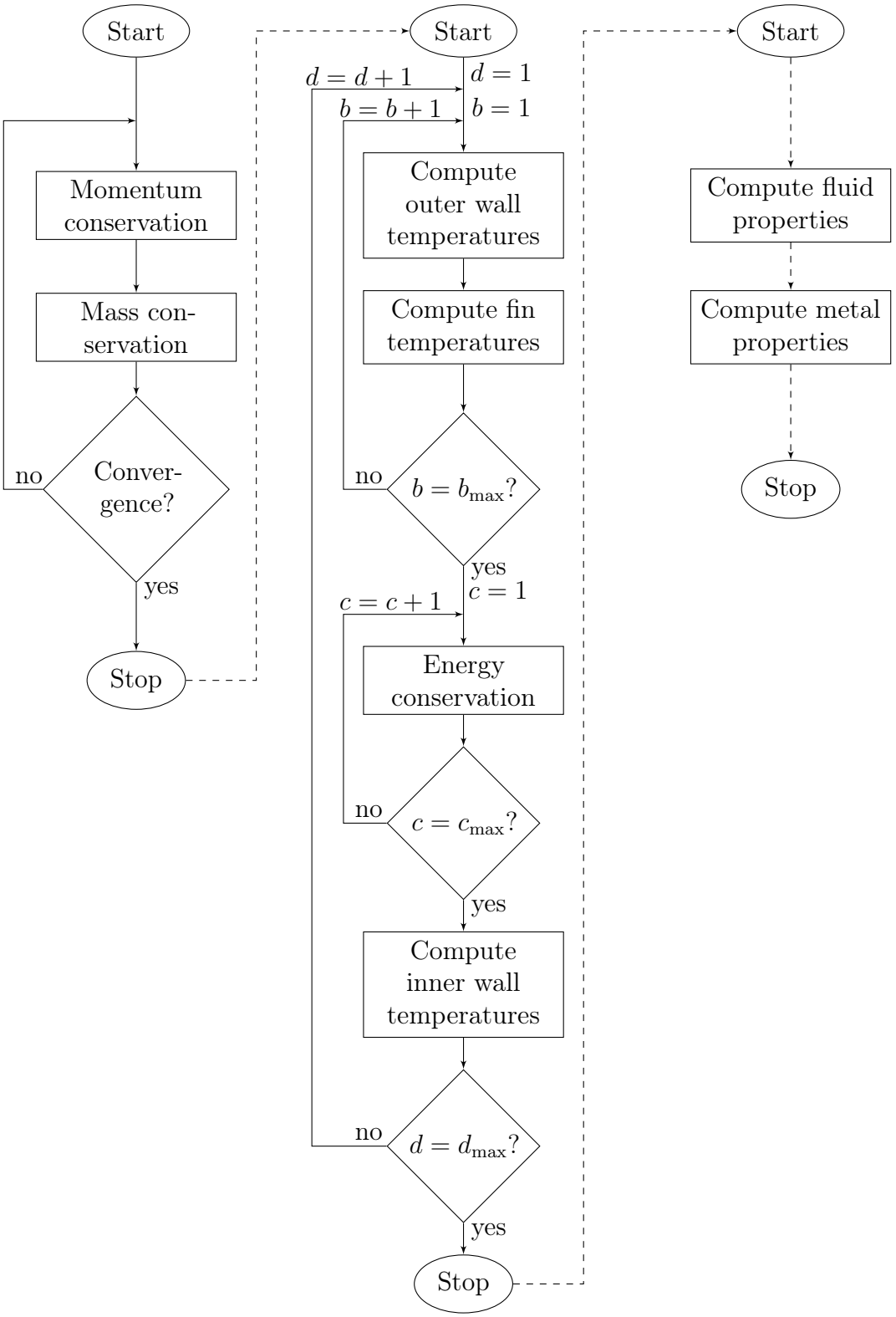

Figure C.1: Detailed flow chart for: Velocity and pressure computation (left), Energy conservation (center) and updating of temperature dependent properties (right)

Stellenbosch University https://scholar.sun.ac.za

Appendix D

Grid Independence of Computer Model

A grid independence analysis was conducted to establish a minimum required grid resolution in order to obtain reliable results. The grid independence was examined for the radial fin resolution m as well as the axial increments n along the spike length.

The analysis was conducted with an adiabatic spike tip. Further simulation parameters are listed in Table D.1.

Table D.1: Simulation conditions for grid dependence analysis

parameter	value unit
$T_{\text{air,in}}$	300 °C
$u_{\text{air,in}}$	8.37 m/s
$p_{\text{air,in}}$	1000 kPa
$\dot{q}''_{\text{rad,spike}}$	50 kW/m^2
$\dot{q}''_{\text{rad,tip}}$	0 kW/m^2
$T_{\text{air},\infty}$	20 °C
$u_{\text{air},\infty}$	3 m/s

Stellenbosch University https://scholar.sun.ac.za

Table D.2: Dependence of air outlet temperature and pressure on grid resolution

parameter	unit				
number of nodes n[1]	-	10	20	40	80
$T_{\text{air,out}}$	°C	690.4	693.1	694.5	695.1
$p_{\text{air,out}}$	Pa	999 064	999 071	999 075	999 077
number of nodes m[2]	-	5	10	20	40
$T_{\text{air,out}}$	°C	692.7	693.1	693.3	694.4
$p_{\text{air,out}}$	Pa	999 072	999 072	999 071	999 071

[1] in axial direction, resolution m in fins set as 10
[2] in fin, radial direction, resolution n axially set as 20

A reduction in the fin discretization leads to increased radiative heat transfer from the fin walls onto the inner tube. As a result, the air flow within the inner tube is heated marginally more with lower fin node numbers , leading to earlier increase in air flow velocity, and therefore increased pressure drop. This explains why the total pressure drop for $m = 5$ equals that of $m = 10$, while the air outlet temperature is lower.

Stellenbosch University https://scholar.sun.ac.za

Appendix E

The Crossed-Strings Method

The crossed-strings method is a practical method that allows the computation of view factors for two-dimensional problems (between infinitely long surfaces) based on simple representation of geometry by direct lines. The method has been developed by H.C. Hottel in the 1950's (Çengel and Ghajar, 2011). A basic representation of the crossed-strings method is illustrated in Figure E.1a. The view factor $F_{i\to j}$ between two surfaces i and j can be computed as

$$F_{i\to j} = \frac{\sum(\text{crossed strings}) - \sum(\text{uncrossed strings})}{2 \times (\text{string on surface } i)}. \tag{E.1}$$

Note that the method is also applicable to surfaces that share a common edge.

Applying equation (E.1) to the problem depicted in Figure E.1a, the view factor $F_{1\to 2}$ between surface 1 and surface 2 is computed as

$$F_{1\to 2} = \frac{(L_3 + L_4) - (L_1 + L_2)}{2 \times B_1}. \tag{E.2}$$

The crossed-strings method allows simple and robust implementation of view factor computation into a heat transfer code. The visual representation of the view factor problems between the two narrow side of the rectangular duct is shown in Figure E.1b and of the view factor between a narrow side and a discretized fin element in Figure E.1c. Standard geometrical problems such as shown in Figure E.1b and Figure E.1c have been solved analytically , as provided in Howell (2011) and provide the same solution as the crossed-strings method.

Stellenbosch University https://scholar.sun.ac.za

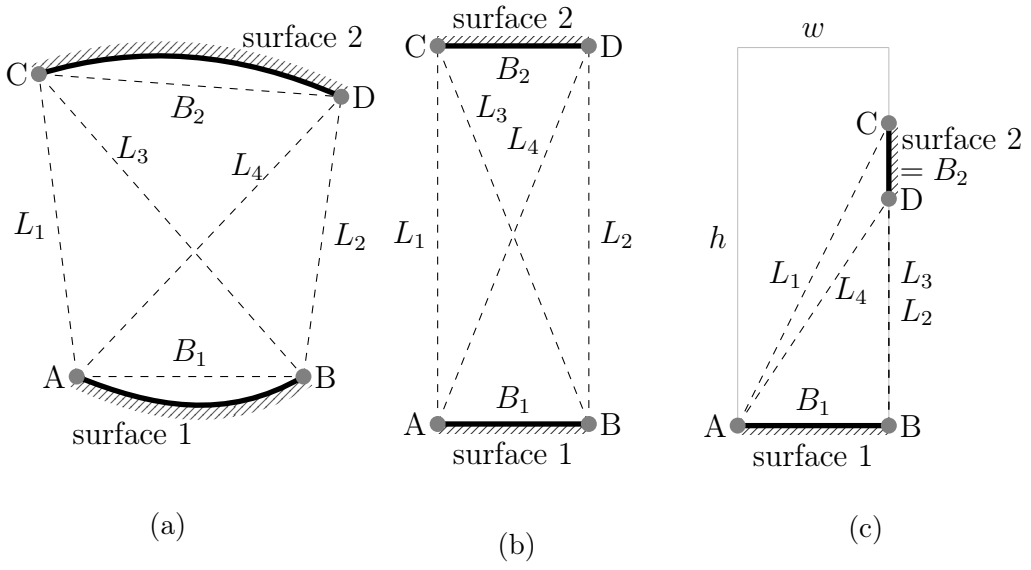

Figure E.1: The crossed-strings-method (a) general illustration for $F_{1\to2}$ between two surfaces, (b) and (c) for computation of $F_{1\to2}$ between top and bottom of a rectangular duct and between the bottom and a wall segment (discretized fin element).

Stellenbosch University https://scholar.sun.ac.za

Appendix F

Nusselt Number in Rectangular Duct for Laminar Flow

Nusselt numbers for fully developed laminar flow inside rectangular ducts for a variety of boundary conditions are provided by (Shah and London, 1978). For the heat transfer from only one surface of a rectangular duct Shah and London provide Nusselt numbers for a variety of duct shapes in tabular form. Figure F.1 shows the Nusselt numbers for constant axial heat flux and constant axial surface temperature over the duct shape ratio w/h for the case where only one width w is not adiabatic.

In the case of the SCRAP receiver the heat convection from the air stream to the wall of the inner tube is neither subject to a constant surface flux ($\dot{q}''_s(x) = \text{const.}, Nu = Nu_H$) nor to a constant surface temperature ($T_s(x) = \text{const.}, Nu = Nu_T$). As the difference in between the two Nusselt numbers can be explained with different temperature profiles for the two cases, an average value is used as an initial Nusselt number for the simulation.

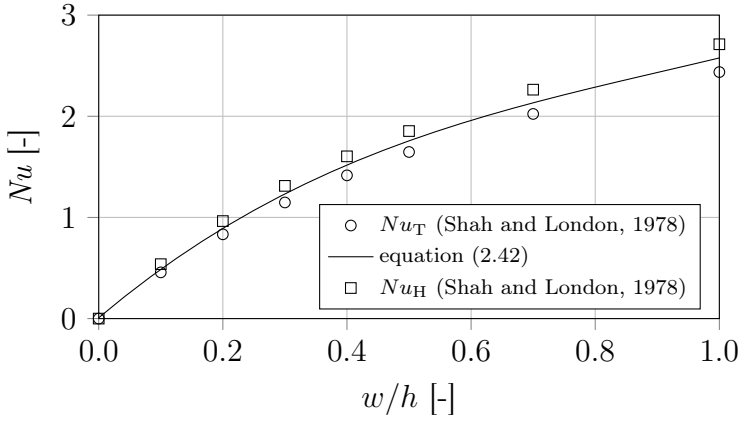

Figure F.1: Nusselt number for laminar flow in a rectangular duct for one heated duct wall w as function of the duct shape

Stellenbosch University https://scholar.sun.ac.za

A third order polynomial curve fit for the mean Nusselt number between the cases $Nu = Nu_{\mathrm{H}}$ and $Nu = Nu_{\mathrm{T}}$ is

$$Nu = 1.508882\left(\frac{w}{h}\right)^3 - 4.122727\left(\frac{w}{h}\right)^2 + 5.182207\left(\frac{w}{h}\right) + 0.008172 \quad \text{(F.1)}$$

The curve fit can be employed to accommodate various duct shapes in the simulation.

In the same way as outlined above the heat transfer coefficient for heating the airflow in the outer duct is based on a curve fit to the average between Nu_{H} and Nu_{T}. The curve fit can be expressed as

$$Nu = 9.29451\left(\frac{w}{h}\right)^4 - 25.2036\left(\frac{w}{h}\right)^3 + 27.1205\left(\frac{w}{h}\right)^2 - 15.8021\left(\frac{w}{h}\right) + 7.87845 \quad \text{(F.2)}$$

and is shown in Figure F.2.

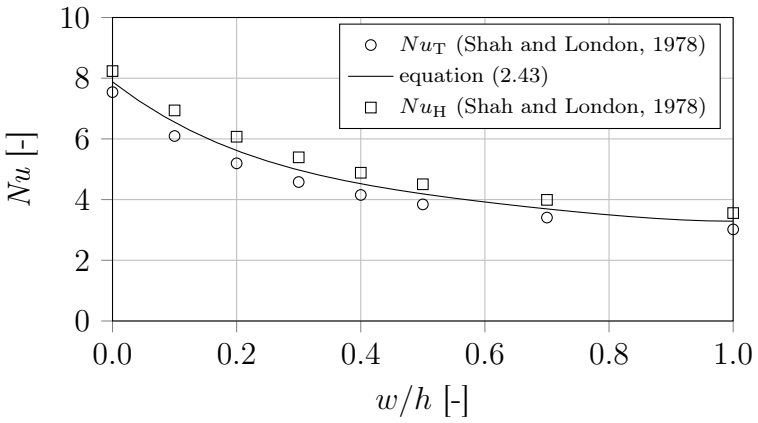

Figure F.2: Nusselt numbers for laminar flow in a rectangular duct heated from three sides, with one w adiabatic as function of the duct shape

Stellenbosch University https://scholar.sun.ac.za

Appendix G

Reference Flat Plate Model for Jet Impingement Cooling

An axis symmetric two-dimensional model was reproduced where a pipe of diameter D points a jet at a heated plate a distance H/D from the nozzle. A sketch of the analyzed case is shown in Figure G.1. The air velocity distribution within the pipe is provided, using a user defined function (udf). Some pipe length of multiple D is included to permit checking the correctness of the employed udf.

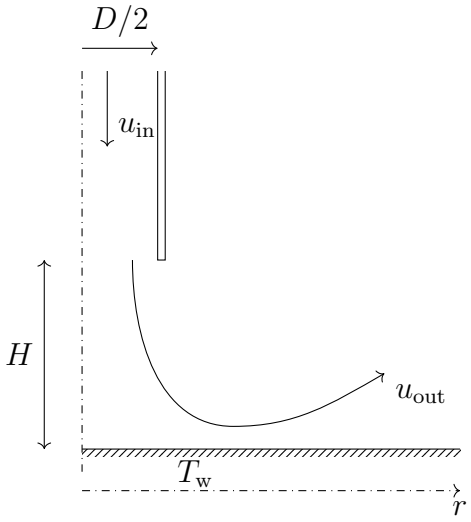

Figure G.1: Sketch of the axis symmetric two-dimensional geometry employed to model Nu of the impinging air flow on the spike tip.

A scenario with a Reynolds number of $Re = 23\,000$ and $H/D = 6$ was simulated and compared to experimental data. The air flow enters through a duct under adiabatic conditions and is heated by the wall it impinges on. Curves showing the resultant Nu for the standard k-ε model, the realizable

Stellenbosch University https://scholar.sun.ac.za

k-ε model as well as the RSM are shown in Figure G.2. For each model a sensitivity study was conducted for increasing mesh refinement.

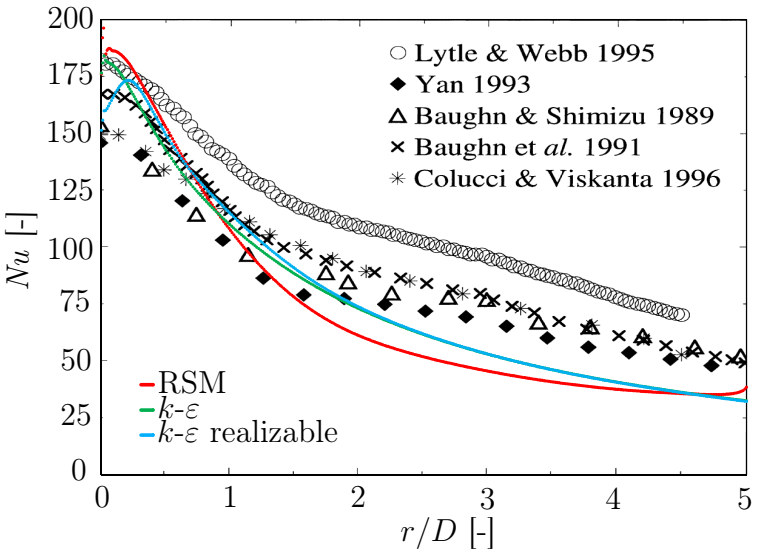

Figure G.2: Nu over r/D for k-ε model, realizable k-ε model as well as RSM model over various experimental results (simulation results overlaid on experimental results summarized by Behnia *et al.* (1997))

Here, the Nusselt number is defined as $Nu = h\ D/k$, where D is the pipe diameter, k the air's thermal conductivity at pipe outlet and h the local heat transfer coefficient computed from the local heat flux with reference to the mean pipe outlet temperature. All three models appear to predict peak Nu rather well in the stagnation zone near $r/D = 0$. The realizable k-ε model does not result in more accurate predictions than the standard k-ε model and predicts a dip in the center of the stagnation zone that is not expected from studying the experimental data Behnia *et al.* (1997). Towards larger r/D values the three models under-predict the local Nusselt numbers. This effect is less pronounced for the k-ε models as compared to the RSM model. It appears that the k-ε model can generate results in a sufficiently accurate range for the purpose of the analysis with a tendency to under-predict rather than over-predict.

The k-ε model provided reasonable results at low computational expense compared to the RSM. The k-ε model was as a consequence used to model jet impingement heat transfer for the spike tip.

Stellenbosch University https://scholar.sun.ac.za

Appendix H

Grid independence of spike tip model

This section provides additional insight into the applied procedure with the CFD simulation conducted to gain basic understanding of impinging jet heat transfer at the spike tip. The procedure is illustrated on the example of the 18 mm nozzle .

A two-dimensional geometry was generated to represent a simplified spike tip, neglecting internal fins. The model had a varying inner tube's inner diameter to permit simulating different nozzle sizes. The model extends 0.2 m upstream and 0.2 m downstream of the tip as shown in Figure H.1. Here, the capital letters indicate named selections for application of boundary conditions. The inlet is marked with A. B marks the symmetry axis, C the outlet. D represents the inner tube's walls on outside and inside. Section E the heated wall extending from the tip through to the end of the model.

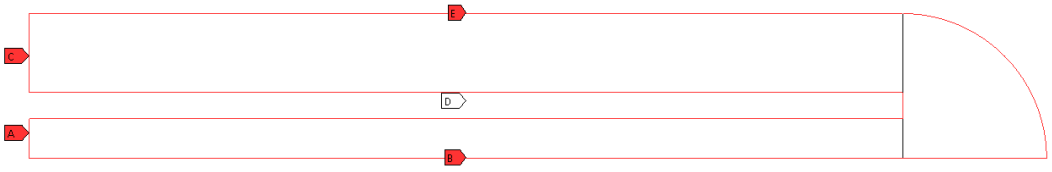

Figure H.1: Screenshot of the simulated domain with capital letters marking named selections for boundary conditions

The $k-\varepsilon$ model was used with enhanced wall treatment activated to enable solving for a fine mesh with nodes in the laminar sublayer. The average Nusselt, $\overline{Nu}$, number was computed from the local Nusselt number, Nu_ϕ, recorded at the spike tip as

$$Nu_\phi = \frac{hd_{\text{nozzle}}}{k}, \tag{H.1}$$

Stellenbosch University https://scholar.sun.ac.za

where h is the local heat transfer coefficient, d_{nozzle} the nozzle diameter and k the air's thermal conductivity on nozzle outlet. The average Nusselt number associated to a nozzle is computed by area-averaging the recorded local Nusselt numbers over the hemispherical tip wall.

The mesh was continuously refined until change in the average Nusselt number became marginal. This procedure was supported by observing y^+ to conclude on a suitably refined mesh with y^+ being at about 1 or below. A coarse mesh is illustrated in Figure H.2. The inner tube and annular space can be seen on the left hand side with the mesh being refined towards the walls, using a bias factor and mapped face meshing. The spike tip mesh is controlled by amending cell face values as well as the cell size along the walls or axis, respectively. The grid resolution at the tip wall is increased applying an inflation layer.

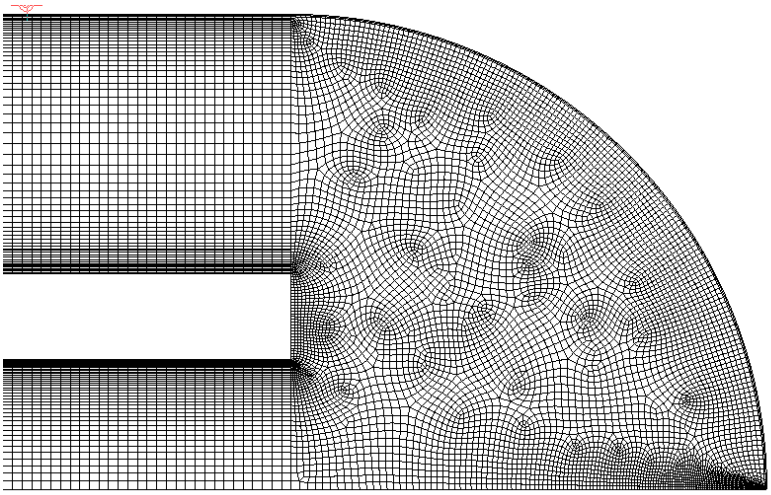

Figure H.2: Screenshot of a coarse mesh at the spike tip

Based on the shown example with a nozzle diameter of $d_{\text{nozzle}} = 18\,\text{mm}$, a plot for grid refinement is shown in Figure H.3, where the number of nodes in the spike tip segment is shown. Notably, towards higher node numbers the change in $\overline{Nu}$ reduces. At a number of nodes of approximately 75 000 the largest values of y^+ in the tip region, y^+_{max}, is at around 1. It can be noted that thereafter increasing mesh refinement does not result in improved results.

Stellenbosch University https://scholar.sun.ac.za

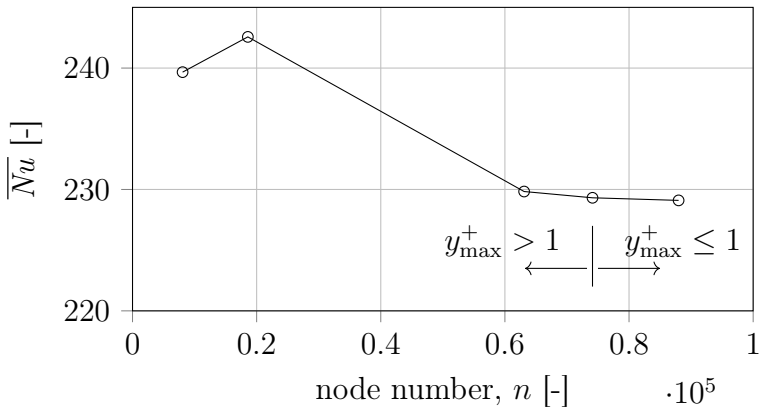

Figure H.3: Development of $\overline{Nu}$ over refining the grid resolution at the spike tip

Figure H.4 illustrates the values of y^+ for the tip region, where $\phi = 0°$ corresponds to the center line and $\phi = 90°$ to the contact point from tip to cylindrical spike body. Figure H.4 shows the y^+ data for the highest node number shown in Figure H.3. It can be seen that the y^+ is consistently at values below 1.

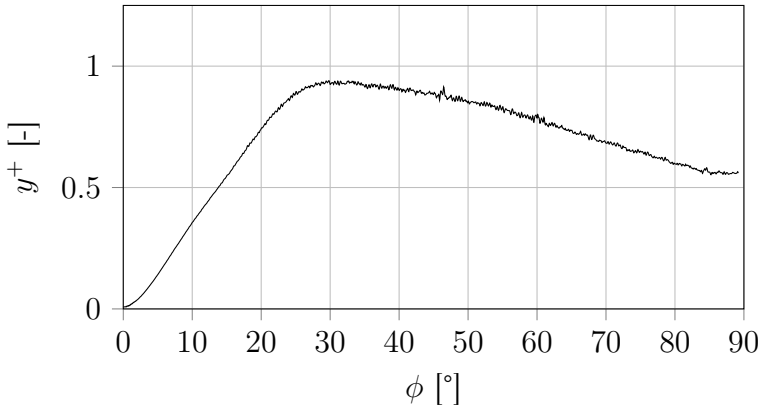

Figure H.4: Plot of y^+ at the spike tip for a suitable mesh

The procedure outline above was applied to all nozzle sizes.

Stellenbosch University https://scholar.sun.ac.za

Stellenbosch University https://scholar.sun.ac.za

Appendix I

Properties of Inconel Alloy 718

The relevant temperature dependent properties of Inconel alloy 718 are provided in the following subsections. Inconel alloy 718 is selected from the family of Inconel alloys for the availability of test results into a range of elevated temperatures.

I.1 Thermal conductivity

The properties of metals are temperature dependent. The thermal conductivity of Inconel alloys depends on the particular Inconel steel type. The thermal conductivity of Inconel Alloy 718 (SMC, 2007) is shown in Figure I.1. The data points can well be approximated by a linear curve fit

$$k/(\mathrm{W/m\,K}) = 1.6031 \times 10^{-2}(T/^{\circ}\mathrm{C}) + 11.032, \tag{I.1}$$

which fits to the data points within $\pm$ 0.8 %.

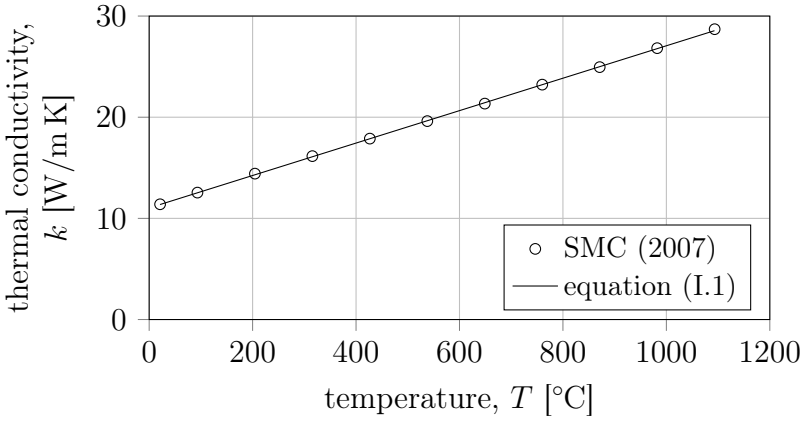

Figure I.1: Thermal conductivity k of Inconel alloy 718 and curve fit

Stellenbosch University https://scholar.sun.ac.za

I.2 Thermal emissivity

The thermal emissivity of Inconel alloy 718 over material temperature is shown in Figure I.2 and approximated with

$$\varepsilon = 4.4373\times10^{-10}(T/°\mathrm{C})^3 - 1.2198\times10^{-6}(T/°\mathrm{C})^2 + 1.1909\times10^{-3}(T/°\mathrm{C}) + 0.45787, \tag{I.2}$$

which fits to the data points within ± 1.2 %. The data points, however, are extracted from Figure 7(c) in (Greene *et al.*, 2000), which was provided with a measurement error of 3 %.

Figure I.2 illustrates the curve fit of equation (I.2) over the data points.

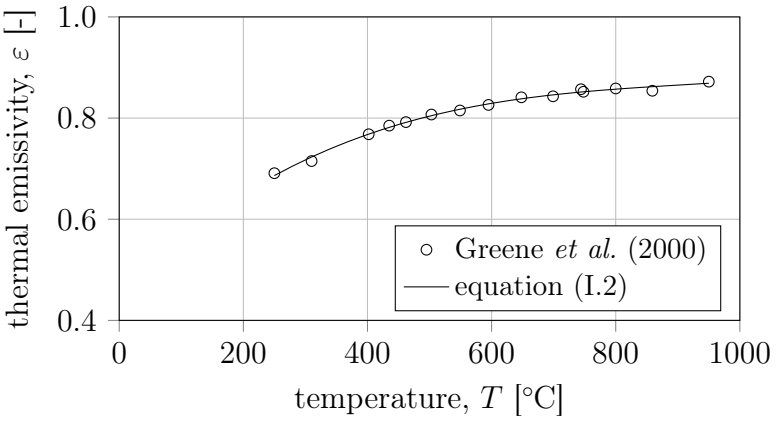

Figure I.2: Thermal emissivity ε of Inconel alloy 718 and curve fit

I.3 Thermal absorptivity

Assuming Kirchhoff's law holds through the temperature range presented, the absorptivity α is equally represented by equation (I.2) for Kirchhoff's law states $\alpha = \varepsilon$.

I.4 Oxidization

Greene and Finfrock (2001) have studied the oxidation behavior of Inconel alloy 718 in the temperature range from 700 °C to 1347 °C. The oxidization of Chromium provides a protective layer on the metal surface which prevents continued oxidization. Greene and Finfrock found through experiments at high temperatures that the protective layer remains intact for heating up to 900 °C. At that temperature oxidization occurs in the first 24 h of heat exposure and no further oxidization was detectable afterwards, the alloy is passivated. At

Stellenbosch University https://scholar.sun.ac.za

temperatures above 950 °C Inconel alloy 718 experiences continued oxidization at a parabolic rate, typical for super-alloys (Greene and Finfrock, 2001).

Stellenbosch University https://scholar.sun.ac.za

Stellenbosch University https://scholar.sun.ac.za

Appendix J

Variations of Test Setup Configurations

The test setup was designed in a modular manner in order to permit further research on the same setup. Figure J.1 to Figure J.5 show possible combinations.

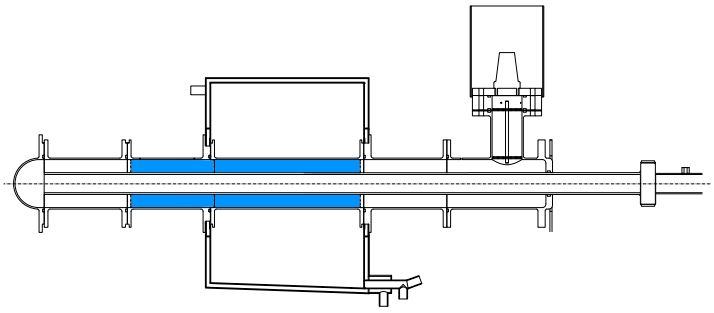

Figure J.1: Experimental setup in the configuration used for this work

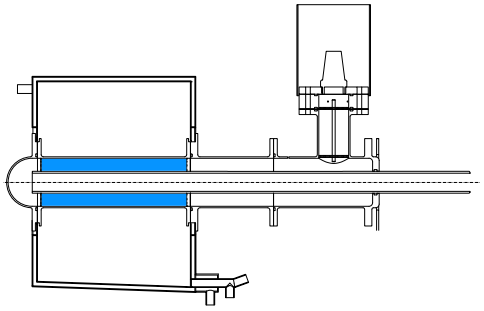

Figure J.2: Experimental setup in a configuration permitting study on heat transfer in the inlet region after the spike tip

Stellenbosch University https://scholar.sun.ac.za

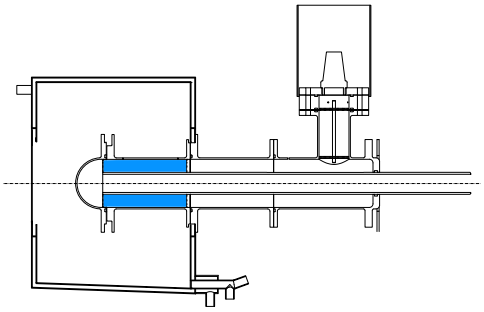

Figure J.3: Experimental setup in a configuration allowing to study heating of the tip as well an internally finned segment

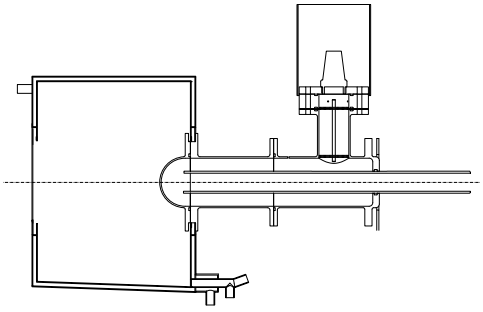

Figure J.4: Experimental setup in a configuration permitting study on jet impingement cooling in the spike tip

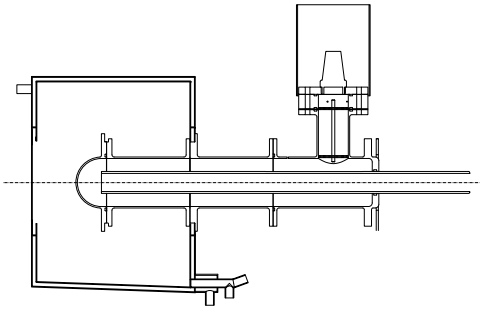

Figure J.5: Experimental setup in a configuration heating the tip and an annular section

Stellenbosch University https://scholar.sun.ac.za

Appendix K

Properties of Dry Air

K.1 Temperature range 300 °C to 1000 °C

The used thermophysical properties for dry air from 300 °C to 1000 °C for pressures from atmospheric to 20 bar are shown in the following. The equation for air density is based on the ideal gas law (see equation (K.1)). Specific heat, dynamic viscosity and thermal conductivity are curve-fit data to the table provided in the VDI Wärmeatlas (VDI, 2010). The curve fit is performed on the data for a pressure of 10 bar.

Equations (K.2) to (K.4) deviate from the tabular data provided in VDI (2010) by below 0.5 % for the pressure between 1 bar to 20 bar.

Density The density ρ is calculated using the ideal gas law:

$$\rho = \frac{p}{R_{\text{specific}} T} \tag{K.1}$$

where p is the pressure in Pa, R_{specific} the specific gas constant of dry air (287.058 J/kg K) and T the air temperature in Kelvin.

Specific heat The equation for c_p is

$$c_\text{p}/(\text{kJ/kg K}) = -8.256 \times 10^{-8} (T/°\text{C})^2 + 3.050 \times 10^{-4} (T/°\text{C}) + 0.9633. \tag{K.2}$$

The specific heat c_p of air has a high dependency on pressure at low temperatures (below 300 °C). The curve fit for the specific heat of dry air over the air temperature is depicted in Figure K.1.

Dynamic viscosity The equation for μ is

$$\mu/(10^{-6}\text{Pa s}) = -6.898 \times 10^{-6} (T/°\text{C})^2 + 3.852 \times 10^{-2} (T/°\text{C}) + 19.01. \tag{K.3}$$

The curve fit for the dynamic viscosity of dry air over the air temperature is depicted in Figure K.2.

Stellenbosch University https://scholar.sun.ac.za

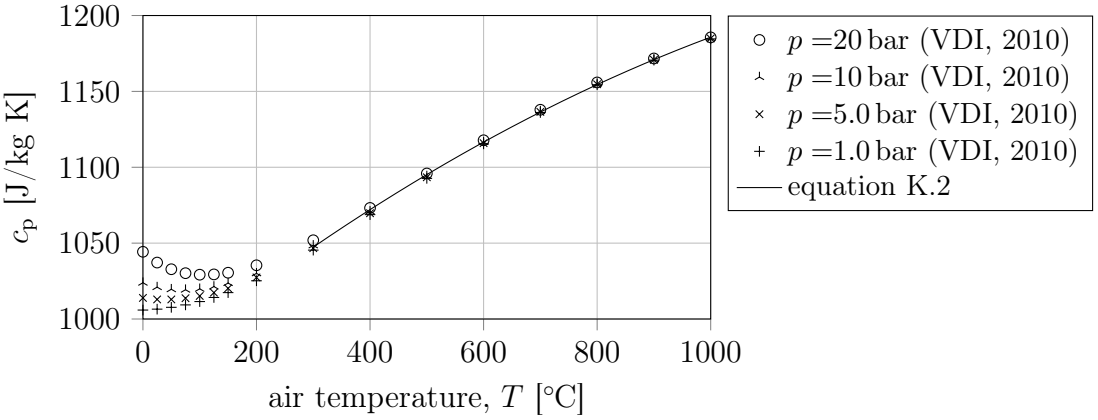

Figure K.1: Curve fit for c_p of air (equation (K.2)) for 300 °C to 1000 °C and 1 bar to 20 bar and data points from VDI (2010)

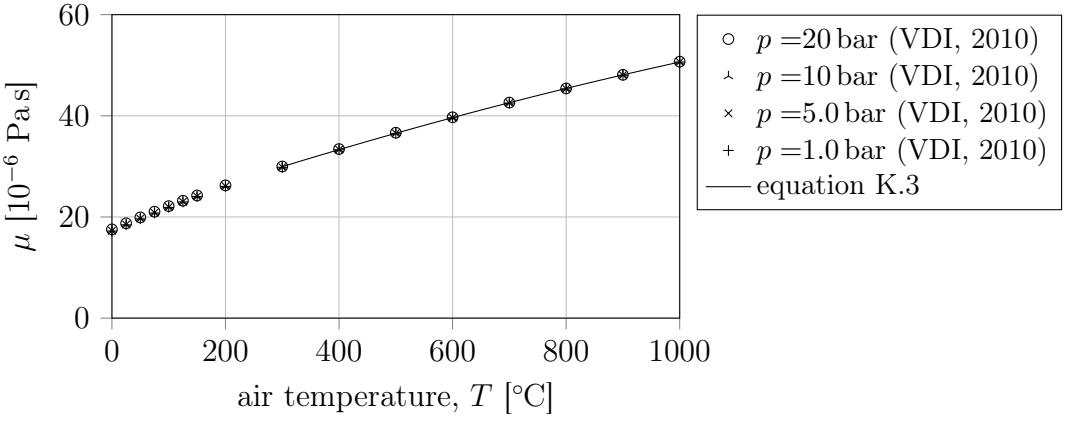

Figure K.2: Curve fit for μ of air (equation (K.3)) for 300 °C to 1000 °C and 1 bar to 20 bar and data points from VDI (2010)

Thermal conductivity The equation for k is

$$k/(\mathrm{mW/m\,K}) = -7.930 \times 10^{-6}(T/°\mathrm{C})^2 + 6.243 \times 10^{-2}(T/°\mathrm{C}) + 26.61. \quad \text{(K.4)}$$

The curve fit for the thermal conductivity of dry air over the air temperature is depicted in Figure K.3.

Stellenbosch University https://scholar.sun.ac.za

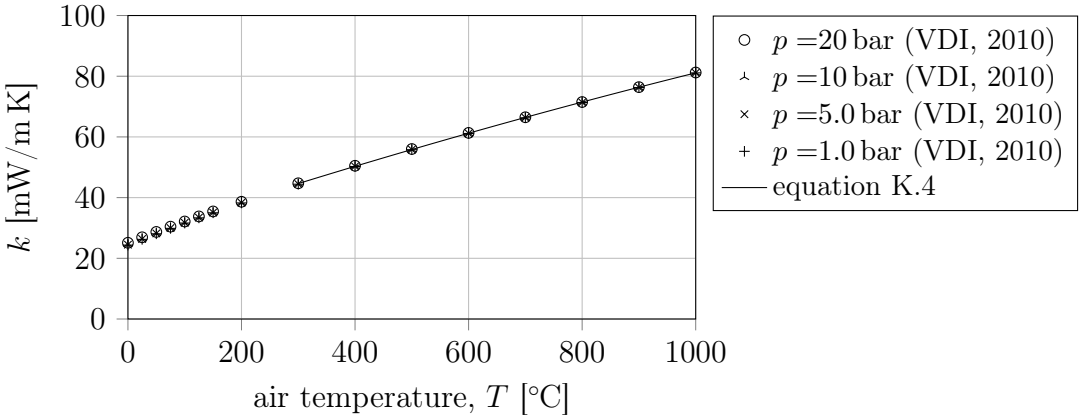

Figure K.3: Curve fit for k of air (equation (K.4)) for 300 °C to 1000 °C and 1 bar to 20 bar and data points from VDI (2010)

K.2 Temperature range 0 °C to 100 °C

For laboratory testing the thermophysical properties of air in the range of 0 °C to 100 °C at pressures from 1 bar to 10 bar are required. The air density for this range is computed by the ideal gas law as lined out in equation (K.1).

Equations (K.5) to (K.7) deviate from the tabular data provided in VDI (2010) by below 0.04 % for the pressure between 1 bar to 10 bar.

Specific heat The equation for c_p is

$$\begin{aligned} c_\mathrm{p}/(\mathrm{kJ/kg\,K}) =& 1.0043 - 2.3388 \times 10^{-7}(T/°\mathrm{C}) + 6.6667 \times 10^{-7}(T/°\mathrm{C})^2 \\ &+ 1.8989 \times 10^{-3}(p/\mathrm{bar}) - 1.05311 \times 10^{-5}(p/\mathrm{bar})(T/°\mathrm{C}) \\ &+ 2.1111 \times 10^{-6}(p/\mathrm{bar})^2. \end{aligned} \tag{K.5}$$

The curve fit for the specific heat of dry air over the air temperature is depicted in Figure K.4.

Dynamic viscosity The equation for μ is

$$\begin{aligned} \mu/(10^{-6}\mathrm{Pa\,s}) =& 17.204 + 4.9883 \times 10^{-2}(T/°\mathrm{C}) - 3.0781 \times 10^{-5}(T/°\mathrm{C})^2 \\ &+ 1.5157 \times 10^{-2}(p/\mathrm{bar}) - 3.39344 \times 10^{-5}(p/\mathrm{bar})(T/°\mathrm{C}) \\ &+ 7.3333 \times 10^{-5}(p/\mathrm{bar})^2. \end{aligned} \tag{K.6}$$

The curve fit for the dynamic viscosity of dry air over the air temperature is depicted in Figure K.5.

Stellenbosch University https://scholar.sun.ac.za

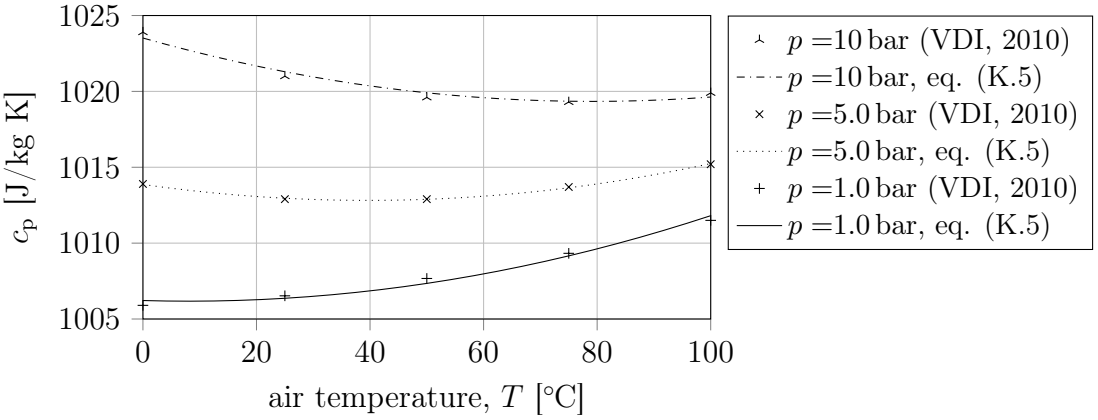

Figure K.4: Curve fit for c_p of air (equation (K.5)) for 0 °C to 100 °C and 1 bar to 20 bar and data points from VDI (2010)

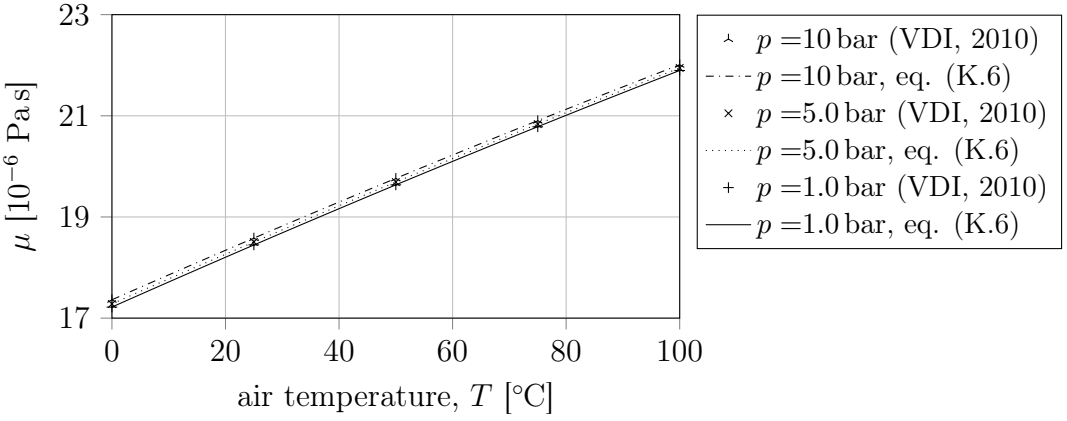

Figure K.5: Curve fit for μ of air (equation (K.6)) for 0 °C to 100 °C and 1 bar to 20 bar and data points from VDI (2010)

Thermal conductivity The equation for k is

$$\begin{aligned} k/(\mathrm{mW/m\,K}) =& 24.328 + 7.6229 \times 10^{-2}(T/°\mathrm{C}) - 3.5238 \times 10^{-5}(T/°\mathrm{C})^2 \\ &+ 3.4601 \times 10^{-2}(p/\mathrm{bar}) - 1.1489 \times 10^{-4}(p/\mathrm{bar})(T/°\mathrm{C}) \\ &+ 1.9889 \times 10^{-4}(p/\mathrm{bar})^2 \end{aligned} \tag{K.7}$$

The curve fit for the thermal conductivity of dry air over the air temperature is depicted in Figure K.6.

Stellenbosch University https://scholar.sun.ac.za

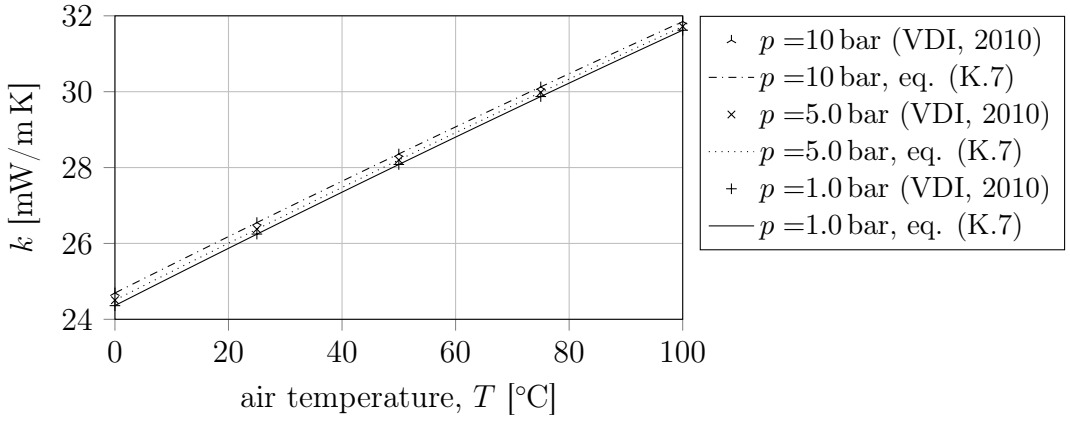

Figure K.6: Curve fit for k of air (equation (K.7)) for 0 °C to 100 °C and 1 bar to 20 bar and data points from VDI (2010)

Stellenbosch University https://scholar.sun.ac.za

Stellenbosch University https://scholar.sun.ac.za

Appendix L

Manufacturing of Internally Finned Sections[1]

The test setup was built as a once-off prototype. Accordingly, a manufacturing process was required that permitted production in a cost-efficient manner. A machining process was required that permitted cutting a depth of approximately 200 mm, introduce little force or heat to avoid narrow fin tips deforming/breaking and provide cost effective production.

It was decided to employ an electrical discharge machining process (wire cutting) that permitted fulfilling the above requirements. With a wire diameter of 0.10 mm, a radius of $r = 0.35$ mm was selected for the fin roots (see Figure M.1) in order to permit the wire to cut a smooth curvature. Due to vertical space requirements for mounting brackets in the wire cutting machine a part length of 200 mm was selected. Figure L.1 shows the 114 mm section prior to wire cutting and the 200 mm test section mounted in the wire cutting machine. The spike components were manufactured from 7050 aluminum alloy.

Figure L.2 shows an internally finned section after wire cutting. The component shown features protruding fins in order to form a minimal air gap when connected to the heated section. As shown in Figure 3.1 the beginning of the fins is recessed on the upstream as well as downstream side of the heated section in order to reduce the impact of the flange onto radial thermal conduction from the hot surface (exposed to steam) to the internal fins.

The manufacturing cost was R18 639 (excluding material) for both internally finned segments. Manufacturing was conducted in house at Stellenbosch University's Institute for Advanced Tooling (IAT).

[1]Parts of this section have been published in Lubkoll *et al.* (2016*a*)

Stellenbosch University https://scholar.sun.ac.za

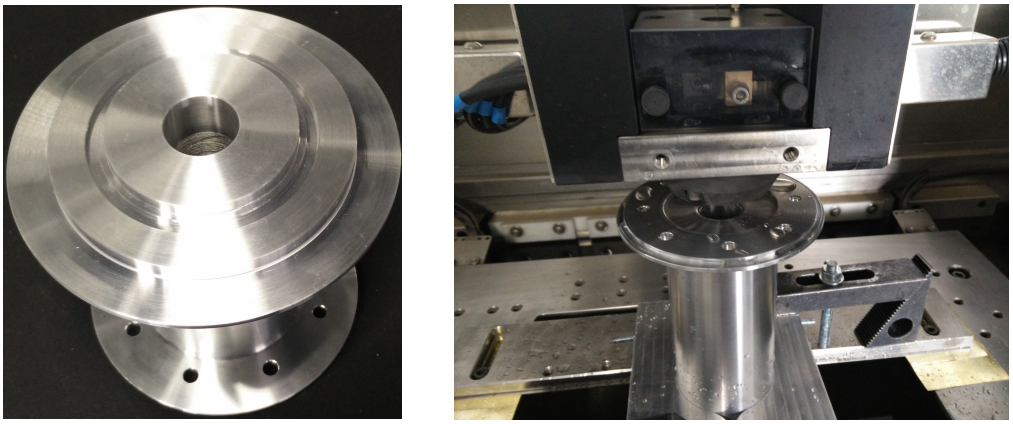

Figure L.1: Photograph of the 114 mm section prior to machining (left) and the 200 mm section mounted in the EDM machine (right).

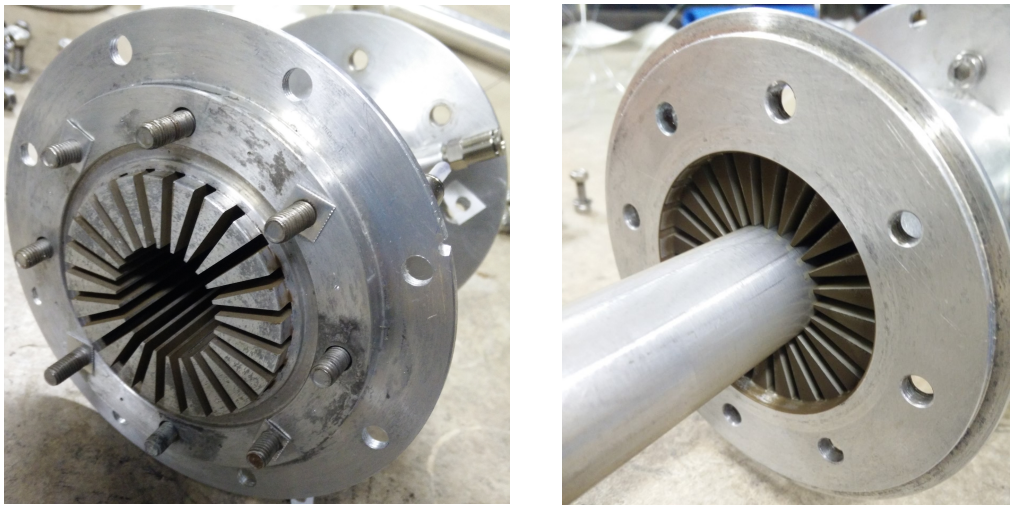

Figure L.2: Photograph of the 114 mm section after EDM machining (left) and the same section from the other side with inner tube inserted (right). The dark brown discoloring on the fins are small rust particles passing through the 40 μm air filter; a phenomenon occurring during commissioning phase at high flow rates.

Stellenbosch University https://scholar.sun.ac.za

Appendix M

Stress Analysis for Experimental Setup[1]

With pressures of up to 1000 kPA possible during the experiments the peak stress in the internally finned sections were analyzed using FEM. The peak stress occurs on the inner side of the pipe wall where stress concentration is observed on the roots. Literature (such as Pikley, 1997) does not offer a stress concentration factor directly applicable to a spike's geometry. To develop a sound understanding of stress distribution and peak stress values a minimal periodic sample was simulated in MSC Patran (MSC, 2014). The sample contains half a duct including half a fin (see Figure M.1).

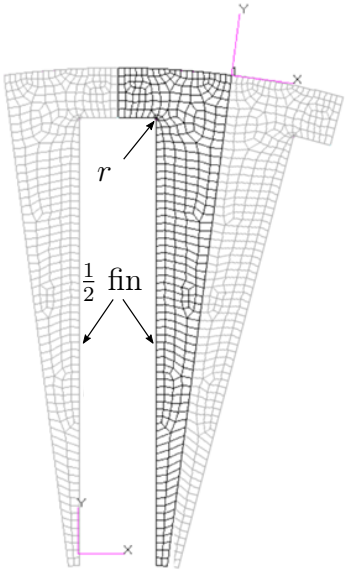

Figure M.1: Coarse mesh of FEM model showing half fin and two further half fins shown for illustration purposes.

[1]Parts of this section have been published in Lubkoll *et al.* (2016*a*)

Stellenbosch University https://scholar.sun.ac.za

The simulation boundary conditions applied were edge pressure on the inside and outside walls of 1000 kPA and 100 kPA, respectively. The symmetric boundary condition is configured as a wall node based restriction of transversal (x-direction) movement ($<0;\ ;>$) and rotation around the axis in axial (z-) direction ($<;\ ;0>$). A coordinate system on each boundary is required to configure the boundary conditions as described (see local coordinate system on top right corner of Figure M.1).

The linear static solver is used to compute the stress. The peak stress is observed with increased mesh resolution until convergence is achieved. Increasing grid resolution was conducted by splitting each quad cell into four in each step, which is permissible due to the relatively small computational expense of the refined setups. The simulation was repeated with increasing grid resolution until the solution converged. The development of the peak stress over a refined grid is depicted in Figure M.2 and shows the peak stress to appear to be leveling out at about 58 MPa (here, for a radius r of 0.1 mm).

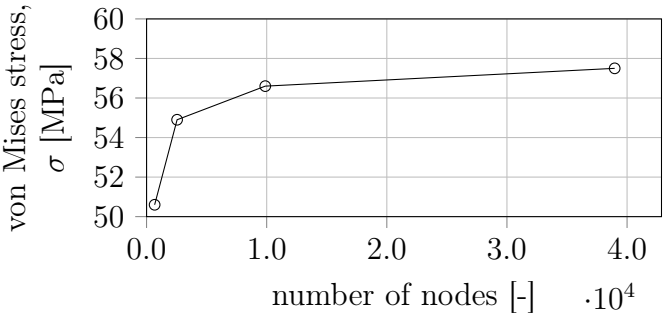

Figure M.2: Peak stress development over number of nodes

In comparison, the stress in tangential direction for a cylindrical pressure vessel (here, the tube without internal fins) is approximated with

$$\sigma_{\mathrm{t}} = \frac{pr}{t}, \tag{M.1}$$

where t is the wall thickness and the cylinder is assumed as thin walled. As a reference, a tube with $r = 0.035$ m, $t = 2$ mm and a pressure p of 10 bar will thus result in $\sigma_{\mathrm{t}} = 15.75$ MPa (assuming an external ambient pressure of 1 bar). This case of a plain circular tube has been simulated in MSC Patran to validate the simulated result and setup. The identical case as a above with $p = 10$ bar and $r = 35$ mm and a wall thickness $t = 2$ mm has been configured. A 7.5° slice of the tube was meshed and the edge pressure boundary condition applied. As a result the inner wall stress $\sigma_{\mathrm{t,i}}$ was given with 15.7 MPa, correlating well with the analytical solution of 15.75 MPa calculated using equation (M.1).

A peak stress of about 58 MPa suggests a stress concentration factor for the rectangular duct with a 0.1 mm fillet of $K = 3.7$. This value was compared

Stellenbosch University https://scholar.sun.ac.za

to literature values from Pikley (1997) on cases that suggested some similarity. Assuming a radius at the fin roots of 0.1 mm, the stress concentration factor K for a shoulder fillet for a stepped at tension bar under tension can be estimated in the range of $K = 5$. As a further reference, K for opposite deep hyperbolic notches in an infinitely wide thin bar under tension can be estimated at about $K = 8$. With these references in mind and considering stress concentration factors tending to be lower for multiple repeating notches as compared to a single notch it seems that the established peak stress simulated in MSC Patran is valid.

Stellenbosch University https://scholar.sun.ac.za

Stellenbosch University https://scholar.sun.ac.za

Appendix N

Properties of Pyromark 2500

Ho et al (Characterization of Pyromark 2500 Paint for High-Temperature Solar Receivers) have investigated Pyromark 2500 as coating for central receiver applications. Pyromark is the current state of the art paint applied to central receiver absorber tubes. Their work included the analysis of thermal emittance of Pyromark 2500 on Inconel as well as SS304 stainless steel over temperatures ranging up to 1000 °C. Their work found a relatively stable thermal emittance ε of Pyromark 2500 between 0.85 to 0.9 in the temperature range of 300 °C and 1000 °C. A thermal emittance of 0.9 is used as the conservative assumption for the analysis in this work.

Stellenbosch University https://scholar.sun.ac.za

Stellenbosch University https://scholar.sun.ac.za

Appendix O

Computation of Air Flow Rate from the Orifice Plate

The orifice plate design is based on the British Standard for measurement of fluid flow in closed conduits BSI (1984). The drop in static pressure over an orifice plate is measured to determine the air flow rate. The device consists of an inlet tube, an upstream and a downstream side flange, the orifice plate as well as a downstream tube. The flanges are equipped with static pressure tappings. The upstream tap is also used to measure gauge pressure to permit computation of fluid density. An illustration of the setup is shown in Figure O.1.

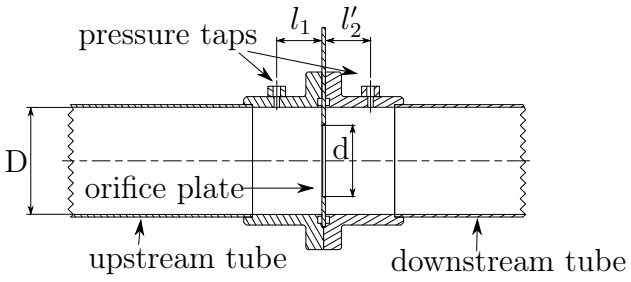

Figure O.1: Sketch of section through the orifice plate with relevant dimensions illustrated.

The mass flow rate $\dot{m}_{\text{air}}$ through the orifice plate is calculated as

$$\dot{m}_{\text{air}} = CE\varepsilon\frac{\pi}{4}d^2\sqrt{2\Delta p \times \rho_1} \tag{O.1}$$

where C is the coefficient of discharge, E the velocity approach factor and ε the air expansion factor. E is a function of the diameter ratio $\beta = d/D$:

$$E = \left(1 - \beta^4\right)^{-1/2}. \tag{O.2}$$

Stellenbosch University https://scholar.sun.ac.za

The discharge coefficient is computed using the Stolz equation (BSI, 1984).

$$C = 0.5959 + 0.0312\beta^{2.1} - 0.1840\beta^{8} + 0.0029\beta^{2.5}\left[\frac{10^6}{Re_{\mathrm{D}}}\right]^{0.75} \tag{O.3}$$

$$+ 0.0900 L_1 \beta^4 \left(1-\beta^4\right)^{-1} - 0.0337 L_2' \beta^3 \tag{O.4}$$

where $L_1 = l_1/D$ where l_1 is the distance of the upstream pressure tapping to the upstream face of the orifice plate. The same way L_2' is calculated as l_2'/D, where the $'$ symbolizes the reference for the distance being the downstream side of the orifice plate.

Lastly, the air expansion factor ε is calculated as

$$\varepsilon = 1 - \left(0.41 + 0.35\beta^4\right)\frac{\Delta p}{\kappa p_1} \tag{O.5}$$

with κ being the isentropic exponent defined as $\kappa = c_{\mathrm{p}}/c_{\mathrm{v}}$. The heat capacity at constant volume, c_v, can be calculated from the heat capacity at constant pressure, c_{p} as $c_{\mathrm{v}} = c_{\mathrm{p}} - R_{\mathrm{specific}}$.

With C being a function of the Reynolds number Re_{D}, which in turn is a function of the flow velocity u, the desired result, the computation is started with a guessed flow velocity and solved iteratively.

Stellenbosch University https://scholar.sun.ac.za

Appendix P

Additional Measurement Results

P.1 Static pressure along internally finned sections

Comparison of modeled and measured static pressure for the flow rates of $\dot{m}_{\text{air}} = 0.0408\,\text{kg/s}$, $\dot{m}_{\text{air}} = 0.0685\,\text{kg/s}$ and $\dot{m}_{\text{air}} = 0.162\,\text{kg/s}$ under adiabatic conditions investigated in chapter 4.

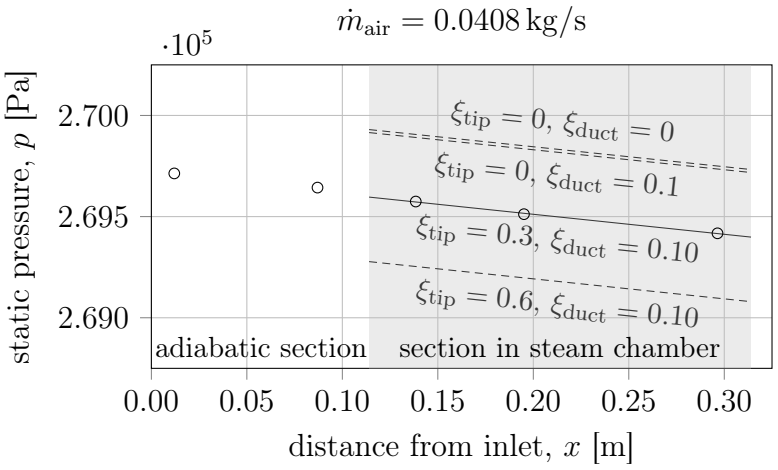

Figure P.1: Measured static pressure data points (circles) along the internally finned adiabatic section and section within the steam chamber (no heating) compared to simulation results for varying ξ_{tip} and ξ_{duct} for $\dot{m}_{\text{air}} = 0.0408\,\text{kg/s}$.

Stellenbosch University https://scholar.sun.ac.za

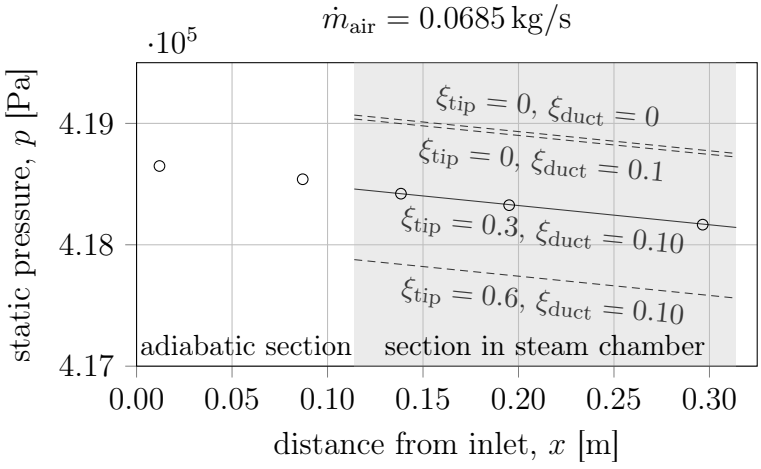

Figure P.2: Measured static pressure data points (circles) along the internally finned adiabatic section and section within the steam chamber (no heating) compared to simulation results for varying ξ_{tip} and ξ_{duct} for $\dot{m}_{\text{air}} = 0.0685\,\text{kg/s}$.

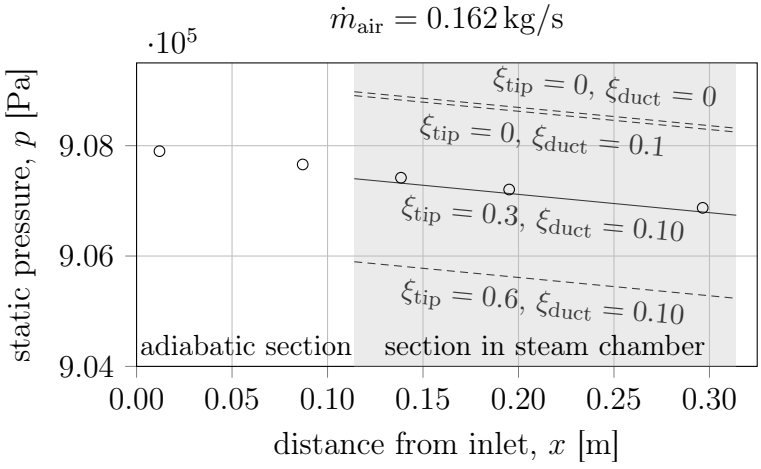

Figure P.3: Measured static pressure data points (circles) along the internally finned adiabatic section and section within the steam chamber (no heating) compared to simulation results for varying ξ_{tip} and ξ_{duct} for $\dot{m}_{\text{air}} = 0.162\,\text{kg/s}$.

Stellenbosch University https://scholar.sun.ac.za

P.2 Temperature distribution within fins

The contour plots comparing the simulated temperature profiles along the fin center in the heated section are provided for all flow rates investigated under heating in chapter 4.

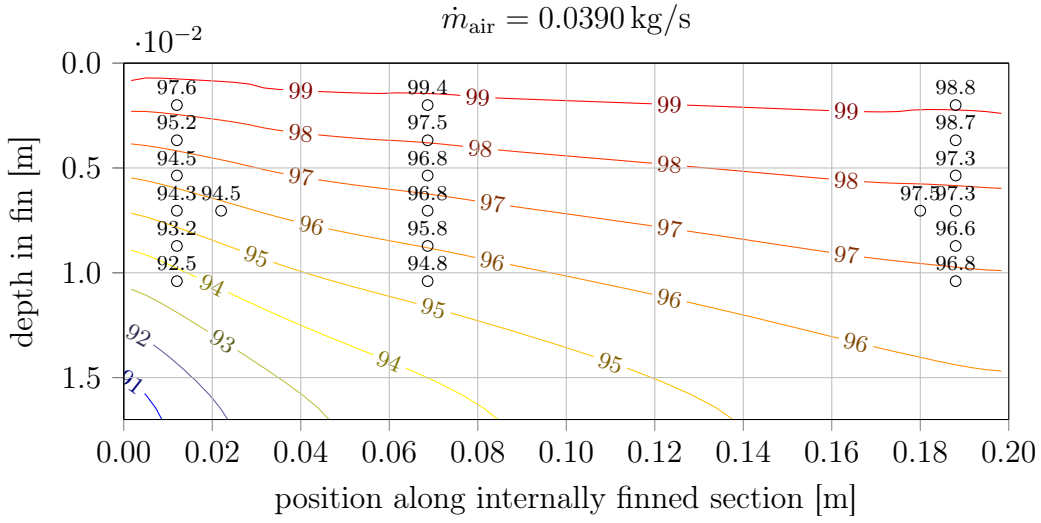

Figure P.4: Contour plot of simulated temperature profile along fin center in heated section for $\dot{m}_{\text{air}} = 0.0390\,\text{kg/s}$. The y-axis shows the depth in the fin with 0 being the outer surface exposed to the steam. Experimental results are shown above the respective black circles, indicating the position of the measurements.

Stellenbosch University https://scholar.sun.ac.za

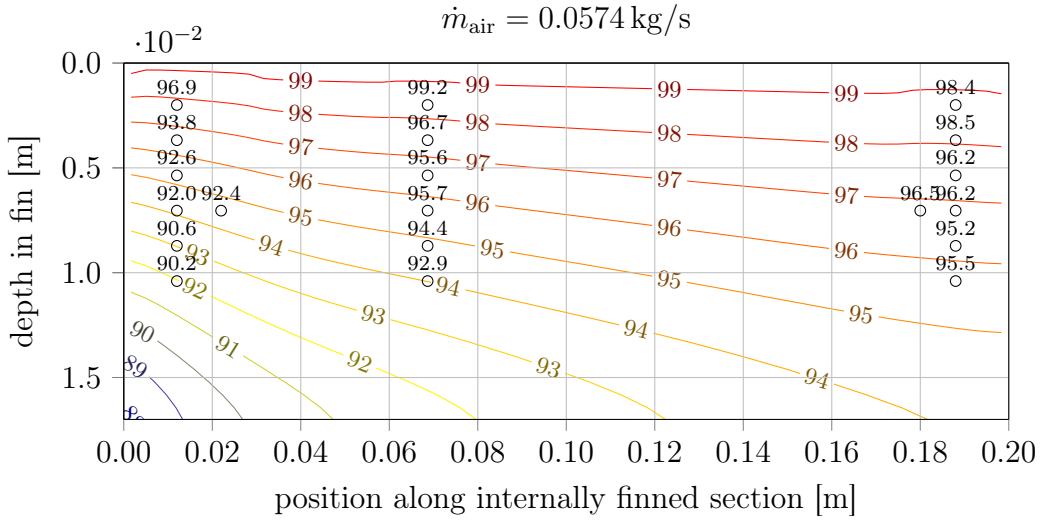

Figure P.5: Contour plot of simulated temperature profile along fin center in heated section for $\dot{m}_{\text{air}} = 0.0574\,\text{kg/s}$. The y-axis shows the depth in the fin with 0 being the outer surface exposed to the steam. Experimental results are shown above the respective black circles, indicating the position of the measurements.

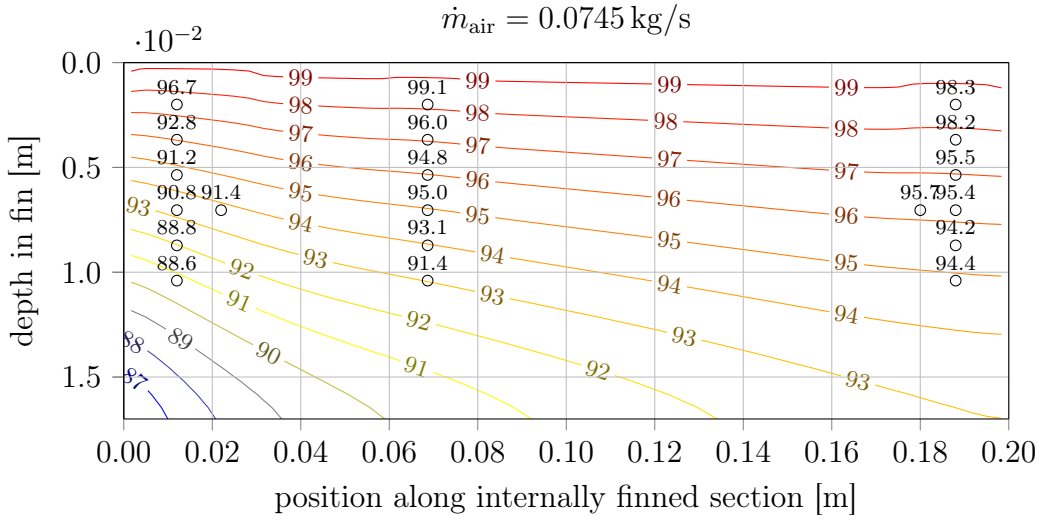

Figure P.6: Contour plot of simulated temperature profile along fin center in heated section for $\dot{m}_{\text{air}} = 0.0745\,\text{kg/s}$. The y-axis shows the depth in the fin with 0 being the outer surface exposed to the steam. Experimental results are shown above the respective black circles, indicating the position of the measurements.

Stellenbosch University https://scholar.sun.ac.za

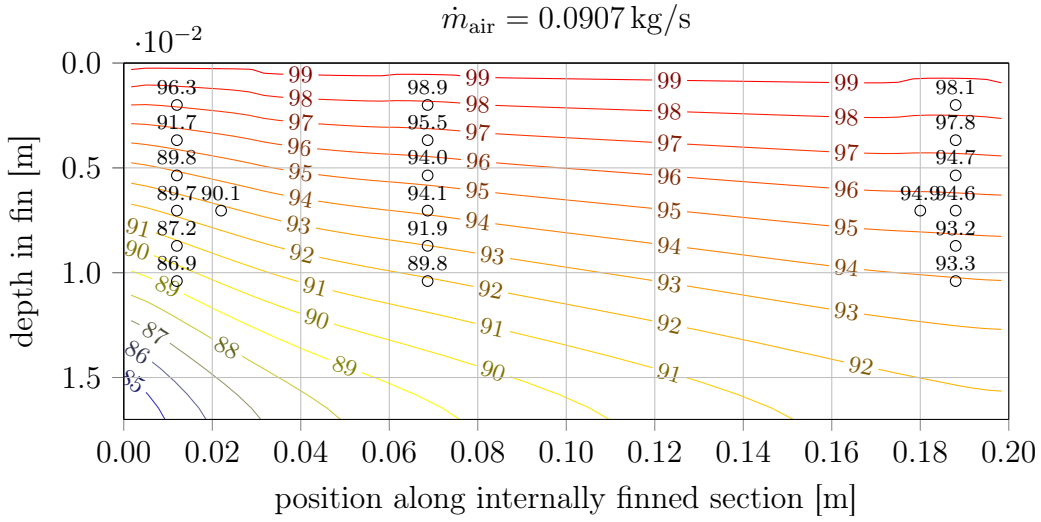

Figure P.7: Contour plot of simulated temperature profile along fin center in heated section for $\dot{m}_{\text{air}} = 0.0907\,\text{kg/s}$. The y-axis shows the depth in the fin with 0 being the outer surface exposed to the steam. Experimental results are shown above the respective black circles, indicating the position of the measurements.

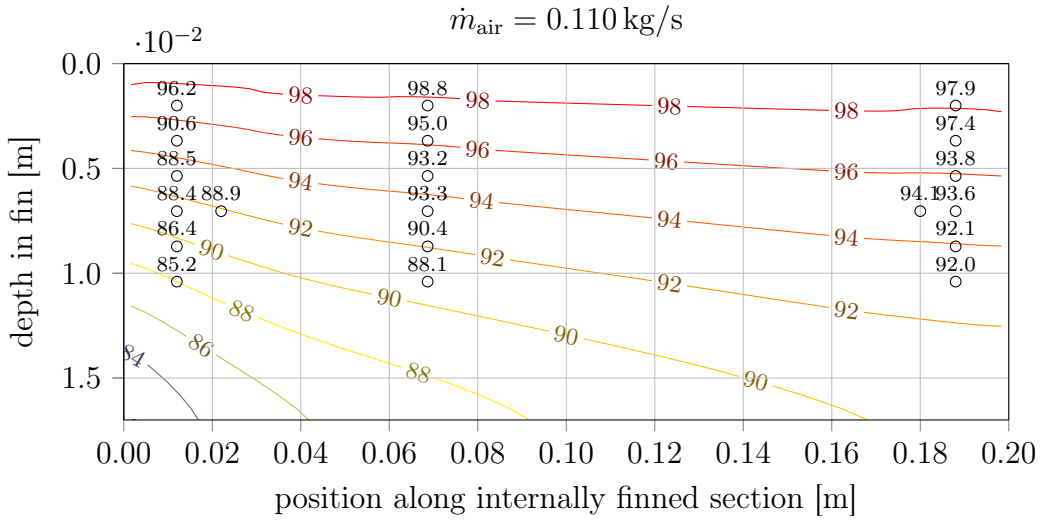

Figure P.8: Contour plot of simulated temperature profile along fin center in heated section for $\dot{m}_{\text{air}} = 0.110\,\text{kg/s}$. The y-axis shows the depth in the fin with 0 being the outer surface exposed to the steam. Experimental results are shown above the respective black circles, indicating the position of the measurements.

Stellenbosch University https://scholar.sun.ac.za

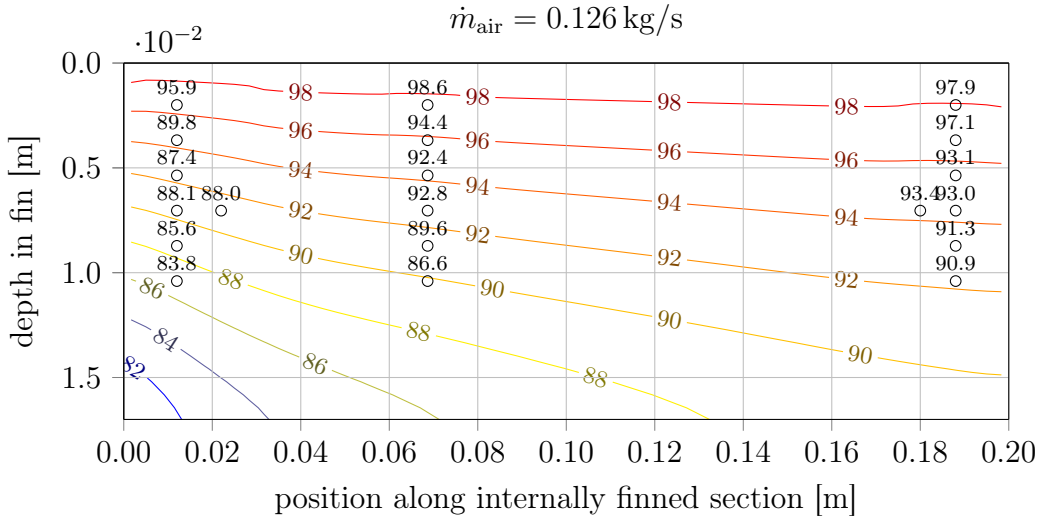

Figure P.9: Contour plot of simulated temperature profile along fin center in heated section for $\dot{m}_{\text{air}} = 0.126\,\text{kg/s}$. The y-axis shows the depth in the fin with 0 being the outer surface exposed to the steam. Experimental results are shown above the respective black circles, indicating the position of the measurements.

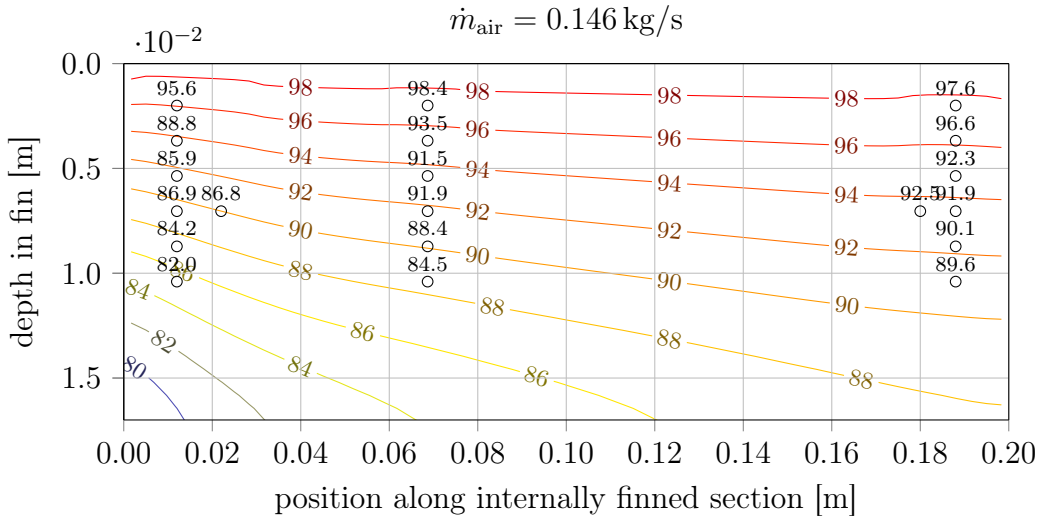

Figure P.10: Contour plot of simulated temperature profile along fin center in heated section for $\dot{m}_{\text{air}} = 0.146\,\text{kg/s}$. The y-axis shows the depth in the fin with 0 being the outer surface exposed to the steam. Experimental results are shown above the respective black circles, indicating the position of the measurements.

Stellenbosch University https://scholar.sun.ac.za

Appendix Q

Factors Affecting Air Outlet Temperature Measurement

With an experimental setup numerous features influence the observed outcome that are not represented in a theoretical model. This chapter discusses such discrepancies between the presented simulation model and the experimental setup to either discard the effects as negligible or attempt to broadly quantify the potential impact. Naturally, such impacts tend to be of non-trivial nature and remain therefore as estimated quantities. Figure Q.1 illustrates a section through the experimental test setup.

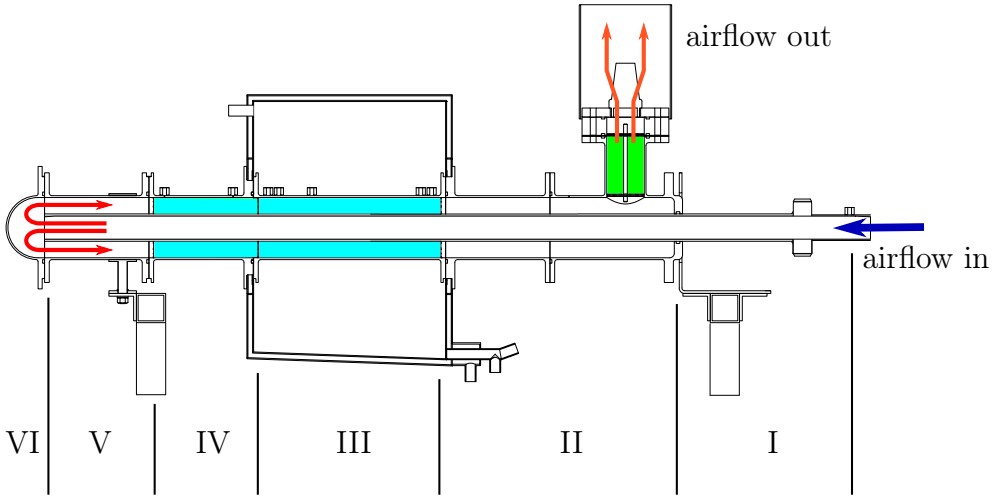

Figure Q.1: Section through experimental setup

Q.1 Expanding air flow with cooling effect

After exiting the heated internally finned section within the steam compartment, the pressurized air flow is rejected to ambient via a silencer. The flange holding

Stellenbosch University https://scholar.sun.ac.za

the silencer is mounted onto a flange on which a set of three thermocouples is mounted to measure the air flow temperature. The spatial proximity from the temperature measurement to the silencer poses a risk that cooling of the air flow under expansion to ambient pressure — as it passes through the silencer — could, via axial thermal conduction through the flanges in upstream direction, influence the thermocouple readings via stem conduction.

Two 2.5 mm thick silicone gaskets were mounted above and below the flange holding the thermocouples to reduce axial conduction. Above and below the flange, the temperature of the flange was recorded using additional thermocouples. No temperature gradient over the 15 mm thick stainless steel flange was observed. Additionally, reading the air outlet temperature after exiting at ambient pressure, using a handhold device, suggested similar readings to the permanently mounted thermocouples. It can be concluded that a temperature drop over expansion is not of significant magnitude and upstream axial conduction is not observed.

Q.2 Heat transfer in annular region

Q.2.1 Cooling of air flow in outer region

The annular region towards the spike tip is adiabatic as it is in the insulated region of the experimental setup. On the other hand, the annular space downstream the steam compartment exposes the hot air to heat loss towards the inner tube (and the air flow therein). For fully developed conditions, predictions of heat transfer are straightforward. Here, however, initially the air flow is expanding out of the finned section into the annular space. There, the air flow departs from the concentric counter-flow pattern and is directed into a perpendicular flow direction towards the exhaust silencer.

To establish an idea of the magnitude of heat transfer occurring between the annulus and the inner tube, a brief analysis is conducted assuming fully developed flow and temperature profile conditions in a conventional concentric annulus. With the annulus' outer wall being adiabatic, the convection heat transfer coefficient to the inner tube can be computed with a conventional Nusselt number equation for turbulent duct flow (as derived in chapter 2):

$$Nu = 0.0215 Pr^{0.5} Re^{0.8}. \tag{Q.1}$$

The resulting temperature drop in the air stream over a length of the experiment's annular space would be in the range of 0.8 K to 1.25 K, for the highest and the lowest flow rate, respectively. Higher local Nusselt numbers, particularly at the exit of the rectangular ducts or in the region where the air flow begins to flow across the inner tube, rather than along it, can be expected and would lead to increased temperature loss.

Stellenbosch University https://scholar.sun.ac.za

Q.2.2 Heating of inlet air flow

As outlined in the previous sub-section (Q.2.1), the heat transfer from the outer air-flow to the inner, in the limited length of the annular segment (II) is challenging to predict accurately. The heating of the air flow within the inner tube assumes a constant wall surface temperature, circumferentially and axially, equivalent to the inner tube temperature exiting the finned section. The heating of the inner air stream is similar in magnitude to the expected cooling of the outer air stream with 0.7 K to 1.3 K, depending on the flow rate.

Q.3 Radial heat transfer through inner tube in finned section

Within the internally finned section the inner tube is heated through convective heat transfer from the air stream in the rectangular ducts. The simulation model does not consider thermal conduction, in the radial direction, between the fin tips and the inner tube. Neither is thermal convection in the narrow slot between the inner tube's wall an the fin tips considered.

Omitting the conductive heat transfer is confirmed as a suitable assumption through visual inspection of the inner tube after conduction a series of experiments: Where the inner tube's outer diameter was not reduced from 30 mm to 29.6 mm, with the aim to permit concentric positioning within the adiabatic internally finned section, scratch marks are visible.The surface located within the heated section remained without scratches or other marks of surface to surface contact.

Q.4 Axial conduction over flanges

The flanges connecting segments of the experimental setup are subject to axial conduction. Where relevant, these flanges have been equipped with silicone gaskets to reduce conduction. In order to quantify the axial conduction, flange temperatures up- and downstream of some of the flanges are measured.

Knowing silicone's thermal conductivity of $k = 0.02\,\mathrm{W/m\,K}$ and the gasket thickness of $t_{\mathrm{gasket}} = 2.5\,\mathrm{mm}$ the heat transfer can be calculated as

$$\dot{Q}_{\mathrm{cond}} = A_{\mathrm{gasket}} \frac{k_{\mathrm{gasket}}}{t_{\mathrm{gasket}}} (T_{\mathrm{flange},1} - T_{\mathrm{flange},2}) \tag{Q.2}$$

where $T_{\mathrm{flange},1}$ and $T_{\mathrm{flange},2}$ are the temperatures of the two flange sides under consideration. With the test section completely wrapped in insulation wool, the effect of conductive heat transfer from a section to another

$$\dot{Q} = \dot{m}_{\mathrm{air}} c_{\mathrm{p}} \Delta T_{\mathrm{air}} \tag{Q.3}$$

Stellenbosch University https://scholar.sun.ac.za

This may occur as a cooling effect through conduction to the mounting structure or a heating effect when conducting from the heated section to a neighboring one.

The thermal conduction upstream the heated section translates to a heating of the air flow of 0.2 K to 0.7 K, the conduction over the flange downstream the steam compartment amounts to 0.1 K to 0.3 K, while the heat loss over the stainless steel mounting bracket has a cooling effect of 0.0 K to 0.1 K. With all values listed, higher heating/cooling effects correspond to lower flow rates.

Summarizing the aforementioned effects in Table Q.1 suggests that the most notable effects do somewhat cancel one another out, not influencing the measured results significantly. In average, the sum of the quantified effects suggests that the air outlet temperature is underestimated by about 0.3 K.

Table Q.1: Impact of quantified heat flows onto air temperature measurement

$\dot{m}_{\text{air}}$ [kg/s]	$\Delta T_{\text{annulus}}$ [K]	$\Delta T_{\text{flange,upst.}}$ [K]	$\Delta T_{\text{flange,downst.}}$ [K]	$\Delta T_{\text{flange,mount}}$ [K]	ΔT_{sum} [K]
0.0390	−1.2	0.73	0.27	−0.065	−0.29
0.0574	−1.0	0.52	0.21	−0.038	−0.32
0.0745	−0.87	0.41	0.18	−0.026	−0.31
0.0907	−0.80	0.34	0.16	−0.020	−0.32
0.110	−0.73	0.28	0.13	−0.016	−0.33
0.126	−0.68	0.25	0.12	−0.013	−0.33
0.146	−0.68	0.22	0.11	−0.011	−0.37

Q.5 Atmospheric pressure

The atmospheric pressure data is collected from an online data base, providing access to the readings of the University's barometric pressure measurements. An average data point for the duration of the experiment is included into the simulation input file. The deviation in atmospheric pressure over the course of an experiment tends to be marginal compared to the error range of the gauge pressure sensor.

Q.6 Steam temperature

To avoid an increase in steam system pressure (and rapid depletion of the steam generator's water tank) steam production is rate is manually adjusted to each air flow rate. As a result, the amount of excess steam exiting the test chamber is of similar magnitude throughout the steady state experiments. A thermocouple is inserted into the steam compartment to read the steam temperature. The

Stellenbosch University https://scholar.sun.ac.za

readings, listed in Table Q.2, confirm steady steam temperatures throughout the duration of the experiment.

Table Q.2: Steam temperature T_{steam} for varying air flow rates

$\dot{m}_{\text{air}}$	[kg/s]	0.0390	0.0574	0.0745	0.0907	0.110	0.126	0.146
T_{steam}	[°C]	99.82	99.75	99.78	99.78	99.85	99.93	99.84

The stability of the steam temperature, T_{steam}, suggests that varying steam flow rates do not significantly impact on the steam temperature. The observed steam temperatures correlate well with the elevation of Stellenbosch at approximately 120 m above sea level.

Q.7 Change in ambient conditions

The pressurized air supply tank is located outside the building and is exposed to ambient conditions. The air supply line, connecting the test setup with the tank, equally runs outside the building over a length of approximately 30 m. This pipe is not insulated to ambient except a layer of paint.

Changes in ambient conditions, such as clouds or wind, have notable impact on the supply air temperature for the reason that reaching thermal steady state conditions may require several minutes to achieve. Throughout all readings attention has been paid to taking readings under steady, stable conditions.

Figure Q.2 shows the air inlet temperature over time from measurement start for a range of readings recorded during commissioning work.

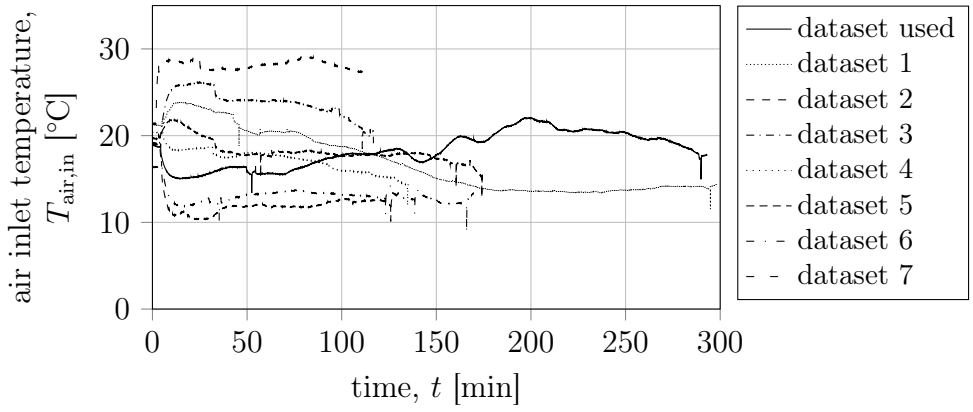

Figure Q.2: Measurement of the air inlet temperature,$T_{\text{air,in}}$, over time showing the variability of air temperature, influenced by ambient conditions. Spikes in the readings indicate temporary turning off of air flow.

Stellenbosch University https://scholar.sun.ac.za

It is notable that all data sets begin at around 20 °C ± 3 °C with the zero reading, thus representing room temperature.

Q.8 Heating of air in areas of single-node pressure drop computation

The pressure drop in the internally finned section upstream of the test segment is computed in a single node. With axial conduction across the flange being observed, heat transfer occurs. $\dot{Q} = \dot{m} c_\mathrm{p} \Delta T$ shows that the heating effect is in the order of ≤1.0 °C, thus leading to negligible error through flow expansion.

Q.9 Temperature measurement error through stagnation effect

Where a thermocouple is inserted into an air stream of high velocity, stagnation effects of the impinging air flow can lead to temperature readings exceeding the actual air temperature. As the air flow accelerates again, passing the thermocouple, a countering cooling effect occurs. These effects, for lower air speeds, tend to cancel each other out. Taking the compressibility effects into account, typically becomes relevant from Mach numbers of $M \geq 0.3$. During the experiments, the highest air flow rate is experienced in the inner tube, where $M = 0.1$ is not exceeded.

The stagnation temperature can be computed as

$$T_0 = T_\mathrm{air} + \frac{u^2}{2 c_\mathrm{p}}, \tag{Q.4}$$

where u is the air flow velocity. With a peak inlet air velocity of $u = 29\,\mathrm{m/s}$ the ΔT attributed the stagnation effect is 0.4 K. Ignoring the countering recovery effects, a measurement deviation of 0.4 K is of the same order of magnitude experienced with other impacts on the measured temperature discussed above.

Q.10 Oxidization of specimen

Prior to commissioning of the experimental apparatus the surfaces were machined and bland aluminium. Over the extended period of manufacturing and assembling of all components for the test setup, oxidization of the parts may have occurred.

After exposing the heated section to steam numerous times, the surface showed some slight discoloring of gray tone. These oxide and residue layers may have impact on the measurement by providing thermal resistance. Due to the numerous fittings for static pressure measurements as well as thermocouple

Stellenbosch University https://scholar.sun.ac.za

sensors being attached with adhesive to the internally finned section, polishing of the surface is not possible. The impact is considered minor.

Stellenbosch University https://scholar.sun.ac.za

Stellenbosch University https://scholar.sun.ac.za

Appendix R

System Pressure Drop Approximation

Based on the design point SCRAP receiver introduced in chapter 2 a brief system pressure drop analysis is conducted with the aim to understand the total losses and bring the pressure drop within a spike into relation to the remaining system losses.

Generally, pressure drop due to a flow obstacle such as pipe friction or a valve can be computed as

$$\Delta p = \xi \frac{\rho u^2}{2}. \tag{R.1}$$

where various friction coefficients, ξ, are introduced in the following subsections. These contain additional spike-related pressure drops for the inlet into the inner tube and outlet out of the internally finned outer tube. Further, ducting and valves in a simple air flow network, linking a turbine to the receiver, are considered.

Figure R.1 introduces a block diagram of a Brayton cycle CSP plant with introducing relevant pressure drops. The simple network contains ducting up a tower to the receiver and additional valves permitting bypass operation. Losses attributed to the turbine side are not considered, assuming a turbine with external combustion chamber.

R.1 Plant dimension assumptions

The dimensions of the SCRAP receiver are as shown in Table R.1.

A receiver with the thermal rating of 36.7 $\mathrm{MW_t}$[1] requires a mass flow rate of

[1] adjusted from initial assumption of 29 $\mathrm{MW_t}$ for increased flux on aperture of $\dot{q}''_{\mathrm{rad}} = 1.27\,\mathrm{MW/m^2}$)

Stellenbosch University https://scholar.sun.ac.za

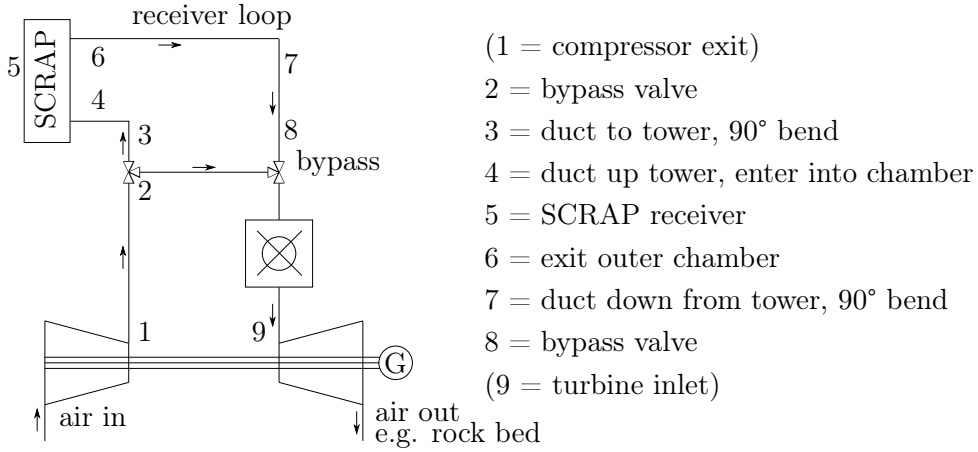

Figure R.1: Block diagram of a Brayton cycle CSP plant with pressurized air receiver and combustion chamber.

Table R.1: SCRAP receiver dimension assumptions

element	unit	value
outer chamber/sphere radius	[m]	2
spike length	[m]	1.3
receiver thermal rating	[MW_t]	29
tower height	[m]	82
air pressure	[MPa]	1.0
inlet temperature	[°C]	300
outlet temperature	[°C]	800
pipe diameter all ducts	[m]	1.0 or 2.0

approximately 65 kg/s when computing the mass flow rate using the following

$$\dot{m} = \frac{\dot{Q}}{\int_{T_{\text{in}}}^{T_{\text{out}}} c_{\text{p}} d\text{T}} \tag{R.2}$$

with air being heated from 300 °C to 800 °C.

R.2 System pressure drop

The system pressure drop is composed of the pressure drop within a SCRAP receiver as well as the pressure drop in the remainder of a CSP plant. Both contributors are approximated in the following.

Stellenbosch University https://scholar.sun.ac.za

R.2.1 Pressure drop spike

The pressure drop over a single spike is combined by a spike entry loss (a), the simulation of the spike itself (b) as well as the air exiting into the outer chamber (c).

Table R.2: Additional spike pressure loss equations

element	description	calculation[1]	
(a)	$\xi_A = 1$	$\Delta P = \xi_A \frac{\rho u^2}{2} = 1 \frac{6.1 \times 7^2}{2}$ Pa	= 149 Pa
(b)	spike model	ΔP	= 3799 Pa
(c)	$f_1/f_2 \to 0$	$\Delta P = (1 - f_1/f_2) \frac{\rho u^2}{2} = 1 \frac{3.2 \times 5.68^2}{2}$ Pa	= 102 Pa
	total spike	$\sum \Delta P$	= 4050 Pa

[1] Assumptions for ξ based on VDI (2010)

R.2.2 Pressure drop receiver system

The pressure drop calculation for a simple receiver system such as shown in Figure R.1 is introduced in this section. Table R.3 lists the pressure losses including the equations used to compute these. Following is Table R.4, where the assumptions for the various friction coefficients are shown and the pressure drops are computed. To permit comparison two pipe diameters are compared, one of 1.0 m and the other of 2.0 m. The two diameters are selected with the purpose to assist building an understanding of sensitivities, rather than claiming to be providing an ideal solution.

To compute the pressure drops, air density at 300 °C is approximately 6.1 kg/m^3 and at 800 °C about 3.3 kg/m^3 for an ideal gas under 10 bar pressure. This results in approximate flow velocities of 11.1 m/s and 20.34 m/s for the pipes with 1.0 m diameter and 2.75 m/s and 5.09 m/s for the pipes with 2.0 m diameter.

Table R.4 illustrates that the ducting dimensions have significant influence on the system pressure drop and the pipe-induced pressure drop can in fact dominate the total pressure drop. One can also note that the largest contributors are the flow up and down the tower, which is of interest when comparing solutions where a turbine may be mounted on top of the tower.

Stellenbosch University https://scholar.sun.ac.za

Table R.3: Pressure losses introduction

element	description	equation
①	compressor exit (not considered here)	-
②	bypass valve	$\Delta P = \xi_{\mathrm{V}} \frac{\rho u^2}{2}$
③	duct to tower and	$\Delta P = f_{\mathrm{D}} \frac{L}{D} \frac{\rho u^2}{2}$
③	bent up tower	$\Delta P = \xi_{\mathrm{U}} \frac{\rho u^2}{2}$
④	duct up tower and	$\Delta P = f_{\mathrm{D}} \frac{L}{D} \frac{\rho u^2}{2}$
④	enter into inner chamber	$\Delta P = (1 - f_1/f_2) \frac{\rho u^2}{2}$
⑤	Spike simulation	see model
⑥	exit of outer chamber	$\Delta P = \xi_{\mathrm{A}} \frac{\rho u^2}{2}$
⑦	duct down tower and	$\Delta P = f_{\mathrm{D}} \frac{L}{D} \frac{\rho u^2}{2}$
⑦	bent towards turbine	$\Delta P = \xi_{\mathrm{U}} \frac{\rho u^2}{2}$
⑧	duct to power block and	$\Delta P = f_{\mathrm{D}} \frac{L}{D} \frac{\rho u^2}{2}$
⑧	bypass valve	$\Delta P = \xi_{\mathrm{V}} \frac{\rho u^2}{2}$
⑨	turbine inlet (not considered here)	-

Stellenbosch University https://scholar.sun.ac.za

Table R.4: Pressure losses calculation

	assumptions[1]	equation	$D = 0.5$ m	$D = 1.0$ m
②	$\xi_V = 0.6$	$\Delta P = \xi_V \frac{\rho u^2}{2}$	= 342 Pa	= 21 Pa
③	$f_D = 0.3164\, Re^{-0.25}$ = 0.01; L = 10m	$\Delta P = f_D \frac{L}{D} \frac{\rho u^2}{2}$	= 44 Pa	= 1.6 Pa
③	$r_{bent}/d_{tube} = 1$, $\xi_U = 0.2$	$\Delta P = \xi_U \frac{\rho u^2}{2}$	= 114 Pa	= 7.1 Pa
④	$f_D = 0.3164\, Re^{-0.25}$ = 0.01; L = 82m	$\Delta P = f_D \frac{L}{D} \frac{\rho u^2}{2}$	= 361 Pa	= 13 Pa
④	$f_1/f_2 \to 0$	$\Delta P = (1 - f_1/f_2) \frac{\rho u^2}{2}$	= 569 Pa	= 36 Pa
⑤	Spike simulation		= 3799 Pa	= 3799 Pa
⑥	$\xi_A = 1$	$\Delta P = \xi_A \frac{\rho u^2}{2}$	= 1052 Pa	= 66 Pa
⑦	$f_D = 0.3164\, Re^{-0.25}$ = 0.01; L = 82m	$\Delta P = f_D \frac{L}{D} \frac{\rho u^2}{2}$	= 743 Pa	= 28 Pa
⑦	$r_{bent}/d_{tube} = 1$, $\xi_U = 0.2$	$\Delta P = \xi_U \frac{\rho u^2}{2}$	= 210 Pa	= 13 Pa
⑧	$f_D = 0.3164\, Re^{-0.25}$ = 0.01; L = 10m	$\Delta P = f_D \frac{L}{D} \frac{\rho u^2}{2}$	= 91 Pa	= 3.4 Pa
⑧	$\xi_V = 0.6$	$\Delta P = \xi_V \frac{\rho u^2}{2} =$	= 631 Pa	= 39 Pa
	total	$\sum \Delta P$	= 7957 Pa = 80 mbar	= 4028 Pa = 40 mbar

[1] Assumptions for ξ based on VDI (2010)

Stellenbosch University https://scholar.sun.ac.za

Stellenbosch University https://scholar.sun.ac.za

List of References

Aora-Solar (2011). Aora-Solar website. Last accessed March 2014.
Available at: http://www.aora-solar.com/

Ávila-Marín, A.L. (2011). Volumetric receivers in Solar Thermal Power Plants with Central Receiver System technology: A review. *Solar Energy*, vol. 85, no. 5, pp. 891–910. ISSN 0038-092X.
Available at: http://dx.doi.org/10.1016/j.solener.2011.02.002

Behnia, M., Parneix, S. and Durbin, P. (1997). Accurate modeling of Impinging Jet heat transfer. *Center Turbulence Research Annual Research Briefs*, pp. 149–164. Last accessed March 2014.

Bellard, D., Ferriere, A., Pra, F. and Couturier, R. (2012). Experimental Characterization of a High-Temperature Pressurized Air Solar Absorber for the PEGASE Project. In: *SolarPACES Conference*. Marrakech.

Bischof-Niemz, T. and Fourie, R. (2016). *Cost of new Power Generators in South Africa - Comparative Analysis based on recent IPP Announcements*. CSIR, Pretoria. Last accessed November 2016.

Blanco, M., Mutuberria, A., Monreal, A. and Albert, R. (2011). Results of the Empirical Validation of Tonatiuh at Mini-Pegase CNRS-PROMES facility. In: *SolarPACES Conference*, pp. 1–8. Granada.

Blanco, M.J., Mutuberria, A., Garcia, P., Gastesi, R. and Martin, V. (2009). Preliminary Validation of Tonatiuh. In: *SolarPACES Conference*. Berlin.

Blanco, M.J., Mutuberria, A. and Martinez, D. (2010). Experimental Validation of Tonatiuh using the Plataforma Solar de Almería Secondary Concentrator Test Campaign Data. In: *SolarPACES Conference*. Perpignan.

Blasius, H. (1912). Das Ähnlichkeitsgesetz bei Reibungsvorgängen. Last accessed November 2014.

Bode, S.-J. and Gauché, P. (2012). Review of Optical Software for use in Concentrating Solar Power Systems. In: *SASEC 2012*, pp. 1–8. Stellenbosch.

Bono, R.J. (2011). DOME (4.80ar01). Last accessed December 2013.
Available at: http://www.antiprism.com/other/dome/dome-4.80ar01_win.zip

Stellenbosch University https://scholar.sun.ac.za

BSI (1984). *British Standard - Measurement of fluid flow in closed conduits*. British Standard Institution, Milton Keynes.

Buck, R., Bräuning, T., Denk, T., Pfänder, M., Schwarzbözl, P. and Tellez, F. (2002). Solar-Hybrid Gas Turbine-based Power Tower Systems (REFOS). *Journal of Solar Energy Engineering*, vol. 124, no. 1, p. 2. ISSN 01996231.
Available at: `http://dx.doi.org/10.1115/1.1445444`

Çengel, Y.A. and Ghajar, A.J. (2011). *Heat and Mass Transfer: Fundamentals and Applications*. Fourth edi edn. McGraw-Hill, Inc., New York. ISBN 978-007-131112-0.

DoE (2016). *Facts Sheet - Bid Window 1: Coal Procurement Programme*. Department of Energy, Pretoria.

Duffie, J.A. and Beckman, D.A. (2006). *Solar Engineering of Thermal Processes*. 3rd edn. John Wiley Sons Inc., Hoboken.

FESTO (2016). *Filter regulators MS-LFR , MS series Filter regulators MS-LFR , MS series*. FESTO.

Figliola, R.S. and Beasley, D.E. (2006). *Theory and Design for Mechanical Measurements*. 4th edn. John Wiley Sons, Inc., Hoboken.

Firstrate (2016). FST800-211 Universal Industrial Pressure Sensor.

Freescale (2008). *Freescale Semiconductor MPX2050*. Freescale semiconductor, Tempe.

Garbrecht, O., Al-Sibai, F., Kneer, R. and Wieghardt, K. (2012). Numerical Investigation of a New Molten Salt Central Receiver Design. In: *SolarPACES*. Marrakech.

Gnielinski, V. (2010). G7 Heat Transfer in Cross-flow Around Single Rows of Tubes and Through Tube Bundles. In: *VDI Heat Atlas*, pp. 725–30. Springer Berlin Heidelberg.

Grange, B., Ferrière, A., Bellard, D., Vrinat, M., Couturier, R., Pra, F. and Fan, Y. (2011). Thermal Performances of a High Temperature Air Solar Absorber Based on Compact Heat Exchange Technology. *Journal of Solar Energy Engineering*, vol. 133, no. 3, p. 031004. ISSN 01996231.
Available at: `http://dx.doi.org/10.1115/1.4004356`

Greene, G., Finfrock, C. and Irvine, T. (2000). Total Hemispherical Emissivity of Oxidized Inconel 718 in the Temperature Range 300 – 1000 °C. *Experimental Thermal and Fluid Science*, vol. 22, no. 3-4, pp. 145–153. ISSN 08941777.
Available at: `http://dx.doi.org/10.1016/S0894-1777(00)00021-2`

Greene, G.A. and Finfrock, C.C. (2001). Oxidation of Inconel 718 in Air at High Temperatures. *Oxidation of Metals*, vol. 55, pp. 505–521.
Available at: `http://dx.doi.org/10.1023/A:1010359815550`

Stellenbosch University https://scholar.sun.ac.za

Heller, P. (2010). SOLHYCO: Solar-Hybrid Power and Cogeneration Plants. Tech. Rep. 019830, DLR, Stuttgart. Last accessed March 2012.

Heller, P., Pfänder, M., Denk, T., Tellez, F., Valverde, A., Fernandez, J. and Ring, A. (2006). Test and Evaluation of a Solar Powered Gas Turbine System. *Solar Energy*, vol. 80, no. 10, pp. 1225–1230. ISSN 0038092X.
Available at: http://dx.doi.org/10.1016/j.solener.2005.04.020

Hischier, I., Leumann, P. and Steinfeld, A. (2012). Experimental and Numerical Analyses of a Pressurized Air Receiver for Solar-Driven Gas Turbines. *Journal of Solar Energy Engineering*, vol. 134, no. 2, p. 021003. ISSN 0199-6231.
Available at: http://dx.doi.org/10.1115/1.4005446

Hoffschmidt, B. (1997). *Vergleichbare Bewertung verschiedener Konzepte Volumetrischer Strahlungsempfaenger*. DLR, Aachen. ISBN 1434-8454.

Hofmann, A., Schenk, C. and Uhlig, R. (2009). Optical Quartz Glass Windows for High Concentrated Thermal Power Plants. In: *SolarPACES Conference*. SolarPACES, Berlin.

Howell, J.R. (2011). A Catalog of Radiation Heat Transfer Configuration Factors. Tech. Rep., The University of Texas at Austin, Austin. Last accessed November 2013.

Huang, L. and Shah, R. (1992). Assessment of Calculation Methods for Efficiency of Straight Fins of Rectangular Profile. *International Heat and Fluid Flow*, vol. 13, no. 3, pp. 282–293.
Available at: http://dx.doi.org/10.1016/0142-727X(92)90042-8

Idelchik, I.E. (1986). *Handbook of Hydraulic Resistance - Coefficients of Local Resistance and of Friction*. 2nd edn. Hemisphere Publishing Corporation, Moscow. ISBN 0-89116-284-4.

Jensch, A., Meschke, F. and Uhlig, R. (2012). Pressurized Ceramic Plate Receiver for High Outlet Temperatures. In: *SolarPACES Conference*. Marrakech.

Jones, O.J. (1976). An Improvement in the Calculation of Turbulent Friction in Rectangular Ducts. *Journal of Fluids Engineering*, vol. 98, pp. 173–181.
Available at: http://dx.doi.org/10.1115/1.3448250

Karni, J., Kribus, A., Doron, P., Rubin, R., Fiterman, A. and Sagie, D. (1997). The DIAPR : A high-pressure, high-temperature solar receiver. *Journal of solar energy engineering*, vol. 119, no. 1, pp. 74–78. ISSN 0199-6231. Last accessed March 2014.
Available at: http://cat.inist.fr/?aModele=afficheN&cpsidt=2589775

Karni, J., Kribus, A., Rubin, R. and Doron, P. (1998). The Porcupine: A Novel High-Flux Absorber for Volumetric Solar Receivers. *Journal of Solar Energy Engineering*, vol. 120, no. 2, p. 85. ISSN 01996231.
Available at: http://dx.doi.org/10.1115/1.2888060

Stellenbosch University https://scholar.sun.ac.za

Kays, W., Crawford, M. and Weigand, B. (2005). *Convection Heat and Mass Transfer*. 4th edn. McGraw-Hill, New York.

Keysight Technologies (2014). *Keysight 34970A Data Acquisition / Switch Unit Family*. Keysight Technologies.

Korzynietz, R., Brioso, J.A., Río, A., Quero, M., Gallas, M., Uhlig, R., Ebert, M., Buck, R. and Teraji, D. (2016). Solugas âĂŞ Comprehensive analysis of the solar hybrid Brayton plant. *Solar Energy*, vol. 135, pp. 578–589. ISSN 0038-092X.
Available at: `http://dx.doi.org/10.1016/j.solener.2016.06.020`

Korzynietz, R., Quero, M. and Uhlig, R. (2012). SOLUGAS — Future Solar Hybrid Technology. In: *SolarPACES Conference*. Marrakech.

Kribus, A., Doron, P., Rubin, R., Karni, J., Reuven, R., Duchan, S. and Taragan, E. (1999). A Multistage Solar Receiver:: The Route To High Temperature. *Solar Energy*, vol. 67, no. 1, pp. 3–11. ISSN 0038092X.
Available at: `http://dx.doi.org/10.1016/S0038-092X(00)00056-6`

Kribus, A., Doron, P., Rubin, R., Reuven, R., Taragan, E., Duchan, S. and Karni, J. (2001). Performance of the Directly-Irradiated Annular Pressurized Receiver (DIAPR) Operating at 20 bar and 1200 °C. *Journal of Solar Energy Engineering*, vol. 123, no. 1, p. 10. ISSN 01996231.
Available at: `http://dx.doi.org/10.1115/1.1345844`

Kribus, A., Zaibel, R., Carey, D., Segal, A. and Karni, J. (1998). A solar-driven combined cycle power plant. *Solar Energy*, vol. 62, no. 2, pp. 121–129. ISSN 0038092X.
Available at: `http://dx.doi.org/10.1016/S0038-092X(97)00107-2`

Kröger, D.G. (2004). *Air-cooled Heat Exchangers and Cooling Towers*. 1st edn. University of Stellenbosch, Stellenbosch. ISBN 978-1593700195.

Kröger, D.G. (2008). Spiky Central Receiver Air Pre-heater (SCRAP). Tech. Rep., University of Stellenbosch, Stellenbosch. Last accessed March 2016.

Kröger, D.G. (2012). SUNSPOT - The Stellenbosch UNiversity Solar POwer Thermodynamic cycle. Tech. Rep., University of Stellenbosch, Stellenbosch. Last accessed October 2015.

Lata, J.M., Rodríguez, M. and de Lara, M.A. (2008). High Flux Central Receivers of Molten Salts for the New Generation of Commercial Stand-Alone Solar Power Plants. *Journal of Solar Energy Engineering*, vol. 130, no. 2, p. 021002. ISSN 01996231.
Available at: `http://dx.doi.org/10.1115/1.2884576`

Lubkoll, M., Harms, T. and Von Backström, T.W. (2016*a*). Introduction to Heat Transfer Test Setup and Manufacturing Process for the SCRAP Receiver. In: *4th Southern African Solar Energy Conference*. SASEC, Stellenbosch. Last accessed November 2016.
Available at: `http://www.sasec.org.za/full-papers/76.pdf`

Stellenbosch University https://scholar.sun.ac.za

Lubkoll, M., Harms, T.M. and Von Backström, T.W. (2016*b*). Introduction of Heat Transfer Test Setup for the SCRAP Receiver. *AIP Conference Proceedings*. In print; last accessed January 2017.

Lubkoll, M., Von Backström, T.W. and Harms, T.M. (2016*c*). Performance Outlook of the SCRAP receiver. *AIP Conference Proceedings*, vol. 1734, no. 030024, pp. 1–7.
Available at: `http://dx.doi.org/10.1063/1.4949076`

Lubkoll, M., Von Backström, T.W., Harms, T.M. and Kröger, D.G. (2015). Initial Analysis on the Novel Spiky Central Receiver Air Pre-heater (SCRAP) Pressurized Air Receiver. *Energy Procedia*, vol. 69, pp. 461–470.
Available at: `http://dx.doi.org/10.1016/j.egypro.2015.03.053`

Lubkoll, M., Von Backström, T.W. and Kröger, D.G. (2014). Survey on Pressurized Air Receiver Development. In: *2nd Southern African Solar Energy Conference 2014*, 0. Port Elizabeth.
Available at: `http://sterg.sun.ac.za/wp-content/uploads/2014/02/501.pdf`

Michelsen, M. and Villadsen, J. (1974). The Graetz Problem With Axial Heat Conduction. *International Journal of Heat and Mass Transfer*, vol. 17, no. 11, pp. 1391–1402. ISSN 00179310.
Available at: `http://dx.doi.org/10.1016/0017-9310(74)90140-9`

MSC (2014). Patran. Version 2014.0.1 64-bit. Last accessed December 2015.

Mutuberria, A., Monreal, A., Blanco, M., Sanchez, M. and Ferriere, A. (2012). Modeling and Structure Deformation Analysis of a Heliostat at Mini-Pegase CNRS-PROMES Facility. In: *SolarPACES Conference*. Marrakech.

Nakatani, H., Osada, T., Kobayashi, K., Watabe, M. and Tagawa, M. (2012). Development of a Concentrated Solar Power Generation System with a Hot-Air Turbine. *Mitsubishi Heavy Industries Technical Review*, vol. 49, no. 1, pp. 1–5. Last accessed May 2013.
Available at: `https://www.mhi.co.jp/technology/review/pdf/e491/e491001.pdf`

Pikley, W.D. (1997). *Petterson's Stress Concentration Factors*. 2nd edn. John Wiley Sons, Inc., New York. ISBN 0-471-53849-3.

Pitz-Paal, R., Botero, N.B. and Steinfeld, A. (2011). Heliostat Field Layout Optimization for High-Temperature Solar Thermochemical Processing. *Solar Energy*, vol. 85, no. 2, pp. 334–343. ISSN 0038092X.
Available at: `http://dx.doi.org/10.1016/j.solener.2010.11.018`

Pritzkow, W.E.C. (1991). Pressure Loaded Volumetric Ceramic Receiver. *Solar Energy Materials*, vol. 24, pp. 498–507.
Available at: `dx.doi.org/10.1016/0165-1633(91)90086-Z`

Stellenbosch University https://scholar.sun.ac.za

Río, A., Korzynietz, R., Brioso, J.A., Gallas, M., Ordóñez, I. and Quero, M. (2015). Soltrec - Pressurized Volumetric Solar Air Receiver Technology. *Energy Procedia*, vol. 69, pp. 360–368. ISSN 1876-6102.
Available at: `http://dx.doi.org/10.1016/j.egypro.2015.03.042`

Roccia, J.P., Piaud, B., Coustet, C., Caliot, C., Guillot, E., Flamant, G. and Delatorre, J. (2012). SOLFAST, a Ray-Tracing Monte-Carlo Software for Solar Concentrating Facilities. *Journal of Physics: Conference Series*, vol. 369, no. 012029. ISSN 1742-6596.
Available at: `http://dx.doi.org/10.1088/1742-6596/369/1/012029`

Romero, M., Buck, R. and Pacheco, J.E. (2002). An Update on Solar Central Receiver Systems, Projects, and Technologies. *Journal of Solar Energy Engineering*, vol. 124, no. 2, p. 98. ISSN 01996231. Last accessed March 2013.
Available at: `http://solarenergyengineering.asmedigitalcollection.asme.org/article.aspx?articleid=1456424`

Romero-Alvarez, M. and Zarza, E. (2007). Concentrating Solar Thermal Power. In: *Handbook of Energy Efficiency and Renewable Energy*, chap. 21, pp. 21–1 – 21–98. Taylor & Francis Group, LLC, Abingdon.

Sawin, J.L., Seyboth, K. and Sverrisson, F. (2016). *Renewables 2016 - Global Status Report*. REN21, Paris. Last accessed December 2016.

Shah, R. and London, A. (1978). *Laminar Flow Forced Convection in Ducts*. Academic Press, Inc., New York.

SMC (2007). *INCONEL alloy 718*. Special Metals Corporation, Huntington.

Solgate Report (2005). SOLGATE Solar Hybrid Gas Turbine Electric Power System - Project Report. Tech. Rep., European Commission, Luxemburg. Last accessed August 2016.
Available at: `https://ec.europa.eu/research/energy/pdf/solgate_en.pdf`

Soo Too, Y.C. and Benito, R. (2013). Enhancing heat transfer in air tubular absorbers for concentrated solar thermal applications. *Applied Thermal Engineering*, vol. 50, no. 1, pp. 1076–1083. ISSN 13594311.
Available at: `http://dx.doi.org/10.1016/j.applthermaleng.2012.06.025`

Stein, W., Kim, J.-S., Burton, A., McNaughton, R., Soo Too, Y.C., McGregor, J., Nakatani, H., Tagawa, M., Osada, T., Okubo, T. and Kobayashi, K. (2010). Design and Construction of a 200 kWe Tower Brayton Cycle Pilot Plant. In: *SolarPACES Conference*. Perpignan.

Stine, W.B. and Geyer, M. (2001). Power From The Sun. Last accessed June 2016.
Available at: `http://www.powerfromthesun.net/book.html`

Vant-Hull, L. (2012). Central Tower Concentrating Solar Power (CSP) Systems. In: Lovegrove, K. and Stein, W. (eds.), *Concentrating Solar Power Technology*, chap. 8, pp. 240–283. Woodhead Publishing, Cambridge.

Stellenbosch University https://scholar.sun.ac.za

VDI (2010). *VDI-Wärmeatlas*. 10th edn. VDI-Verlag, Düsseldorf.

Wang, W., Laumert, B., Xu, H. and Strand, T. (2015). Conjugate heat transfer analysis of an impinging receiver design for a dish-Brayton system. *Solar Energy*, vol. 119, pp. 298–309.
Available at: http://dx.doi.org/10.1016/j.solener.2015.07.013

Wendelin, T., Dobos, A. and Lewandowski, A. (2013). SolTrace : A Ray-Tracing Code for Complex Solar Optical Systems. Tech. Rep., NREL, Golden. Last accessed October 2013.
Available at: http://www.nrel.gov/docs/fy14osti/59163.pdf

White, F. (1991). *Viscous Fluid Flow*. 2nd edn. McGraw-Hill, Inc., New York. ISBN 0-07-069712-4.

Zuckerman, N. and Lior, N. (2006). Jet Impingement Heat Transfer: Physics, Correlations, and Numerical Modeling. *Advances in Heat Transfer*, vol. 39, no. C, pp. 565–631.
Available at: dx.doi.org/10.1016/S0065-2717(06)39006-5